Numerical Investigations of Turbulent Hydrogen Combustion for Uniform and Stratified Mixtures in Confined Geometries

Thesis Report

ME55035 ME-EFPT MSc Thesis

Harish Karthik

Delft University of Technology

TU Delft

Numerical Investigations of Turbulent Hydrogen Combustion for Uniform and Stratified Mixtures in Confined Geometries

Thesis Report

by

Harish Karthik

Student number:	6054641
Supervisor:	Dr. Rene Pecnik
Co - Supervisor:	Dr. Anna Felden
NRG Supervisor:	Dr. Sina Tajfirooz
Project Duration:	Oct 2024 - Aug 2025
Faculty:	Faculty of Mechanical Engineering, Delft

The thesis is being carried out in collaboration with Nuclear Research and Consultancy Group (NRG).

TU Delft

NRG

Acknowledgments

Harish Karthik
Alkmaar, August 2025

I would like to begin by expressing my sincere gratitude to Dr. Sina Tajfirooz and Dr. Ed Komen, my supervisors at the Nuclear Research and Consultancy Group (NRG), for their invaluable guidance and daily support throughout this thesis. Their mentorship allowed me to engage in the fascinating research conducted at NRG, exploring the intersection of nuclear engineering and computational fluid dynamics, and tackling the complex challenge of combustion. Through their assistance and insightful discussions, I was able to deepen my understanding of this intricate phenomenon and learn far beyond the fundamentals of fluid flow.

I am equally grateful to my academic supervisors from Delft University of Technology, Dr. René Pecnik and Dr. Anna Felden, for their valuable feedback and supervision during this project. Their expertise and advice have been instrumental in shaping the outcome of this work.

Finally, I would like to thank my parents and my brother for their unwavering encouragement and for always steering me in the right direction, never allowing me to give up. I am also deeply appreciative of my best friend, Pratyusha, for her constant support, for patiently listening to my thoughts, and for motivating me through every high and low.

Abstract

During a severe accident in a watercooled nuclear power plant, large quantities of hydrogen can be generated in the reactor core. The hydrogen mixed with air presents a potential risk of combustion when the hydrogen concentration reaches flammability limits. If combustion occurs, pressure loads can damage safety systems and even compromise the structural integrity of the nuclear reactor walls. Thus, predicting the pressure loads is an important safety issue to ensure the reliability of critical structures in the event of a severe accident.

Computational Fluid Dynamics (CFD) codes can be used as numerical tools to assess the risks of hydrogen combustion and predict detailed transients of the pressure loads. The scenarios simulated in nuclear safety engineering can be analyzed with low fidelity models based on reduction assumptions of the physical phenomena. Specifically, the flame gradient models are chosen to model the combustion phenomena based on a turbulent flame speed to which the combustion propagates.

In this work, the applicability and robustness of a pressure-based solver for compressible reacting flows is first assessed through the canonical Sod shock tube problem, thereby establishing its capability to handle a wide range of Mach numbers relevant to deflagration and mild shock regimes. Building upon the baseline `XiFoam` solver, two new solvers are introduced: `NRGXiFoam` for fully premixed conditions, and `ppNRGXiFoam` for partially premixed configurations. A central contribution of this thesis is the optimisation, modification, and integration of a generic laminar flame speed library into `OpenFOAM`, enabling robust predictions for lean hydrogen-air mixtures across a wide range of conditions.

The `ppNRGXiFoam` solver extends the fully premixed framework by incorporating transport equations for the mixture fraction and its variance, thereby enabling the simulation of fuel stratification effects. The updated flame speed library is validated against experimental data for lean stratified hydrogen–air flames, and its interaction with turbulence closures is assessed through different algebraic wrinkling factor models.

Validation and performance assessment are carried out on two experimental configurations ENACCEF and the ENACCEF-2 flame acceleration facilities with obstacle-induced turbulence. Key quantities such as flame radius, turbulent flame speed, and pressure rise are compared to experimental data, with sensitivity studies performed on mesh resolution, time-stepping, and turbulence model selection.

Overall, the developments presented in this thesis significantly enhance the predictive capability of `OpenFOAM` for partially premixed hydrogen combustion under conditions relevant to nuclear safety, while providing a validated and flexible framework for modelling turbulent flame propagation with composition inhomogeneities.

Contents

List of Figures

List of Tables

Nomenclature

Abbreviations

Abbreviation	Definition
AMR	Adaptive Mesh Refinement
ASTEC	Accident Source Term Evaluation Code
BWR	Boiling Water Reactor
CFD	Computational Fluid Dynamics
CVCS	Chemical Volume Control System
DES	Detached Eddy Simulation
DNS	Direct Numerical Simulation
ETFC	Extended Turbulent Flame Closure
FCVS	Filtered Containment Venting System
GTFC	Goulier Turbulent Flamespeed Closure
IACC	Isochoric Adiabatic Complete Combustion
IAEA	International Atomic Energy Agency
IEA	International Energy Agency
LES	Large Eddy Simulation
LP	Lumped Parameter
MCCI	Molten Core Concrete Interaction
MELCOR	Methods for Estimation of Leakages and Consequences of Releases
NAS	National Academy of Sciences
PAR	Passive Autocatalytic Recombiner
RANS	Reynolds Averaged Navier Stokes
TFC	Turbulent Flame Closure
TMI	Three Mile Island
Xe^{135}	Xenon-135

Symbols

Symbol	Definition	Unit
a	Generic scalar quantity	[-]
$\overline{a}$	Reynolds-averaged value of a	[-]
a'	Fluctuating component in Reynolds decomposition	[-]
a''	Favre fluctuation	[-]
$\widetilde{a}$	Favre-averaged (density-weighted) value of a	[-]
A	Mean flame front cross-sectional area	[m^2]
A_T	Total turbulent flame surface area	[m^2]
A, B	Model constants for TFC and ETFC models	[-]
C_g, C_d	Production and dissipation constants in mixture fraction variance model	[-]
$C_\mu, C_{\varepsilon 1}, C_{\varepsilon 2}, \sigma_k, \sigma_\varepsilon$	k–ε turbulence model constants	[-]
$\beta^*, C_{\omega 1}, C_{\omega 2}, \sigma_\omega$	k–ω turbulence model constants	[-]
c_p	Specific heat capacity at constant pressure	[J/(kg·K)]
$c_p(T)$	Specific heat capacity at constant pressure as a function of T	[J/(kg·K)]

Symbol	Definition	Unit
$c_{p,k}$	Specific heat at constant pressure of species k	[J/(kg·K)]
CFL	Courant–Friedrichs–Lewy number	[-]
δ_L	Laminar flame thickness	[m]
δ_{PH}	Preheat zone thickness	[m]
δ_{R}	Reaction zone thickness	[m]
$\Delta h^0_{f,k}$	Standard enthalpy of formation of species k at T_0	[J/kg]
Δt	Time step size	[s]
Δx	Grid spacing	[m]
D	Binary mass diffusion coefficient	[m^2/s]
D_{ref}	Reference mass diffusivity	[m^2/s]
D_t	Turbulent diffusivity	[m^2/s]
D_t^{∞}	Asymptotic turbulent diffusivity	[m^2/s]
Da	Damköhler number	[-]
Da_T	Turbulent Damköhler number	[-]
E_{int}	Internal energy per unit mass	[J/kg]
E_{kin}	Kinetic energy per unit mass	[J/kg]
E_{tot}	Total energy per unit mass	[J/kg]
$f_{k,n}$	External force on species n in direction k	[m/s^2]
h	Total specific enthalpy of mixture	[J/kg]
h_k	Specific enthalpy of species k	[J/kg]
k_{th}	Thermal conductivity	[W/(m·K)]
Ka_T	Turbulent Karlovitz number	[-]
l_0	Turbulent integral length scale	[m]
L	Characteristic length scale	[m]
L_{ref}	Reference length scale	[m]
M	Mach number	[-]
$\dot{m}$	Mass flow rate	[kg/s]
N_{cells}	Total number of computational cells	[-]
p	Pressure	[Pa]
p_0	Initial pressure	[Pa]
p_{out}	Outlet pressure	[Pa]
p_{ref}	Reference pressure	[Pa]
Pr	Prandtl number	[-]
Pr_t	Turbulent Prandtl number	[-]
Q_{comb}	Total heat release from combustion	[J]
$\dot{Q}$	Heat release rate	[W]
q_k	Heat flux in k^{th} direction	[W/m^2]
R_f	Flame radius	[m]
Re	Reynolds number	[-]
Re_L	Reynolds number based on L	[-]
ρ	Density	[kg/m^3]
ρ_b	Density of burnt gases	[kg/m^3]
ρ_{ref}	Reference density	[kg/m^3]
S	Stoichiometric mass ratio	[-]
S_L	Laminar flame speed	[m/s]
S_L^{∞}	Strained laminar flame speed	[m/s]
S_T	Turbulent flame speed	[m/s]
Sc	Schmidt number	[-]
$\mathrm{Sc}_{t,j}$	Turbulent Schmidt number for species j	[-]
Σ	Flame surface density	[m^2/m^3]
t_0	Integral timescale	[s]
t_c	Chemical timescale	[s]
t_η	Kolmogorov timescale	[s]
t_{ref}	Reference time scale	[s]

Symbol	Definition	Unit
T_0	Initial temperature	[K]
T_B	Burnt gas temperature	[K]
T_{IG}	Ignition temperature	[K]
T_{in}	Inlet temperature	[K]
T_{ref}	Reference temperature	[K]
T_U	Unburnt gas temperature	[K]
$u'(\eta)$	Velocity fluctuation at Kolmogorov scale	[m/s]
$u'(l_t)$	Velocity fluctuation at integral scale l_t	[m/s]
u_{in}	Inlet velocity	[m/s]
u_{out}	Outlet velocity	[m/s]
u_{ref}	Reference velocity scale	[m/s]
u_i	Velocity component in i^{th} direction	[m/s]
u_k	Velocity component in k^{th} direction	[m/s]
u_i'	Reynolds velocity fluctuation	[m/s]
u_i''	Favre velocity fluctuation	[m/s]
$V_{k,i}$	Diffusion velocity of species k	[m/s]
V_T	Spatial turbulent flame velocity	[m/s]
W_F	Molecular weight of fuel	[kg/mol]
W_O	Molecular weight of oxidizer	[kg/mol]
X_F	Mole fraction of fuel	[-]
X_O	Mole fraction of oxidizer	[-]
$Y_{k,0}$	Initial mass fraction of species k	[-]
$Y_{k,\mathrm{in}}$	Inlet mass fraction of species k	[-]
Y_n	Mass fraction of species n	[-]
Z	Mixture fraction	[-]
$\widetilde{Z}$	Favre-averaged mixture fraction	[-]
Z_{st}	Stoichiometric mixture fraction	[-]
$\widetilde{Z''^2}$	Variance of mixture fraction	[-]
α	Thermal diffusivity	[m^2/s]
α_b	Mass diffusivity of burnt gases	[m^2/s]
α_u	Thermal diffusivity of unburnt gases	[m^2/s]
$\dot{\omega}_T$	Heat release rate due to chemical reactions	[W/m^3]
$\overline{\dot{\omega}}_c$	Mean source term of progress variable	[kg/(m^3·s)]
Θ	Activation temperature	[K]
θ_F'	Stoichiometric coefficient of fuel	[-]
θ_O'	Stoichiometric coefficient of oxidizer	[-]
κ_s	Local strain rate	[s^{-1}]
λ	Thermal conductivity	[W/(m·K)]
λ_u	Thermal conductivity of unburnt gases	[W/(m·K)]
μ	Dynamic viscosity	[Pa·s]
μ_{ref}	Reference dynamic viscosity	[Pa·s]
μ_t	Turbulent viscosity	[Pa·s]
ρ_b	Density of burnt gases	[kg/m^3]
ρ_{ref}	Reference density	[kg/m^3]
$\sigma_k, \sigma_\varepsilon, \sigma_\omega$	Turbulence model constants	[-]
τ_c	Chemical timescale	[s]
τ_L	Lagrangian turbulence timescale	[s]
τ_η	Kolmogorov time scale	[s]
τ_{ij}	Mean viscous stress tensor	[Pa]
τ_{ki}	Viscous stress tensor component	[Pa]
$\tilde{c}$	Favre-averaged progress variable	[-]
Ξ	Flame wrinkling factor	[-]

1 Introduction

1.1. Background

1.1.1. Energy Demand and the Role of Nuclear Power

Global electricity consumption has exhibited a consistent upward trend over the past several decades, and this demand is projected to continue growing in the foreseeable future [1]. Currently, a significant portion of global electricity is generated using fossil fuels such as coal and natural gas. These sources are associated with high carbon dioxide (CO_2) emissions per unit of electricity, contributing to global warming and climate change through greenhouse effects.

In light of environmental concerns and international climate commitments, there has been a growing push toward cleaner energy alternatives. Renewable energy technologies-such as solar, wind, and hydro have rapidly advanced. Alongside these, nuclear power remains a key component of the low-carbon energy portfolio, contributing approximately 15% of the world's electricity [1]. Nuclear energy is particularly valued for its high energy density and low greenhouse gas emissions during routine operation.

1.1.2. Risks in Nuclear Accidents

Despite these benefits, nuclear energy continues to raise concerns regarding radiological safety, particularly in the event of severe accidents. One of the most critical hazards involves the release of radioactive isotopes such as xenon-135 (Xe^{135}) and iodine-131 (I^{131}). These isotopes are direct fission products of uranium and are generated through reactions such as [2]:

$$^{235}\mathrm{U} + \mathrm{n} \rightarrow {}^{131}\mathrm{I} + {}^{104}\mathrm{Mo} + 3n + \text{energy} \tag{1.1}$$

$$^{235}\mathrm{U} + \mathrm{n} \rightarrow {}^{135}\mathrm{Xe} + \text{fission product} + \text{neutrons} \tag{1.2}$$

In addition to radioactive releases, hydrogen generation during accident conditions poses a major threat to containment integrity. One of the dominant sources of hydrogen is the oxidation of zirconium alloy cladding in the presence of steam at high temperatures:

$$\mathrm{Zr\ (s)} + 2\,\mathrm{H_2O\ (g)} \rightarrow \mathrm{ZrO_2\ (s)} + 2\,\mathrm{H_2\ (g)} \tag{1.3}$$

Zirconium-based alloys, such as Zircaloy-4, are commonly used as cladding material for nuclear fuel rods due to their low neutron absorption cross-section and favorable mechanical properties under irradiation [2].

Under normal operating conditions, small amounts of hydrogen are generated through this reaction and are removed by systems such as the Chemical Volume Control System (CVCS) [3, 4]. However, in severe accident scenarios, hydrogen production can escalate dramatically. Two primary mechanisms contribute to this:

- When fuel cladding temperatures exceed approximately 1200 °C, the zirconium-steam reaction becomes highly exothermic and can become self-sustaining.
- Interaction between molten core material (corium) and the concrete base of the containment-known as Molten Core Concrete Interaction (MCCI)—leads to further hydrogen production through thermal decomposition of concrete.

The accumulation of hydrogen inside the containment structure can lead to the formation of flammable or explosive mixtures, particularly in reactor types that use air instead of inert gases such as nitrogen. Although safety systems like Passive Autocatalytic Recombiners (PARs) and igniters are designed to manage hydrogen levels, these devices may be insufficient during rapid hydrogen generation. If an ignition source is present, hydrogen combustion can occur, producing significant pressure loads that threaten the structural integrity of the containment.

1.1.3. Nuclear Accidents and Mitigation Strategies

The safety of nuclear power plants remains a critical concern in the domain of energy generation, particularly due to the high-consequence nature of severe accident scenarios. Among the various hazards, hydrogen generation and combustion present significant risks to plant integrity and public safety. Hydrogen may be produced through several high-temperature reactions during accidents, including zirconium-steam reactions, steel oxidation, molten core-water interactions, and molten core-concrete interactions (MCCI). Once released into the containment atmosphere, hydrogen can mix with air to form flammable or explosive mixtures. If ignited, the resulting combustion or detonation can generate rapid pressure transients capable of compromising the containment structure.

The importance of managing hydrogen risk has been underscored by major nuclear accidents. In the 1979 Three Mile Island (TMI) incident, a loss-of-coolant event led to overheating of the fuel cladding. A subsequent zirconium-steam reaction produced a significant amount of hydrogen gas, resulting in a pressure increase of approximately 2 bar within the containment [5]. While combustion was ultimately avoided, the incident emphasized the potential threat of hydrogen accumulation and highlighted the need for better understanding and mitigation of hydrogen-related hazards [6].

The Fukushima Daiichi disaster in March 2011 further demonstrated the catastrophic consequences of unmanaged hydrogen buildup. Following core damage due to prolonged station blackout, hydrogen generated from zirconium-water reactions accumulated in the reactor buildings of Units 1, 3, and 4. In the absence of effective venting or recombination, this hydrogen ignited and caused massive explosions, severely damaging the reactor infrastructure [7, 8]. Unit 2 also suffered possible containment failure. These events illustrated the limitations of existing safety measures and underscored the urgent need for comprehensive hydrogen management strategies. To mitigate hydrogen risk, nuclear power plants employ a combination of passive and active safety systems. The most widely used include:

- **Passive Autocatalytic Recombiners (PARs):** These devices promote the recombination of hydrogen and oxygen into water vapor without requiring external power [9]. PARs are compact, self-activating, and operate continuously once hydrogen is present.
- **Pressure Relief Valves:** Designed to relieve overpressure in the containment, these valves can prevent structural damage by releasing gas to the environment or to filtered systems [10].
- **Containment Inerting and Controlled Igniters:** Some reactor designs, especially older Boiling Water Reactors (BWRs), use containment inerting (e.g., nitrogen atmosphere) to suppress combustion. Others implement igniters to burn hydrogen in a controlled manner and prevent explosive concentration buildup [11].
- **Filtered Containment Venting Systems (FCVS):** These systems allow depressurization of the containment atmosphere through high-efficiency filters that minimize radioactive release. FCVS installations became mandatory in many countries following the Fukushima disaster [12].

While these systems represent significant advancements in hydrogen risk management, they are not without limitations. PARs operate steadily but relatively slowly, which may not be sufficient during rapid hydrogen release. Relief valves can become overwhelmed in large-scale accident scenarios, leading to partial containment overpressurization [10]. Even containment inerting cannot eliminate the risk entirely—hydrogen that escapes into auxiliary buildings may still form explosive mixtures if mixed with air and ignited [10].

These limitations were brought into sharp focus during the Fukushima Daiichi accident. Despite the presence of some mitigation systems, hydrogen explosions still occurred, highlighting gaps in protection. Furthermore, this event marked a turning point in how the nuclear safety community perceives hydrogen hazards. Prior to Fukushima, most safety assessments focused on primary system failures such as loss-of-coolant accidents (LOCAs) and core melt as the dominant contributors to radioactive release [13, 14, 15]. Post-Fukushima, there is greater emphasis on hydrogen combustion and its role in containment failure [16]. In response, regulatory bodies and plant operators have moved toward multi-layered hydrogen management strategies. These include not only the hardware systems described above but also improved diagnostics, procedural enhancements, and the development of advanced modeling tools [17].

1.1.4. Modeling Strategies for Hydrogen Combustion

Accurate prediction of hydrogen combustion behavior in nuclear containment structures is essential for assessing safety margins during severe accidents. In particular, reliable peak pressure estimates are required to evaluate structural integrity under combustion-induced loads. To this end, two primary classes of simulation tools are employed: Lumped Parameter (LP) codes and Computational Fluid Dynamics (CFD) codes [17].

LP codes - such as MELCOR [18], CONTAIN [19], ASTEC [20], and SPECTRA [21] are widely used in industry and regulatory applications due to their computational efficiency and broad validation history. These models divide the containment into a small number of interconnected control volumes (typically 50–100) and solve conservation equations under strong assumptions, such as homogeneous mixing and isochoric, adiabatic complete combustion (IACC). While suitable for global accident analysis and screening, LP codes lack the spatial resolution to capture key local effects such as flame acceleration, vent flows, or interactions with internal structures.

In contrast, CFD tools - including OpenFOAM [22], ANSYS Fluent [23], and STAR-CCM+ [24] —solve the Navier-Stokes equations with detailed sub-models for turbulence and combustion. These tools can resolve fine-scale flow features, enabling the prediction of localized flame fronts, pressure spikes, and transient mixing phenomena that are critical in hydrogen combustion scenarios. However, CFD simulations are resource-intensive and introduce uncertainties related to turbulence and flame modeling, especially under rapidly evolving thermodynamic conditions.

Rather than being mutually exclusive, LP and CFD approaches are increasingly viewed as complementary. A practical coupling strategy involves using LP codes to simulate a broad spectrum of accident sequences and identify worst-case scenarios. CFD analysis is then applied selectively to these critical cases for high-fidelity resolution of local combustion dynamics [25]. This tiered approach balances accuracy and computational cost, enabling robust safety assessments without exhaustive resource use.

Within the CFD framework, multiple turbulence-combustion modeling strategies exist, each suited to different levels of fidelity and computational demand. Reynolds-Averaged Navier-Stokes (RANS) models [26] provide time-averaged predictions at relatively low cost and are often used in engineering practice. Large Eddy Simulation (LES) [27], by contrast, resolves the large-scale turbulent structures while modeling only subgrid effects, leading to improved accuracy in transient flame behavior but at significantly higher computational cost. Hybrid RANS-LES approaches, such as Detached Eddy Simulation (DES) [28], attempt to combine the strengths of both techniques and are increasingly explored in nuclear safety applications.

Model Choices in the Present Work

The thesis described in this report addresses the problem of simulating hydrogen turbulent combustion scenarios for nuclear safety management using CFD. While hydrogen-air combustion in reality involves complex chemical kinetics, with more than fifty elementary reactions and radical species formation, the present work adopts a simplified approach, not based on detailed chemistry.

This choice reflects the objectives of severe accident analysis, where the primary interest lies in predicting integral quantities such as flame speed, pressure, rather than resolving intermediate species. Detailed chemistry models, while more physically complete, incur computational costs for containment-scale simulations and introduce additional uncertainties in reaction rate parameters. For these reasons, flame speed–based models, combined with experimentally derived correlations, remain the pragmatic choice for engineering-scale nuclear safety analysis.

For turbulence closure, a Reynolds Averaged Navier Stokes (RANS) approach is adopted in preference to Large Eddy Simulation (LES) or Direct Numerical Simulation (DNS) [29]. While LES offers higher fidelity by resolving the large-scale turbulent motions and explicitly modelling only subgrid contributions, its computational expense renders it impractical for full-containment accident scenarios. RANS models, by contrast, provide time-averaged solutions at a fraction of the cost, and have a long history of use in regulatory and industrial hydrogen safety studies.

A pressure-based solution algorithm is adopted in this work to ensure robustness across the range of Mach numbers relevant to containment-scale hydrogen deflagrations. Unlike density-based solvers, which are optimised for fully compressible high-Mach flows, pressure-based methods solve directly for pressure and remain well-behaved in low-speed and mixed-flow regimes without the need for preconditioning. This makes them efficient for the predominantly subsonic to transonic conditions of accident scenarios, while still capable of handling shocks and discontinuities when appropriate compressibility corrections are applied. The validity of this approach has been explicitly verified in this study.

In summary, the combination of a flame speed-based combustion model, RANS turbulence closure, and a pressure-based solution strategy represents a pragmatic balance between physical fidelity and computational tractability for large-scale, accident-relevant hydrogen combustion simulations. These modelling choices are consistent with current engineering practice, while the integration of modern experimental correlations enhances predictive accuracy within the adopted framework.

1.2. Research Context and Objectives

This work continues a series of CFD-based investigations carried out at Nuclear Research and Consultancy Group (NRG) using OpenFOAM to simulate hydrogen combustion in nuclear reactor containments.

Previous research by Lobato Pérez [30] focused on implementing existing turbulent combustion models in an open-source CFD framework. The key research questions in that study were:

- How can classical combustion model formulations be implemented in OpenFOAM?
- Can the resulting simulations be made less case-dependent with respect to ignition strategies and empirical constants?
- How can these combustion models be verified and validated?
- Can Adaptive Mesh Refinement (AMR) be implemented for axisymmetric domains in OpenFOAM?
- How do different turbulence models interact with combustion models under phenomena such as flame acceleration or buoyant flows?

Building on this, De Palma's [31] work explored the applicability of a hydrogen specific combustion model - the Goulier Turbulent Flamespeed Closure (GTFC) [32] within the ENACCEF[33] facility. His research addressed the performance of GTFC in inhomogeneous hydrogen-air mixtures, expanding the scope beyond earlier studies that focused solely on homogeneous conditions.

Research Focus of the Present Work: The present study advances this line of research by incorporating new experimental correlations for the laminar flame speed derived by Bentaïb [34]. These correlations will be integrated into a CFD solver developed in OpenFOAM, capable of handling both partially premixed and non-premixed hydrogen-air mixtures. The core research questions addressed in this thesis are:

- What is the range of applicability and numerical stability of a pressure-based solver for reactive flow under accident relevant conditions?
- How can newly derived laminar flame speed correlations (e.g. Bentaïb [34]) be implemented and validated within a turbulent combustion model in OpenFOAM?
- Can the solver accurately capture combustion in inhomogeneous mixtures using mixture fraction and mixture fraction variance as key inputs?
- How does mixture inhomogeneity affect flame development, propagation, and pressure dynamics in confined geometries?
- Previous a priori analyses, such as those by Sathiah [35], have suggested that mixture fraction variance (Z''^2) plays a negligible role in hydrogen combustion modeling under certain conditions. This study re-examines that assumption by explicitly incorporating mixture fraction variance into a pressure-based solver for inhomogeneous hydrogen-air mixtures. The aim is to assess whether accounting for Z''^2 improves predictive accuracy in pressure loads and flame propagation under non-uniform, partially premixed conditions.

This investigation aims to improve the predictive accuracy of hydrogen combustion simulations in realistic nuclear safety scenarios, thereby supporting model development for containment-scale applications.

1.3. Thesis Outline

This thesis report is divided into six chapters, including the current introductory chapter.

Chapter 2 presents the theoretical background relevant to this work. It begins with the governing equations of fluid flow and scalar transport, followed by an introduction to turbulence and its modeling approaches. The chapter then provides an overview of combustion theory, discussing the different modes of premixed combustion, including laminar and turbulent regimes. Finally, it introduces the concept of partially premixed combustion, outlining its key physical mechanisms and relevance to the present study.

Chapter 3 introduces the mathematical modelling methodologies employed in this study. It focuses on Reynolds-Averaged Navier–Stokes (RANS) based approaches for turbulence closure and then discusses the key closure models for turbulent combustion adopted in this work.

In Chapter 4, the numerical framework employed in this study is introduced. The chapter begins with a description of the finite volume method and the pressure–velocity coupling strategy, followed by an overview of the baseline `XiFoam` solver. The solver's applicability is then validated using the Sod shock tube benchmark case. Subsequently, the important parameters necessary for modelling turbulent combustion are described, including the flame radius calculation methods, laminar flame speed correlations and corrections, and wrinkling factor models. The chapter concludes with the introduction of the two custom solvers used in this work—`NRGXiFoam` and `ppNRGXiFoam`-alongside the implementation of a generic flame speed library for stratified mixtures.

Chapter 5 describes the ENACCEF facility setup and presents the main simulation results. The validation of the implemented model is conducted against experimental data, and a sensitivity analysis is performed to assess the influence of mixture fraction variance on combustion behavior in partially premixed regimes.

Finally, Chapter 6 concludes the thesis with a summary of key findings and provides recommendations for future work, including proposed extensions to the combustion model and its validation in other containment-relevant configurations.

2

Turbulent Flows and Combustion

Hydrogen combustion in nuclear reactor containments presents unique challenges due to its strong coupling with turbulence and mixing phenomena. Accurate modeling of such systems requires a sound understanding of the underlying fluid mechanics and combustion physics. This chapter presents the theoretical background necessary for analyzing and simulating turbulent reactive flows, with a focus on premixed and partially premixed combustion regimes relevant to hydrogen safety studies.

Turbulence plays a central role in enhancing mixing and flame propagation, especially in accident scenarios involving inhomogeneous hydrogen-air distributions. Section 2.2 introduces the fundamentals of turbulence, including key length and time scales, and the statistical framework used for modeling turbulent flows. Section 2.1 outlines the governing equations for reactive flows, including species transport and thermodynamic coupling.

In premixed combustion, the flame front propagates through a mixture where fuel and oxidizer are present in stoichiometric or near-stoichiometric proportions. Sections 2.4 and 2.5 provides an overview of premixed and partially premixed combustion theory, laminar and turbulent flame speeds, and relevant combustion regimes.

The content of this chapter establishes the theoretical foundation upon which the numerical modeling and solver development in the following chapters are built.

2.1. Governing Equations

The behavior of both reacting and non-reacting flows is governed by a set of fundamental conservation equations. This section outlines the governing equations for mass, momentum, energy, and species transport that form the basis of computational fluid dynamics (CFD) modeling in reactive flow systems.

2.1.1. Continuity/ Mass Conservation

The conservation of mass, commonly referred to as the continuity equation, governs the behavior of a fluid as it moves through a differential control volume. For a compressible flow, the continuity equation in Cartesian coordinates is expressed as [36]:

$$\frac{\partial \rho}{\partial t} + \frac{\partial (\rho u_i)}{\partial x_i} = 0 \tag{2.1}$$

Here, ρ represents the fluid density [kg/m^3], and u_i denotes the velocity component in the i^{th} spatial direction [m/s].

2.1.2. Momentum Conservation

The conservation of momentum, commonly represented by the Navier–Stokes equations, describes the evolution of momentum in a fluid due to inertial, pressure, viscous, and external body forces. Derived from Newton's Second Law, this equation applies to both reacting and non-reacting flows. However, in combustion scenarios, flow behavior can differ significantly due to variations in fluid properties such as density and viscosity across the flame front.

For a compressible, Newtonian fluid, the momentum conservation equation in index notation is expressed as [36]:

$$\frac{\partial(\rho u_k)}{\partial t} + \frac{\partial(\rho u_k u_i)}{\partial x_i} = -\frac{\partial p}{\partial x_k} + \frac{\partial \tau_{ki}}{\partial x_i} + \rho \sum_{n=1}^{N} Y_k f_{k,n} \tag{2.2}$$

Here, ρ is the fluid density [kg/m^3], u_k is the velocity component in the k-direction [m/s], p is the pressure [Pa], τ_{ki} is the viscous stress tensor [Pa], Y_n is the mass fraction of species n, and $f_{k,n}$ is the external force acting on species n in direction k.

The viscous stress tensor for a Newtonian fluid is defined as:

$$\tau_{ki} = \mu \left(\frac{\partial u_i}{\partial x_k} + \frac{\partial u_k}{\partial x_i} \right) - \frac{2}{3}\mu \left(\frac{\partial u_j}{\partial x_j} \right) \delta_{ki} \tag{2.3}$$

where μ is the dynamic viscosity [Pa·s], and δ_{ki} is the Kronecker delta function.

Although the mathematical form of the momentum equation remains the same in both reacting and non-reacting flows, combustion introduces substantial local variations in density and viscosity due to sharp temperature gradients. For instance, the thermal expansion across a flame front can lead to local Reynolds number changes by an order of magnitude. As a result, flow fields in reactive environments may exhibit behavior that deviates significantly from their non-reactive counterparts, such as transition from turbulence to laminar flow upon ignition.

These coupled effects highlight the need for appropriate turbulence and combustion modeling to accurately capture flow dynamics in reactive systems.

2.1.3. Species Conservation

In multicomponent reactive flows, the conservation of mass must be extended to account for individual chemical species. While the total mass conservation equation remains unchanged—since combustion does not create or destroy mass—the mass of each species can vary due to convection, diffusion, and chemical reaction.

The general transport equation for the mass fraction Y_k of species k in an N-species mixture is given by [36]:

$$\frac{\partial(\rho Y_k)}{\partial t} + \frac{\partial}{\partial x_i}\left(\rho u_i Y_k\right) = -\frac{\partial}{\partial x_i}\left(\rho V_{k,i} Y_k\right) + \dot{\omega}_k \tag{2.4}$$

Here, ρ is the fluid density [kg/m^3], u_i is the velocity component in the i-th direction [m/s], $V_{k,i}$ is the diffusion velocity of species k along direction i, and $\dot{\omega}_k$ is the reaction rate of species k [kg/(m^{3}s)]. This equation represents a balance between convection, diffusion, and chemical source/sink terms.

The diffusion flux term $\rho V_{k,i} Y_k$ can be approximated using Fick's Law in the case of binary mixtures [36]:

$$V_{k,i} Y_k = -D \frac{\partial Y_k}{\partial x_i} \tag{2.5}$$

where D is the binary mass diffusion coefficient [m^2/s]. While solving for equation 2.4,since the total mass is conserved, only $N-1$ species conservation equations are required, as the N-th can be obtained from the constraint:

$$\sum_{k=1}^{N} Y_k = 1 \tag{2.6}$$

This species transport formulation plays a critical role in capturing flame dynamics, mixture inhomogeneity, and local stoichiometry variations in hydrogen combustion modeling.

2.1.4. Energy Conservation

The conservation of energy in reactive flows is a key component for accurately capturing heat release, temperature evolution, and fluid dynamics during combustion. In this work, the energy balance is expressed in terms of the total enthalpy, which includes both sensible and chemical contributions.

The specific mass enthalpy of species k, denoted h_k, can be written as [36]:

$$h_k = \int_{T_0}^{T} c_{p,k}(T)\, dT + \Delta h^0_{f,k} \tag{2.7}$$

where $c_{p,k}$ is the specific heat at constant pressure $J/(kg)$ of species k, $\Delta h^0_{f,k}$ is the standard enthalpy of formation at the reference temperature T_0, and T is the local mixture temperature.

The total enthalpy h of the mixture is the mass-weighted sum over all species:

$$h = \sum_{k=1}^{N} Y_k h_k \tag{2.8}$$

Applying the First Law of Thermodynamics to a differential control volume leads to the following total enthalpy conservation equation [36]:

$$\frac{\partial(\rho h)}{\partial t} + \frac{\partial}{\partial x_k}(\rho u_k h) = \frac{\partial p}{\partial t} + \frac{\partial}{\partial x_k}(u_i \tau_{ik}) - \frac{\partial q_k}{\partial x_k} + \dot{Q} + \dot{\omega}_T + \rho \sum_{k=1}^{N} Y_k f_{k,i}(u_i + V_{k,i}) \tag{2.9}$$

Here:

- τ_{ik} is the viscous stress tensor [Pa]
- q_k is the heat flux in direction k
- $\dot{Q}$ is an external heat source
- $f_{k,i}$ is the body force acting on species k in direction i
- $\dot{\omega}_T$ is the heat release rate due to chemical reactions
- $V_{k,i}$ is the diffusion velocity of species k
- p is the pressure [Pa]

The heat flux q_k consists of two components: conductive heat transfer (via Fourier's law) and species diffusion enthalpy flux:

$$q_k = -\lambda \frac{\partial T}{\partial x_k} + \rho \sum_{j=1}^{N} h_j Y_j V_{j,k} \tag{2.10}$$

where λ is the thermal conductivity [W/(m·K)], and the second term represents the energy transport due to species diffusion. This term becomes especially relevant in multi-component systems like hydrogen-air mixtures, where thermal diffusion can influence mass and heat transport.

The heat release rate due to chemical reactions, $\dot{\omega}_T$, is defined as:

$$\dot{\omega}_T = -\sum_{k=1}^{N} \Delta h^0_{f,k} \cdot \dot{\omega}_k \tag{2.11}$$

where $\dot{\omega}_k$ is the net reaction rate of species k. This source term captures the energy released (or absorbed) during chemical reactions and is essential for coupling combustion chemistry to fluid motion.

In this thesis, the total enthalpy formulation is used to close the energy equation. It provides a robust framework for compressible reactive flow simulations and has been validated in previous in-house studies [30].

2.2. Turbulent Flows

2.2.1. Introduction to Turbulence

Turbulence is a complex and chaotic state of fluid motion characterized by rapid fluctuations in velocity, pressure, and scalar quantities. Unlike laminar flows, which are smooth and orderly, turbulent flows exhibit irregular and three-dimensional eddy structures that interact across a wide range of spatial and temporal scales [37, 38]. Despite its apparent randomness, turbulence is governed by the same conservation equations that describe laminar flow, and can be analyzed statistically under certain simplifying assumptions.

Turbulent flows typically occur at high Reynolds numbers, where inertial forces dominate over viscous forces. The Reynolds number is a dimensionless parameter defined as:

$$Re = \frac{\rho u L}{\mu} \tag{2.12}$$

where ρ is the fluid density [kg/m^3], u is a characteristic velocity [m/s], L is a characteristic length scale [m], and μ is the dynamic viscosity [Pa·s]. For flows with large Re, viscous effects are confined to small scales, while the bulk of the flow is governed by inertial dynamics.

2.2.2. Energy Cascade and Scale Decomposition

Turbulent motion is typically described as an ensemble of interacting eddies of various sizes. The largest eddies, governed by the geometry and boundary conditions of the flow, are responsible for most of the energy of the mean flow. Through a nonlinear breakdown process known as the *energy cascade* [37] (see figure 2.1), energy is transferred from large to progressively smaller eddies until it reaches the smallest dissipative scales, where viscous effects convert kinetic energy into internal energy (heat) [39, 40].

This multiscale structure of turbulence can be categorized into three regions, as depicted in figure 2.1:

- **Integral Scale Region**: Represents the largest and most energetic eddies, with characteristic length l_t, velocity fluctuation $u'(l_t)$, and time scale τ_t. These are flow-dependent and anisotropic.
- **Inertial Subrange**: Contains intermediate-sized eddies that transport energy without significant viscous effects. This region follows the Kolmogorov $-5/3$ power law for the energy spectrum, and the energy transfer rate ε is assumed to be constant across scales.
- **Dissipation Range**: Comprises the smallest scales where viscosity dominates. These scales are referred to as Kolmogorov scales and define the limit at which turbulent kinetic energy is fully dissipated.

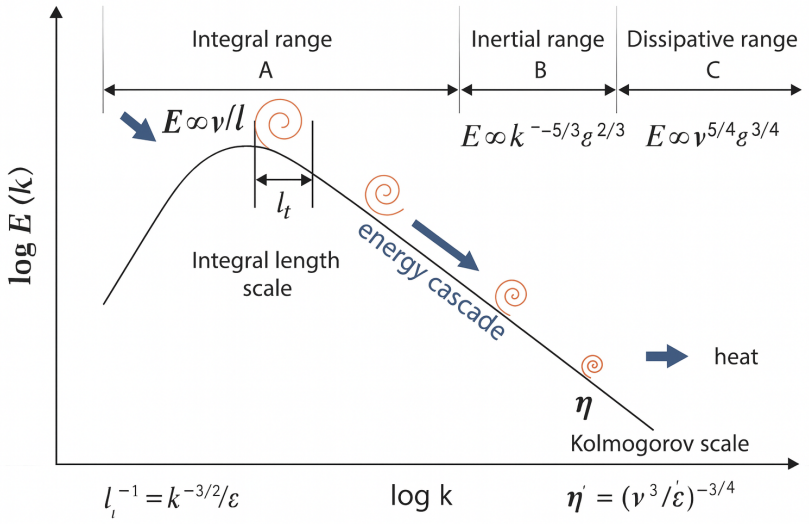

Figure 2.1: Kolmogorov's turbulent energy cascade [41] showing the integral range (A), inertial range (B), and dissipative range (C). Symbols: $E(k)$ – turbulent kinetic energy spectrum at wavenumber k; l_t – integral length scale; η – Kolmogorov length scale; ν – kinematic viscosity; ε – turbulent kinetic energy dissipation rate; $u'(l_t)$ – velocity fluctuation at scale l_t.

2.2.3. Characteristic Turbulent Scales

Integral Scales: The integral length scale l_t, velocity fluctuation $u'(l_t)$, and time scale τ_t can be estimated using the turbulent kinetic energy k and its dissipation rate ε [37]:

$$l_t = \frac{k^{3/2}}{\varepsilon}, \quad u'(l_t) = \sqrt{\frac{2k}{3}}, \quad \tau_t = \frac{l_t}{u'(l_t)} = \sqrt{\frac{3}{2}} \cdot \frac{k}{\varepsilon} \tag{2.13}$$

Kolmogorov (Dissipation) Scales: These represent the smallest scales in a turbulent flow, where energy is dissipated into heat due to viscous effects. Based on dimensional analysis, the Kolmogorov scales are defined as [37]:

$$\eta = \left(\frac{\nu^3}{\varepsilon}\right)^{1/4}, \quad u_\eta = (\nu\varepsilon)^{1/4}, \quad \tau_\eta = \left(\frac{\nu}{\varepsilon}\right)^{1/2} \tag{2.14}$$

In these expressions, η denotes the Kolmogorov length scale [m], which represents the smallest eddy size in the flow where viscous dissipation dominates. u_η is the Kolmogorov velocity scale [m/s], corresponding to the characteristic velocity at the smallest scales, and τ_η is the Kolmogorov time scale [s], indicating the lifespan of these dissipative structures, while ν is the kinematic viscosity, defined as $\nu = \mu/\rho$, with μ being the dynamic viscosity [Pa·s] and ρ the fluid density [kg/m^3].

2.3. Introduction to Combustion

Combustion is a complex physico-chemical process involving an exothermic oxidation reaction between a fuel and an oxidizer. For gaseous combustion, the products are typically gases such as carbon dioxide and water vapor, and the reaction is sustained by the release of heat. The initiation of combustion requires the presence of three elements - fuel, oxidizer, and an energy source - often referred to as the fire triangle. Once ignited, the system becomes self-sustaining due to the continuous energy release and transport of reactive species.

From a modeling perspective, combustion is governed by a tightly coupled set of physical mechanisms, including fluid dynamics, chemical kinetics, heat and mass transfer, and in many cases, turbulent mixing.

These mechanisms influence flame structure, propagation characteristics, and pollutant formation, and therefore must be carefully accounted for in both experimental and numerical analyses.

Combustion can be classified based on several criteria, each providing insight into the dominant physical mechanisms. Two classifications that are especially relevant to hydrogen safety and nuclear containment scenarios are based on (i) the degree of mixing between fuel and oxidizer, and (ii) the mechanism of flame propagation [42].

2.3.1. Classification Based on Reactant Mixing

The way fuel and oxidizer mix determines the spatial structure of the flame and the controlling transport processes. This leads to the following subcategories:

- ***Premixed Combustion:*** In this regime, the fuel and oxidizer are mixed prior to ignition. Upon initiation, the flame front propagates into the unburned mixture, separating the burned and unburned gases. The flame speed and thickness are key parameters in describing the flame structure. Premixed combustion is commonly observed in applications such as spark-ignition engines and domestic gas burners [43].
- ***Non-premixed (Diffusion) Combustion:*** Here, the fuel and oxidizer enter the domain separately and react only upon molecular diffusion at their interface. The reaction rate is limited by the rate of mixing, making this regime diffusion-controlled. This mode is typical of diesel engines, industrial furnaces, and jet diffusion flames.
- ***Partially-Premixed Combustion:*** In practical systems, a strictly premixed or non-premixed condition is rare. Partially-premixed combustion involves inhomogeneous mixtures of fuel and oxidizer, exhibiting regions with varying equivalence ratios. Features of both premixed and diffusion flames are observed. Stratified flows, as encountered in hydrogen containment scenarios, and triple flames are classical examples of this regime.

2.3.2. Classification Based on Propagation Mechanism

When the fuel-air mixture is within the flammability limits (see figure 2.2), the flame may propagate via two distinct modes depending on local thermodynamic and flow conditions:

- ***Deflagration:*** Characterized by a subsonic flame front that propagates primarily through thermal conduction and mass diffusion. The pressure rise is typically modest, and flame speed is governed by the local mixture properties and heat transfer. Deflagrations are the most common mode in hydrogen combustion incidents.

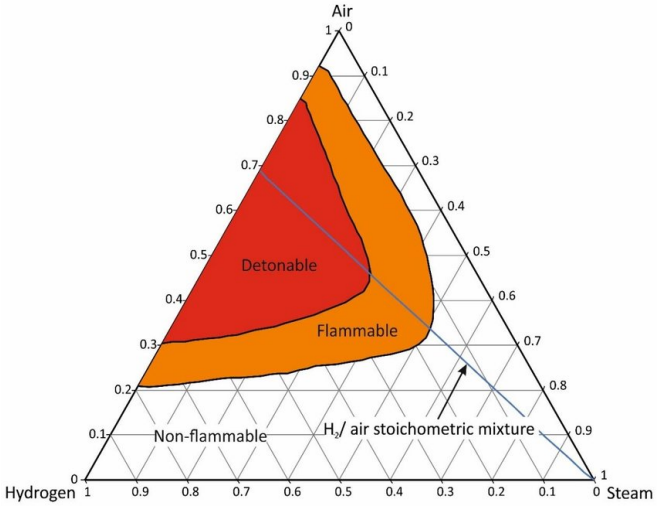

Figure 2.2: Shapiro flammability diagram for hydrogen steam air mixtures [44]

- ***Detonation:*** In this high-energy regime, the combustion wave propagates supersonically, driven by a strong shock wave that compresses and heats the unburnt mixture above its autoignition temperature [45]. Detonations result in a sharp pressure spike and can cause severe structural damage. Although direct initiation of detonation requires large energy input, flame acceleration mechanisms—due to turbulence, obstacles, or confinement—can lead to a Deflagration-to-Detonation Transition (DDT) [46].

These classifications are essential for evaluating hydrogen combustion hazards in nuclear containment systems. In particular, the presence of partially-premixed mixtures and the potential for DDT events demand careful modeling and mitigation strategies [46], which are addressed in later chapters of this thesis.

2.4. Premixed Combustion

When the fuel and oxidizer are thoroughly mixed prior to ignition, the resulting process is referred to as *premixed combustion*. In this configuration, the flame propagates through the mixture as a self-sustaining reaction front, separating the unburnt reactants from the hot combustion products.

Premixed combustion is commonly observed in practical systems such as spark-ignition engines, gas turbines, and domestic burners. From a modeling perspective, premixed flames are often classified into two major categories: laminar and turbulent. Laminar premixed combustion involves a smooth, steady flame front, whereas turbulent premixed combustion is characterized by the interaction between the flame front and turbulent flow structures. These differences influence flame speed, structure, and stability, and are critical for combustion modeling in engineering systems.

Another important classification arises from the degree of mixing between the fuel and oxidizer. While fully premixed flames assume a homogeneous reactant mixture, real systems often involve spatial gradients in equivalence ratio due to incomplete mixing. These configurations fall under *partially premixed combustion*, which is of particular relevance in safety-critical applications such as hydrogen combustion in nuclear reactor containments.

This section focuses on establishing the theoretical foundations of premixed combustion, starting with the laminar regime and followed by turbulent and partially premixed flames.

2.4.1. Laminar Premixed Combustion

A laminar premixed flame is a thin, one-dimensional reactive zone propagating into a quiescent or uniformly moving premixed mixture. In the simplest steady-state configuration, the laminar flame speed S_L exactly balances the incoming reactant velocity, resulting in a stationary flame front in the laboratory frame.

Laminar premixed flames provide the fundamental building blocks for understanding more complex turbulent combustion, since their speed and thickness set the characteristic scales for flame propagation.

Flame Structure and Zones

Figure 2.4.1 shows the schematic structure of a laminar premixed flame, divided into the following zones [47]:

- **Reactants:** The fresh unburnt mixture enters from the left at temperature T_U and flows toward the flame front with velocity $u = S_L$ (see Fig. 2.4.1).
- **Preheat Zone (δ_{PH}):** Region ahead of the reaction zone where heat is conducted from the hot burnt products into the reactants, raising their temperature from T_U to the ignition temperature T_{IG}. No significant chemical reaction occurs here.
- **Reaction Zone (δ_{R}):** Narrow region where the temperature rises sharply from T_{IG} to T_B due to rapid exothermic chemical reactions that consume the fuel.
- **Products:** Fully burnt gases at high temperature T_B leaving the reaction zone; chemical reactions have ceased.

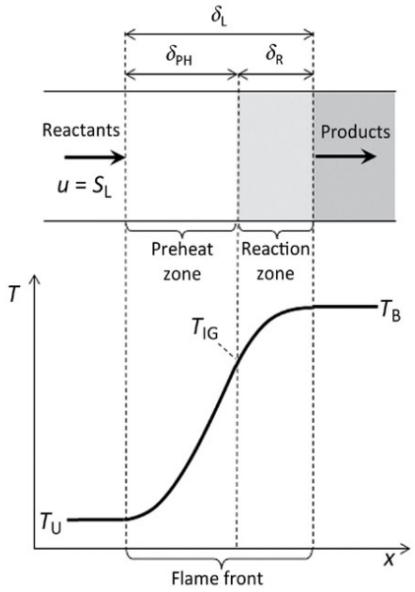

Figure 2.3: Schematic of a one-dimensional laminar premixed flame. Adapted from [48]. S_L = laminar flame speed [m/s], δ_L = total flame thickness [m], δ_{PH} = preheat zone thickness [m], δ_{R} = reaction zone thickness [m], T_U = unburnt gas temperature [K], T_B = burnt gas temperature [K], T_{IG} = ignition temperature [K].

Stoichiometry and Equivalence Ratio

The chemical reaction can be generically expressed as:

$$\theta'_F F + \theta'_O O \rightarrow \text{Products} \tag{2.15}$$

where F and O represent the fuel and oxidizer, and θ'_F, θ'_O are their stoichiometric coefficients. The stoichiometric mass ratio S is then defined as:

$$S = \left(\frac{Y_O}{Y_F}\right)_{st} = \frac{\theta'_O W_O}{\theta'_F W_F} \tag{2.16}$$

where Y_O and Y_F are the mass fractions, and W_O, W_F are the molecular weights of the oxidizer and fuel, respectively. The subscript “st” denotes values at stoichiometric conditions.

A key parameter in premixed combustion is the **equivalence ratio** ϕ, which characterizes the relative proportion of fuel to oxidizer in the mixture compared to the stoichiometric case. It is defined as:

$$\phi = \frac{(X_F/X_O)}{(X_F/X_O)_{st}} = \frac{(Y_F/Y_O)}{(Y_F/Y_O)_{st}} = S \cdot \frac{Y_F}{Y_O} \tag{2.17}$$

Here, X_F and X_O represent the mole fractions of fuel and oxidizer, respectively. An equivalence ratio $\phi < 1$ corresponds to a *lean* mixture (excess oxidizer), $\phi > 1$ indicates a *rich* mixture (excess fuel), and $\phi = 1$ is the *stoichiometric* case.

An equivalence ratio $\phi < 1$ corresponds to a *lean* mixture (excess oxidizer), $\phi > 1$ indicates a *rich* mixture (excess fuel), and $\phi = 1$ is the *stoichiometric* case. In the context of nuclear reactor safety and hydrogen combustion, the mixtures are typically lean due to the stratification of hydrogen in the containment volume.

Key Flame Parameters

The two key parameters defining the flame are the **laminar flame speed** S_L and the **flame thickness** δ_L.

Laminar Flame Speed S_L: The laminar flame speed S_L is defined as the velocity at which a planar flame front propagates into the unburnt premixed reactants under adiabatic and quiescent conditions. It represents a fundamental property of the fuel–oxidizer mixture and depends on thermochemical parameters such as the equivalence ratio, temperature, pressure, and reaction mechanism.

Based on the Activation Energy Asymptotic (AEA) theory [47], and under the assumption of a single-step irreversible reaction and unity Lewis number(refer to A.1), the conservation equations across the flame front can be reduced to a system of ordinary differential equations involving a progress variable c, defined as:

$$c = \frac{Y_f' - Y_{f,u}}{Y_{f,b} - Y_{f,u}} \quad \xrightarrow{\text{when Le=1}} \quad c = \frac{T - T_u}{T_b - T_u}, \tag{2.18}$$

where Y_f' is the local fuel mass fraction, and $Y_{f,u}$, $Y_{f,b}$ are the mass fractions of the unburnt and burnt gases, and T is the local temperature, and T_u, T_b are the temperatures of the unburnt and burnt gases, respectively. The variable $c \in [0, 1]$ represents the transition from unburnt to burnt states.

The simplified governing equations 2.1, 2.2, and 2.4 assuming a constant density ρ and thermal diffusivity D,can be written using c, and takes the form:

$$\begin{aligned} &\frac{d}{dx}(\rho u) = 0, \\ &\frac{d}{dx}(\rho u^2) = \frac{d}{dx}\left(\frac{4}{3}\mu\frac{du}{dx}\right) - \frac{dp}{dx}, \\ &\frac{d}{dx}(\rho u c) = \frac{d}{dx}\left(\rho D\frac{dc}{dx}\right) + \dot{\omega}_c. \end{aligned} \tag{2.19}$$

where $\dot{\omega}_c$ is the source term describing the chemical reaction rate, which can be modeled as:

$$\dot{\omega}_c = \rho(1-c)\frac{1}{\tau_r}\exp\left(-\frac{\Theta}{T}\right) \tag{2.20}$$

with τ_r representing the characteristic chemical reaction time, and Θ the activation temperature. Assuming steady-state conditions, the laminar flame speed S_L can be extracted by integrating the reaction rate across the flame thickness [47]:

$$S_L = \left(2\alpha_u \int_0^1 \frac{\dot{\omega}_c}{\rho_u}\, dc\right)^{1/2} \tag{2.21}$$

where α_u and ρ_u are the thermal diffusivity and density of the unburnt gases.

Alternatively, dimensional analysis suggests the scaling [47]:

$$S_L \propto \sqrt{\frac{\alpha_u}{\tau_c}} \tag{2.22}$$

where τ_c is the chemical timescale.

Flame Thickness δ_L: The laminar flame thickness δ_L represents the spatial extent of the temperature or species gradient across the flame. Several definitions exist:

1. **Thermal Thickness [49]:**

$$\delta_L = \frac{T_b - T_u}{\max\left|\frac{dT}{dx}\right|} \tag{2.23}$$

2. **Progress Variable-Based Thickness [49]:**

$$\delta_L = \frac{1}{\max\left|\frac{dc}{dx}\right|} \tag{2.24}$$

3. **Diffusive Thickness (based on mixture properties)[49]:**

$$\delta_L = \frac{\alpha_u}{S_L} \tag{2.25}$$

where $\alpha_u = \frac{\lambda_u}{\rho_u c_p}$ is the thermal diffusivity of the unburnt gases.

4. **Corrected Diffusive Thickness[36]**

$$\delta_L = 2\frac{\alpha_u}{S_L}\left(\frac{T_b}{T_u}\right)^{0.7} \tag{2.26}$$

Each of these formulations captures different physical features of the flame, and the appropriate choice depends on the modeling context and available data. In practice, the corrected diffusive thickness is widely used in numerical solvers due to its accuracy and computational efficiency.

Although the AEA theory employs simplifying assumptions—such as constant specific heats, unity Lewis number, and negligible pressure variation—it serves as a useful analytical framework for estimating flame properties and understanding the internal structure of laminar premixed flames.

Summary and Relevance

A laminar premixed flame is fully characterised by S_L and δ_L, which depend on the mixture composition (ϕ), thermodynamic conditions, and transport properties. Although the AEA theory involves simplifying assumptions, it provides a solid analytical foundation for understanding flame structure, and forms the basis for turbulent combustion modelling in hydrogen safety applications.

2.4.2. Turbulent Premixed Combustion

In practical combustion systems, such as engines, gas turbines, or nuclear reactor accident scenarios, the flow is rarely laminar. Instead, combustion often occurs in a turbulent environment where complex interactions between the flame front and turbulent eddies alter flame structure, propagation speed, and stability. This regime is known as *turbulent premixed combustion* and represents one of the most challenging phenomena to model and predict in combustion science.

Governing Parameters

In contrast to the smooth structure of a laminar flame, a turbulent flame front becomes highly wrinkled due to interaction with a range of eddy sizes. These deformations increase the flame surface area, thereby enhancing the overall burning rate. However, the internal flame structure may still resemble that of a laminar flame, depending on the turbulence intensity and length scales relative to the flame thickness. This observation forms the basis of the **flamelet assumption**, which treats the turbulent flame as an ensemble of locally one-dimensional laminar flames. The key parameters influencing turbulent flame behavior include:

- Turbulent velocity fluctuations u',
- Integral length scale l_0,
- Kolmogorov length scale η,
- Laminar flame thickness δ_L,
- Laminar flame speed S_L,
- Chemical time scale $\tau_c = \delta_L / S_L$.

Turbulent Flame Speed

One of the most important quantities in turbulent combustion is the **turbulent flame speed** S_T, which represents the effective rate at which a premixed flame front propagates through a turbulent flow field. It encapsulates both the enhancement in flame surface area due to wrinkling and stretch, and the increased transport of heat and mass caused by turbulent eddies.

Here, **flame wrinkling** refers to the corrugation of the flame front caused by turbulent eddies of various sizes, which increases the total flame surface area available for combustion. **Flame stretch** refers to the local deformation of the flame front due to velocity gradients (strain) or curvature, which can either accelerate or decelerate the local burning rate depending on the mixture and flow conditions.

A widely accepted correlation, originally proposed by Damköhler and refined by Peters [50], relates the turbulent flame speed to the surface area of the wrinkled flame front:

$$\frac{S_T}{S_L} = \frac{A_T}{A} \tag{2.27}$$

where:

- S_T is the turbulent flame speed [m/s],
- S_L is the unstrained laminar flame speed [m/s],
- A_T is the total surface area of the turbulent (wrinkled) flame front [m^2],
- A is the cross-sectional area of the mean flame front [m^2].

At low turbulence intensities, the flame wrinkling scales linearly with the velocity fluctuation, leading to the simplified relation [50]:

$$\frac{S_T}{S_L} \approx 1 + \frac{u'}{S_L} \tag{2.28}$$

where u' is the root-mean-square (rms) turbulent velocity fluctuation [m/s]. This implies that in weak turbulence, the increase in flame speed is primarily geometric. In the limit of strong turbulence ($u' \gg S_L$), the turbulent flame speed becomes proportional to the turbulence intensity, i.e., $S_T \sim u'$, indicating that turbulent transport dominates over chemical reaction rates.

Time Scales and Dimensionless Numbers

To further understand how turbulence interacts with flame propagation, it is essential to compare different characteristic time scales in the system:

$$t_0 = \frac{l_0}{u'} \qquad \text{(Integral timescale)} \tag{2.29}$$

$$t_\eta = \frac{\eta}{u'(\eta)} \qquad \text{(Kolmogorov timescale)} \tag{2.30}$$

$$t_c = \frac{\delta_L}{S_L} \qquad \text{(Chemical timescale)} \tag{2.31}$$

where:

- l_0 is the integral length scale of turbulence [m], representing the size of the largest eddies,
- u' is the velocity fluctuation at the integral scale [m/s],
- η is the Kolmogorov length scale [m], corresponding to the smallest dissipative eddies,
- $u'(\eta)$ is the turbulent velocity fluctuation at scale η,
- δ_L is the laminar flame thickness [m].

Two important non-dimensional numbers derived from these scales are:

$$\text{Damköhler number:} \quad Da_T = \frac{t_0}{t_c} = \frac{l_0/u'}{\delta_L/S_L} \tag{2.32}$$

$$\text{Karlovitz number:} \quad Ka_T = \frac{t_c}{t_\eta} = \frac{\delta_L/S_L}{\eta/u'(\eta)} \tag{2.33}$$

These quantities characterize the relative timescales of turbulent mixing and chemical reaction:

- $Da_T \gg 1$: Chemistry is fast compared to turbulence; the flame structure is preserved.

- $Ka_T \ll 1$: Flame remains largely unaffected by small-scale turbulence (flamelet regime).
- $Ka_T \gg 1$: Small-scale turbulence penetrates into the flame front, potentially disrupting the reaction zone.

Classification of Combustion Regimes

Together, Da_T and Ka_T form the basis for combustion regime classification using diagrams such as the Borghi–Peters diagram, which guide the selection of appropriate modeling strategies in simulations. Figure 2.4 illustrates the main regimes of premixed turbulent combustion in a map defined by the turbulence intensity u'/S_L (ordinate) and the ratio of the integral length scale to the laminar flame thickness l_0/δ_L (abscissa).

Each region in Figure 2.4 corresponds to a distinct flame–turbulence interaction regime:

- **Laminar flames:** Located in the lower-left corner ($Re_T < 1$), turbulence is negligible and the flame propagates as a smooth laminar front.
- **Wrinkled flamelets:** At low turbulence intensities and large Da_T, the flame surface is mildly corrugated (wrinkled) by large eddies, but the internal laminar flame structure is preserved. This region lies in the lower-right part of the diagram, below the $Ka_T = 1$ line.
- **Corrugated flamelets:** With increasing turbulence, eddies begin to interact with the preheat zone while still not penetrating the reaction zone ($Ka_T < 1$). The flame surface area increases significantly, leading to higher burning rates. This region is found above the wrinkled flamelets, between the $Ka_T = 1$ and $Da_T = 1$ boundaries.
- **Thickened wrinkled flames:** In the high-turbulence portion of the flamelet regime ($Da_T > 1,\ Ka_T > 1$), small eddies thicken the flame while maintaining a discernible flamelet structure.
- **Well-stirred reactor:** In the top-left corner ($Da_T < 1$), turbulent mixing is much faster than chemical reaction rates, resulting in a homogenized, reactor-like behavior rather than a propagating flame front.

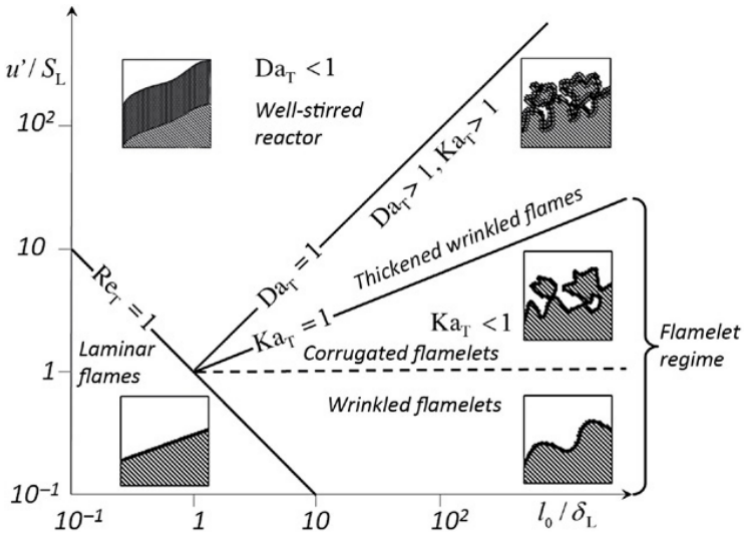

Figure 2.4: Classification of regimes in premixed combustion using the Borghi-Peters diagram [48]. The ordinate represents turbulence intensity (u'/S_L), and the abscissa is the ratio of the integral length scale to the laminar flame thickness (l_0/δ_L).

Additional Physical Effects: Flame Stretch and Curvature

In turbulent flames, the local flame speed may also be affected by strain and curvature, phenomena collectively referred to as flame *stretch*. Stretch can arise either from aerodynamic strain in the surrounding flow or from the intrinsic curvature of the flame front itself. Both mechanisms alter the local burning velocity and, in extreme cases, can lead to local flame quenching.

The strained laminar flame speed S_L^∞ is related to the unstrained speed $S_{L,0}$ through [49]:

$$S_L^\infty = S_{L,0}\left(1 - \left(\frac{\rho_b}{\rho_u}\right)^2 \cdot \frac{\alpha_b}{\alpha_u} \cdot \tau_c \cdot \kappa_s\right) \tag{2.34}$$

where:

- κ_s is the local strain rate [s^{-1}],
- α_b, α_u are the mass diffusivities of the burnt and unburnt gases [m^2/s],
- ρ_b, ρ_u are the densities of the burnt and unburnt gases [kg/m^3],
- τ_c is the chemical timescale [s].

High strain rates reduce S_L^∞ and may cause extinction when the stretch exceeds the flame's ability to sustain propagation.

In the flamelet regime, of particular relevance in nuclear safety scenarios - the turbulent flame is modeled as an ensemble of thin, wrinkled laminar flamelets embedded within the flow field; these flamelets locally propagate at the laminar flame speed, while large-scale turbulence stretches and folds them, forming a so-called "flame brush" [51, 52]. The turbulent flame speed S_T is then interpreted as the mean speed at which this flame brush propagates through the domain.

In complex three-dimensional configurations, defining a unique flame surface is challenging due to the local wrinkling and folding [53]. However, when a spherically expanding flame front is considered - such as in unconfined hydrogen deflagrations—the spatial turbulent flame velocity V_T can be defined as the time derivative of the flame radius R_f, and is related to the turbulent flame speed by:

$$V_T = \frac{dR_f}{dt} = \frac{\rho_u}{\rho_b} S_T \tag{2.35}$$

where ρ_u and ρ_b denote the densities of the unburnt and burnt gases, respectively. This relation assumes spherical symmetry and mass conservation across the flame front, and is especially useful for modeling flame propagation in containment scenarios involving hydrogen-air mixtures.

The modeling of turbulent flame propagation thus requires accurate descriptions of both the geometric wrinkling of the flame front and the underlying laminar flamelet properties. These serve as a basis for algebraic flame speed correlations, level-set methods, and transport equation-based models used in large-scale CFD simulations.

2.5. Partially Premixed Combustion

Partially premixed combustion (PPC) represents a regime that lies between the classical limits of premixed and non-premixed combustion. In this regime, the fuel and oxidizer are mixed to varying degrees prior to ignition, resulting in spatial gradients in mixture composition—typically described by a locally varying equivalence ratio ϕ. This leads to a combustion process influenced by both premixed flame propagation and diffusion-controlled reaction zones, depending on the local stratification.

In accident-relevant scenarios, such as hydrogen combustion in nuclear reactor containments, stratification naturally arises due to density differences between hydrogen and air. The relatively light hydrogen released into the containment tends to accumulate near the upper regions, producing a stable hydrogen-rich layer above a leaner mixture below. This non-uniformity means that the propagating flame will encounter different mixture strengths along its path. As a result, local flame speed, flame structure, and heat release rate can vary significantly during propagation. Stratification can thus strongly influence overall flame acceleration, pressure build-up, and the risk of transitioning to more severe combustion regimes such as deflagration-to-detonation transition (DDT). Understanding flame behaviour in stratified mixtures is therefore essential for accurate safety assessment and predictive modelling.

Three key physical mechanisms characterize PPC flames [54]. First, due to spatial non-uniformity in the equivalence ratio, back-supported stratified combustion may occur, in which the burnt gas temperature exceeds that of a stoichiometric premixed case. Second, the wrinkling and stretching of flame

fronts by turbulence and mixture inhomogeneities increase the flame surface area, though this does not necessarily correlate with an increase in global burning velocity. Lastly, a unique feature in PPC is the formation of a *triple flame*, where lean, stoichiometric, and rich premixed reaction zones coexist, often enhancing the flame propagation speed significantly beyond the laminar flame speed.

Mixture Fraction and Progress Variable: To describe PPC, two scalar quantities are commonly employed: the mixture fraction Z, and the progress variable c. The mixture fraction Z quantifies the local composition of the mixture in terms of mass fractions of constituent elements. For a generic combustion reaction involving fuel, oxidizer, and products:

$$\theta'_F F + \theta'_O O \rightarrow \text{Products} \tag{2.36}$$

the mixture fraction is defined as [55]:

$$Z = \frac{Y_j - Y_{j,\text{ox}}}{Y_{j,\text{fuel}} - Y_{j,\text{ox}}}, \tag{2.37}$$

where Y_j denotes the elemental mass fraction of a conserved atom (e.g., C, H), and $Y_{j,\text{fuel}}$, $Y_{j,\text{ox}}$ are its values in the pure fuel and oxidizer streams, respectively. In this form, $Z = 0$ represents pure oxidizer and $Z = 1$ corresponds to pure fuel.

The progress variable c tracks the conversion of reactants into products and is defined based on species mass fractions (refer equation 2.18).

Transport Equations: The governing transport equations for the mixture fraction Z and the progress variable c are [36]:

$$\frac{\partial(\rho Z)}{\partial t} + \frac{\partial}{\partial x_k}(\rho u_k Z) = \frac{\partial}{\partial x_k}\left(\rho D \frac{\partial Z}{\partial x_k}\right), \tag{2.38}$$

$$\frac{\partial(\rho c)}{\partial t} + \frac{\partial}{\partial x_k}(\rho u_k c) = \frac{\partial}{\partial x_k}\left(\rho D \frac{\partial c}{\partial x_k}\right) + \dot{\omega}_c, \tag{2.39}$$

The scalar Z is conserved in the absence of reactions, whereas c includes a source term $\dot{\omega}_c$, representing the local reaction rate. The local equivalence ratio ϕ can be directly linked to the mixture fraction using:

$$\phi = \frac{Z}{1 - Z} \cdot \frac{1 - Z_{\text{st}}}{Z_{\text{st}}}, \tag{2.40}$$

where Z_{st} is the mixture fraction at stoichiometric conditions.

In this chapter, the fundamental governing equations, combustion regimes, and key physical mechanisms relevant to laminar, turbulent, and partially premixed flames have been presented. These theoretical foundations form the basis for the modelling and numerical approaches developed in the subsequent chapters.

3

Modelling Approaches for Turbulent Combustion

Turbulent reactive flows, such as those encountered in hydrogen combustion systems, are governed by highly nonlinear, multi-scale phenomena that resist analytical solutions. As a result, numerical simulations have become indispensable for understanding and predicting the behavior of such systems. This chapter outlines the principal numerical modeling approaches used in Computational Fluid Dynamics (CFD) for simulating turbulent flows, with a focus on methods applicable to both non-reacting and reacting configurations.

CFD solves the Navier–Stokes equations using different levels of turbulence resolution depending on the available computational resources and the required accuracy. Broadly, three approaches are commonly used [36] in the literature and industry: Direct Numerical Simulation (DNS), Large Eddy Simulation (LES), and Reynolds-Averaged Navier–Stokes (RANS). These are summarized below.

3.1. Overview of Modelling Approaches

Direct Numerical Simulation (DNS): In DNS, the full set of instantaneous Navier–Stokes equations is solved without any turbulence modeling. All scales of motion—from the largest energy-containing eddies to the smallest dissipative scales—are resolved. This method offers the highest fidelity, capturing all turbulent fluctuations and their interactions with chemical reactions. However, the computational cost of DNS increases rapidly with Reynolds number, as the number of required grid points scales with $N \sim Re^{9/4}$ [56]. For typical engineering flows with moderate-to-high Reynolds numbers, DNS remains computationally prohibitive. Thus, DNS is predominantly employed in fundamental research to validate models and study canonical problems.

Large Eddy Simulation (LES): LES offers a compromise between computational cost and accuracy. It resolves the large, energy-containing turbulent eddies explicitly, while the smaller subgrid-scale (SGS) motions are modeled using SGS models. This approach is justified by Kolmogorov's hypothesis that small-scale turbulence is more universal and isotropic than the large-scale structures. LES captures unsteady flow features and spatially-varying turbulence with higher fidelity than RANS and is particularly suited for combustion problems where turbulence-chemistry interactions are important. Nonetheless, LES requires fine spatial and temporal resolution and is typically limited to research applications or high-performance computing environments.

Reynolds-Averaged Navier–Stokes (RANS): In the RANS framework, the governing equations are ensemble-averaged [37] (or time-averaged for steady flows), resulting in a system that describes the mean flow properties. The effects of turbulence are modeled through closure relations, such as eddy-viscosity models, leading to a reduction in computational requirements. Although RANS models do not

resolve turbulent structures explicitly, they provide a computationally efficient framework for simulating a wide range of industrial flows. RANS remains the most widely adopted method in engineering design due to its simplicity, robustness, and lower computational cost.

Figure 3.1 illustrates the hierarchy of turbulence modeling methods with respect to the turbulence energy spectrum. While DNS resolves all modes, LES resolves only large-scale modes up to a cutoff frequency k_c, and RANS models the entire turbulent spectrum.

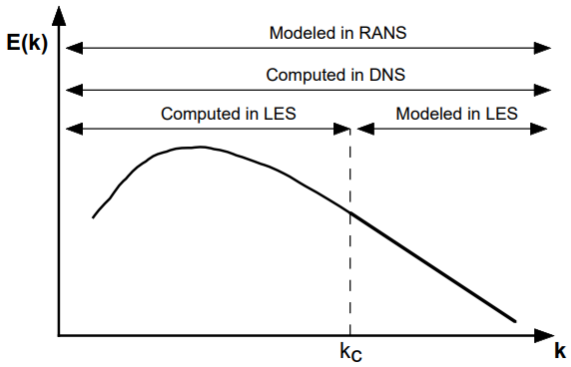

Figure 3.1: Turbulence modeling approaches across the energy spectrum. E(k) is the turbulence energy spectrum [m^3/s^2] and k is the wavenumber [1/m]. k_c is the cut-off wave number used in LES. Adapted from [36].

Given the computational constraints and the large parametric space of the problem, this study adopts the RANS approach to simulate turbulent hydrogen-air flows. Although RANS provides only a time-averaged view of the turbulent field and relies on empirical closure models, it offers a practical compromise between model complexity and computational feasibility. This choice enables the investigation of combustion behavior under various operational conditions, laying the groundwork for more advanced simulations using LES in future work.

In the following sections, the formulation of RANS equations and their application to turbulent combustion modeling are discussed in detail. LES-based formulations are also briefly introduced to highlight their comparative features.

3.1.1. Reynolds and Favre Averaging

The foundation of the Reynolds-Averaged Navier–Stokes (RANS) method lies in decomposing instantaneous flow quantities into a mean and a fluctuating component [37]. This decomposition is known as *Reynolds decomposition*. For a generic scalar quantity a, it is expressed as:

$$a = \overline{a} + a' \tag{3.1}$$

where $\overline{a}$ is the mean (ensemble-averaged) component, and a' is the fluctuating component. When the Reynolds decomposition is substituted into the governing equations and time-averaged, it results in additional correlation terms involving the fluctuating quantities.

The averaging operator obeys several useful mathematical properties, listed below:

$$\overline{a'} = 0 \tag{3.3}$$

$$\overline{ab} = \overline{a}\,\overline{b} \tag{3.4}$$

$$\overline{a'b'} \neq 0 \tag{3.5}$$

Equation (3.5) is of particular importance—it highlights that the product of fluctuating quantities does not vanish upon averaging. These correlation terms, such as $\overline{u_i' u_j'}$ (refer equation **??**), are responsible

for the turbulent transport of momentum and are known as Reynolds stresses. Since they introduce new unknowns, closure models are required to solve the RANS equations.

For flows with significant density variations—typical of reactive flows such as combustion—Reynolds averaging becomes insufficient, , this approach will introduce additional terms because density also needs to be split into a mean and fluctuating term Instead, a *Favre averaging* approach is employed, where density-weighted averages are used [57]:

$$\widetilde{a} = \frac{\overline{\rho a}}{\overline{\rho}}, \quad \text{so that} \quad a = \widetilde{a} + a'' \tag{3.2}$$

Here, $\widetilde{a}$ denotes the Favre-averaged quantity and a'' is the Favre fluctuation. This ensures that $\overline{\rho a''} = 0$, simplifying the treatment of variable-density flows and avoiding additional density–fluctuation cross-terms.

3.1.2. RANS Governing Equations

The Favre-averaged governing equations for mass, momentum, species, and energy are obtained by substituting the Favre decomposition into the instantaneous equations and applying the appropriate averaging. The resulting RANS equations are [36]:

Favre-Averaged Continuity Equation

$$\frac{\partial \bar{\rho}}{\partial t} + \frac{\partial}{\partial x_i}(\bar{\rho}\widetilde{u}_i) = 0 \tag{3.3}$$

Favre-Averaged Momentum Equation

$$\frac{\partial(\bar{\rho}\widetilde{u}_j)}{\partial t} + \frac{\partial}{\partial x_i}(\bar{\rho}\widetilde{u}_i\widetilde{u}_j) = -\frac{\partial \bar{p}}{\partial x_j} + \frac{\partial \tau_{ij}}{\partial x_i} - \frac{\partial}{\partial x_i}\left(\bar{\rho}\widetilde{u_i''u_j''}\right) + \bar{\rho}\sum_{k=1}^{N}\widetilde{Y}_k f_{k,j} \tag{3.4}$$

Favre-Averaged Species Conservation

$$\frac{\partial(\bar{\rho}\widetilde{Y}_k)}{\partial t} + \frac{\partial}{\partial x_i}(\bar{\rho}\widetilde{u}_i\widetilde{Y}_k) = -\frac{\partial}{\partial x_i}\left(\bar{\rho}\widetilde{u_i''Y_k''} + \bar{\rho}V_{k,i}\widetilde{Y}_k\right) + \widetilde{\dot{\omega}}_k \tag{3.5}$$

Favre-Averaged Energy Conservation

$$\begin{aligned}\frac{\partial(\bar{\rho}\widetilde{h})}{\partial t} + \frac{\partial}{\partial x_i}(\bar{\rho}\widetilde{u}_i\widetilde{h}) = \bar{\omega}_T + \frac{D\bar{p}}{Dt} + \frac{\partial}{\partial x_i}\left(\lambda\frac{\partial \bar{T}}{\partial x_i} - \bar{\rho}\widetilde{u_i''h''}\right) \\ + \tau_{ij}\frac{\partial \widetilde{u}_i}{\partial x_j} - \frac{\partial}{\partial x_i}\left(\bar{\rho}\sum_{k=1}^{N}V_{k,i}\widetilde{Y}_k h_k\right)\end{aligned} \tag{3.6}$$

Here:

- $\bar{\rho}\widetilde{u_i''u_j''}$ is the *Reynolds stress tensor*,
- $\bar{\rho}\widetilde{u_i''Y_k''}$ is the turbulent species flux,
- $\bar{\rho}\widetilde{u_i''h_s''}$ is the turbulent enthalpy flux,
- $\widetilde{\dot{\omega}}_k$ is the mean chemical source term for species k,
- $\widetilde{\tau}_{ij}$ is the mean viscous stress tensor,
- $V_{k,i}$ is the laminar diffusion velocity of species k,
- λ is the thermal conductivity.

Closure and Modeling Needs

The RANS equations introduce several unclosed terms that must be modeled:

- **Reynolds stresses:** $\widetilde{\bar{\rho}u_i''u_j''}$, closed using turbulence models (e.g., k-ε, k-ω, Reynolds stress models).
- **Turbulent scalar fluxes:** $\widetilde{\bar{\rho}u_i''Y_k''}$, $\widetilde{\bar{\rho}u_i''h_s''}$, typically modeled using gradient diffusion hypotheses.
- **Chemical source terms:** $\dot{\omega}_k$, closed using finite-rate chemistry models or flamelet-based approaches depending on the combustion regime.

In this work, a RANS framework with finite-rate chemistry is employed to simulate reactive hydrogen-air flows. Turbulence–combustion interactions are partially captured through suitable turbulence and species transport models, allowing for practical and computationlly feasible simulations.

3.1.3. Reynolds Stresses and Turbulence Closure

When the Navier–Stokes equations are Reynolds-averaged, the nonlinear convective terms introduce additional unknowns in the form of Reynolds stresses, defined as $\widetilde{\bar{\rho}u_i''u_j''}$. These terms represent the transport of momentum by turbulent fluctuations and must be modeled to close the system of equations.

A commonly adopted approach for this closure is the **Boussinesq hypothesis**, which introduces the concept of an eddy viscosity μ_t to relate the Reynolds stresses to the mean velocity gradients. The approximation is given as:

$$-\widetilde{\bar{\rho}u_i''u_j''} = \mu_t \left(\frac{\partial \widetilde{u}_i}{\partial x_j} + \frac{\partial \widetilde{u}_j}{\partial x_i} \right) - \frac{2}{3} \left(\bar{\rho}k + \mu_t \frac{\partial \widetilde{u}_k}{\partial x_k} \right) \delta_{ij} \tag{3.7}$$

Here:

- μ_t is the turbulent eddy viscosity [Pa·s],
- $k = \frac{1}{2}\overline{u_i''u_i''}$ is the turbulent kinetic energy [m^2/s^2],
- δ_{ij} is the Kronecker delta,
- $\widetilde{u}_i$ are the Favre-averaged velocity components.

This model assumes isotropic turbulence, which significantly simplifies the problem by treating turbulence-induced momentum transfer analogously to molecular viscosity. However, this isotropy assumption may limit accuracy in flows involving separation, swirl, or strong streamline curvature, where anisotropic effects are prominent.

The eddy viscosity μ_t is not known a priori and must be computed using a turbulence model. Most models estimate μ_t based on the turbulent kinetic energy k and an additional turbulence scale, such as the dissipation rate ε or specific dissipation rate ω. These will be discussed in the following subsections, where different two-equation turbulence models such as k–ε, k–ω, and the k–ε model by Launder and Spalding with buoyancy corrections will be introduced.

3.1.4. Turbulence Models

Turbulence modeling is essential to close the Reynolds-Averaged Navier–Stokes (RANS) equations, especially for the unresolved Reynolds stress terms introduced by the averaging procedure. This section outlines the different two-equation turbulence models employed in this work, each based on the solution of transport equations for turbulent kinetic energy k and either the turbulence dissipation rate ε or the specific dissipation rate ω.

Standard k-ε Model

The standard k–ε model is one of the most widely used turbulence models due to its simplicity and robustness. It solves two transport equations: one for the turbulent kinetic energy k and another for

its dissipation rate ε: The standard k–ε model is a two-equation closure model used to estimate the turbulent kinetic energy k and its dissipation rate ε. The transport equations for these two variables are [58]:

$$\frac{\partial(\bar{\rho}k)}{\partial t} + \frac{\partial}{\partial x_i}\left(\bar{\rho}\widetilde{u}_i k\right) = \frac{\partial}{\partial x_i}\left[\left(\mu + \frac{\mu_t}{\sigma_k}\right)\frac{\partial k}{\partial x_i}\right] + P_k - \bar{\rho}\varepsilon + S_k \tag{3.8}$$

$$\frac{\partial(\bar{\rho}\varepsilon)}{\partial t} + \frac{\partial}{\partial x_i}\left(\bar{\rho}\widetilde{u}_i \varepsilon\right) = \frac{\partial}{\partial x_i}\left[\left(\mu + \frac{\mu_t}{\sigma_\varepsilon}\right)\frac{\partial \varepsilon}{\partial x_i}\right] + C_{\varepsilon 1}\frac{\varepsilon}{k}P_k - C_{\varepsilon 2}\bar{\rho}\frac{\varepsilon^2}{k} + S_\varepsilon \tag{3.9}$$

The term P_k represents the production of turbulent kinetic energy due to mean velocity gradients, and is modeled as:

$$P_k = -\bar{\rho}\widetilde{u_i'' u_j''}\frac{\partial \widetilde{u}_i}{\partial x_j} \tag{3.10}$$

The turbulent eddy viscosity is modeled as:

$$\mu_t = \rho C_\mu \frac{k^2}{\varepsilon}\,, \tag{3.11}$$

The following variables are model constants used in the respective turbulence models. For the standard k–ε model, the constants are typically assigned the following values:

$$\begin{aligned} C_\mu &= 0.09, & \sigma_k &= 1.00, & \sigma_\varepsilon &= 1.30, \\ C_{\varepsilon 1} &= 1.44, & C_{\varepsilon 2} &= 1.92\,. \end{aligned}$$

Buoyant k-ε Model

To account for buoyancy effects, the standard k–ε model is extended by incorporating source terms:

$$S_k = -G_{\text{coeff}} k\,, \tag{3.12}$$

$$S_\varepsilon = -C_{\varepsilon 1}\tanh\left(\frac{|\hat{g}_i \widetilde{u}_i|}{|\widetilde{u}_j - \hat{g}_j(\hat{g}_i\widetilde{u}_i)|}\right) G_{\text{coeff}}\varepsilon\,, \tag{3.13}$$

where G_{coeff} is defined as:

$$G_{\text{coeff}} = C_\mu \frac{k}{\varepsilon} g_i \frac{\partial \rho}{\partial x_i}\,, \tag{3.14}$$

and $\hat{g}_i$ is the normalized gravitational vector. These modifications allow the model to capture stratification and buoyancy-driven turbulence.

k-ω Model

The k–ω model solves for turbulent kinetic energy k and specific dissipation rate ω. The transport equations are [59]:

$$\frac{\partial(\rho k)}{\partial t} + \frac{\partial}{\partial x_i}(\rho\widetilde{u}_i k) = \frac{\partial}{\partial x_i}\left[\left(\mu + \frac{\mu_t}{\sigma_k}\right)\frac{\partial k}{\partial x_i}\right] + P_k - \beta^*\rho\omega k\,, \tag{3.15}$$

$$\frac{\partial(\rho\omega)}{\partial t} + \frac{\partial}{\partial x_i}(\rho\widetilde{u}_i \omega) = \frac{\partial}{\partial x_i}\left[\left(\mu + \frac{\mu_t}{\sigma_\omega}\right)\frac{\partial \omega}{\partial x_i}\right] + C_{\omega 1}\frac{\omega}{k}P_k - C_{\omega 2}\rho\omega^2\,, \tag{3.16}$$

where the turbulent viscosity is calculated as:

$$\mu_t = \rho\frac{k}{\omega}\,, \quad \omega = \frac{\varepsilon}{\beta^* k}\,. \tag{3.17}$$

Similarly, for the standard k–ω model, the default model constants are:

$$\begin{aligned} &\beta^* = 0.09, && C_{\omega 1} = 0.52, && C_{\omega 2} = 0.072, \\ &\sigma_k = 2.0, && \sigma_\omega = 2.0\,. \end{aligned}$$

These constants are calibrated based on experimental data and are commonly used in engineering applications. However, variations or modifications may be found in literature to improve model performance in specific flow configurations.

Turbulent Energy Flux Closure

In the Favre-averaged energy equation, the turbulent energy flux term $\widetilde{\bar{\rho} u_k'' h''}$ arises from correlations between velocity and enthalpy fluctuations. To close this term, the gradient diffusion hypothesis is commonly employed, yielding the following relation:

$$\widetilde{\bar{\rho} u_k'' h''} = -\frac{\mu_t}{\mathrm{Pr}_t} \frac{\partial \widetilde{h}}{\partial x_k} \tag{3.18}$$

Here, μ_t is the turbulent dynamic viscosity [Pa·s], $\widetilde{h}$ is the Favre-averaged total enthalpy [J/kg], and Pr_t is the turbulent Prandtl number. This number serves as an analog to the laminar Prandtl number and quantifies the ratio of turbulent momentum diffusivity to turbulent thermal diffusivity.

In practice, Pr_t is often treated as a constant, with values typically ranging from 0.75 to 1.0. Although this simplification is computationally convenient, it may introduce errors in flows with strong heat transfer gradients, especially in reacting or compressible turbulent flows. Some advanced turbulence models allow for a dynamically computed Pr_t [60], but such approaches are rarely used in industrial RANS simulations due to added complexity.

Turbulent Species Mass Flux Closure

Similarly, the turbulent mass flux of species j, represented by the correlation $\rho u_k'' Y_j''$, must be closed to solve the species transport equation. Using the gradient diffusion assumption, the flux is modeled as:

$$\widetilde{\bar{\rho} u_k'' Y_j''} = -\frac{\mu_t}{\mathrm{Sc}_{t,j}} \frac{\partial \widetilde{Y}_j}{\partial x_k} = -D_{t,k} \frac{\partial \widetilde{Y}_j}{\partial x_k} \tag{3.19}$$

Here, $\widetilde{Y}_j$ is the Favre-averaged mass fraction of species j, $\mathrm{Sc}_{t,j}$ is the turbulent Schmidt number for species j, and $D_{t,k}$ is the turbulent mass diffusivity [m^2/s] defined as $D_{t,k} = \mu_t / \mathrm{Sc}_{t,j}$. Like the turbulent Prandtl number, $\mathrm{Sc}_{t,j}$ is usually assumed to be constant, typically in the range of 0.7 to 0.9 for gaseous flows.

It is also common practice to neglect the contribution of laminar diffusion terms, such as $\bar{\rho} V_{j,k} Y_j$, and thermal conduction $\lambda \frac{\partial \tilde{T}}{\partial x_k}$, under the assumption that turbulent transport dominates in high Reynolds number flows.

3.2. Turbulent Combustion Modelling

Turbulent combustion involves the complex interaction of chemical reactions with fluctuating velocity fields and scalar gradients. Unlike laminar flames, turbulent flames are wrinkled, stretched, and dynamically distorted by eddies across spatial and temporal scales. In practical CFD simulations, especially within the RANS framework, the instantaneous combustion process is modeled using statistically averaged quantities, necessitating appropriate closure models.

The governing transport equation for a progress variable c, which describes the transition from unburnt ($c = 0$) to burnt ($c = 1$) states, is given - after Favre averaging[36]:

$$\frac{\partial (\bar{\rho} \tilde{c})}{\partial t} + \frac{\partial}{\partial x_k} \left(\bar{\rho} \tilde{u}_k \tilde{c} \right) = \frac{\partial}{\partial x_k} \left[\bar{\rho} D \frac{\partial \tilde{c}}{\partial x_k} - \widetilde{\bar{\rho} u_k'' c''} \right] + \overline{\dot{\omega}}_c, \tag{3.20}$$

where $\tilde{c}$ is the Favre-averaged progress variable, $\bar{\rho}$ is the mean density, D is the molecular diffusivity, and $\overline{\dot{\omega}}_c$ is the mean chemical source term.

Two critical unclosed terms appear on the right-hand side of this equation:

- **Turbulent flux term** $\widetilde{\bar{\rho} u_k'' c''}$,
- **Mean chemical source term** $\overline{\dot{\omega}}_c$.

3.2.1. Closure of the Turbulent Scalar Flux

The turbulent scalar flux is typically closed using the gradient transport (or eddy diffusivity) hypothesis:

$$\widetilde{\bar{\rho} u_k'' c''} = -\bar{\rho} D_t \frac{\partial \tilde{c}}{\partial x_k}, \tag{3.21}$$

where D_t is the turbulent diffusivity, often related to the turbulent viscosity μ_t via the turbulent Prandtl or Schmidt number. For the progress variable, a typical assumption is $D_t = \mu_t / \rho \cdot Pr_t^{-1}$, where Pr_t is taken in the range 0.75 to 1.0 [60]. This closure reflects the dominant role of turbulent mixing compared to molecular diffusion in high-Reynolds-number flows.

3.2.2. Closure of the Mean Source Term

The closure of the mean source term $\overline{\dot{\omega}}_c$ depends on the flame structure and turbulence–chemistry interaction regime. Several modelling approaches are available to estimate the reaction rate under turbulent conditions:

Algebraic Models

Algebraic models encompass a class of combustion closures that assume the chemical reaction proceeds on timescales much shorter than those of turbulence (i.e., high Damköhler number $\mathrm{Da} \gg 1$). Under this assumption, the combustion rate is primarily controlled by turbulent mixing rather than detailed chemical kinetics. These models often employ empirical or semi-empirical formulations that relate the mean reaction rate to turbulence quantities such as the turbulent kinetic energy k, its dissipation rate ε, or the scalar dissipation rate.

One of the most widely used models in this category is the *Eddy Break-Up (EBU)* model, originally proposed by Magnussen and Hjertager [61] and later refined by Bray [62] . The EBU model assumes that combustion is limited by the rate at which turbulent eddies mix reactants and products, and therefore models the mean chemical source term as:

$$\overline{\dot{\omega}}_c = C_{EBU}\, \bar{\rho} \frac{\varepsilon}{k} \tilde{c}(1 - \tilde{c}), \tag{3.22}$$

where C_{EBU} is an empirical model constant, ε is the turbulent dissipation rate, k is the turbulent kinetic energy, and $\tilde{c}$ is the Favre-averaged progress variable. This model treats combustion as a single-step irreversible process and assumes a unity Lewis number and ideal gas behavior.

While the EBU model is simple and computationally efficient, it presents several limitations: it tends to overestimate reaction rates in highly strained regions due to the large ε/k ratio and requires careful tuning of C_{EBU} for each case. Moreover, due to its lack of detailed chemistry, the model may not accurately capture flame quenching, re-ignition, or flame structure in complex or highly turbulent regimes.

Presumed PDF (pPDF) Models

Presumed PDF models aim to account for the sub-grid scale variability of the mixture fraction Z by integrating over a presumed distribution. The mean chemical source term $\overline{\dot{\omega}}$ is then computed as [36]:

$$\overline{\dot{\omega}} = \int_0^1 \dot{\omega}(Z)\, P(Z)\, dZ, \tag{3.23}$$

where $\dot{\omega}(Z)$ is the reaction rate as a function of the local mixture fraction, typically pre-tabulated from one-dimensional laminar flamelets, and $P(Z)$ is the probability density function of Z.

A commonly used presumed form for $P(Z)$ is the beta-distribution:

$$P(Z) = \frac{\Gamma(a+b)}{\Gamma(a)\Gamma(b)} Z^{a-1}(1-Z)^{b-1} \tag{3.24}$$

which is bounded between 0 and 1 and flexible enough to capture skewed distributions often seen in turbulent reactive flows. The shape parameters a and b are computed using the mean and variance of the mixture fraction $\tilde{Z}$ and $\widetilde{Z''^2}$:

$$a = \tilde{Z}\left(\frac{\tilde{Z}(1-\tilde{Z})}{\widetilde{Z''^2}} - 1\right), \tag{3.25}$$

$$b = (1-\tilde{Z})\left(\frac{\tilde{Z}(1-\tilde{Z})}{\widetilde{Z''^2}} - 1\right). \tag{3.26}$$

To accurately model this PDF, the variance $\widetilde{Z''^2}$ must be computed using a transport equation (eqn 3.29). While the pPDF method offers a physically robust approach to model the effects of turbulence–chemistry interaction, its application increases the computational cost due to the need for additional scalar transport equations and integration steps over the local PDFs. Nonetheless, its ability to capture local composition fluctuations makes it particularly suitable for partially premixed and stratified flow environments.

In many practical implementations, the PDF of the progress variable c is assumed to be a delta function-implying that c takes a single value for a given Z for simplicity. However, when fluctuations in c are significant, a beta distribution may be used. In partially premixed combustion, a joint PDF $P(Z,c)$ is sometimes employed to account for correlations between mixture composition and reaction progress.

3.2.3. Mixture Fraction and Variance

The mean mixture fraction $\widetilde{Z}$ satisfies the following transport equation:

$$\frac{\partial}{\partial t}\left(\bar{\rho}\widetilde{Z}\right) + \frac{\partial}{\partial x_i}\left(\bar{\rho}\widetilde{u}_i\widetilde{Z}\right) = \frac{\partial}{\partial x_i}\left(\bar{\rho}\bar{D}\frac{\partial \widetilde{Z}}{\partial x_i}\right) + \frac{\partial}{\partial x_i}\left(\bar{\rho}D_t\frac{\partial \widetilde{Z}}{\partial x_i}\right), \tag{3.27}$$

where $\bar{D}$ is the molecular diffusivity and D_t is the turbulent diffusivity of Z.

The variance of the mixture fraction, $\widetilde{Z''^2}$, quantifies the intensity of local scalar fluctuations in a turbulent flow field. It plays a critical role in constructing the presumed PDF, especially when using beta-function closures. The variance is defined as:

$$Z''^2 = \frac{\overline{\rho(Z-\widetilde{Z})^2}}{\bar{\rho}}, \tag{3.28}$$

where Z is the instantaneous mixture fraction and $\widetilde{Z}$ is its Favre-averaged mean.

In Unsteady Reynolds-Averaged Navier–Stokes (URANS) simulations, $\widetilde{Z''^2}$ is computed by solving a separate transport equation [36]:

$$\begin{aligned}\frac{\partial}{\partial t}\left(\bar{\rho}\widetilde{Z''^2}\right) + \frac{\partial}{\partial x_i}\left(\bar{\rho}\widetilde{u}_i\widetilde{Z''^2}\right) = \frac{\partial}{\partial x_i}\left(\rho D\frac{\partial Z''^2}{\partial x_i}\right) + 2Z''\frac{\partial}{\partial x_i}\left(\rho D\frac{\partial \widetilde{Z}}{\partial x_i}\right) \\ + \frac{\partial}{\partial x_i}\left(\bar{\rho}D_t\frac{\partial \widetilde{Z''^2}}{\partial x_i}\right) + C_g\mu_t\left(\frac{\partial \widetilde{Z}}{\partial x_i}\right)^2 - C_d\bar{\rho}\frac{\varepsilon}{k}\widetilde{Z''^2}\end{aligned} \tag{3.29}$$

where D and D_t are the molecular and turbulent diffusivities of the mixture fraction, respectively, and μ_t is the turbulent viscosity. The coefficients C_g and C_d represent the scalar production and dissipation constants, respectively.

In the limiting case of steady-state and negligible transport, the production and dissipation terms are in equilibrium:

$$C_g \mu_t \left(\frac{\partial \widetilde{Z}}{\partial x_i} \right)^2 = C_d \bar{\rho} \frac{\varepsilon}{k} \widetilde{Z''^2}. \tag{3.30}$$

This relation enables the approximate evaluation of $\widetilde{Z''^2}$ in terms of local turbulence quantities:

$$\widetilde{Z''^2} = \left(\frac{C_g}{C_d} \cdot \frac{k}{\bar{\rho}\,\varepsilon} \right) \mu_t \left(\frac{\partial \widetilde{Z}}{\partial x_i} \right)^2 \tag{3.31}$$

From this expression, it becomes evident that steeper gradients in $\widetilde{Z}$, as often encountered in stratified or partially premixed flows, significantly amplify the variance due to a quadratic dependence. This makes the mixture fraction variance a sensitive marker for localized scalar stratification. Furthermore, since $\mu_t \sim \bar{\rho}\, k^2/\varepsilon$, the magnitude of turbulence also directly influences the extent of local composition variability.

Accurate computation of $\widetilde{Z''^2}$ is therefore essential for the fidelity of beta-PDF-based turbulent combustion models, particularly in the simulation of hydrogen combustion and steam-rich environments where sharp composition gradients and high diffusivity dominate the flow physics.

Now that the mean mixture fraction and its variance have been defined, along with their transport equations, we can proceed to complete the discussion of different approaches for calculating the mean chemical source term.

Flame Surface Density (FSD) Models

Flame surface density (FSD) models represent turbulent premixed combustion as an ensemble of thin, wrinkled laminar flamelets embedded in a turbulent flow field. The core idea is to express the mean chemical source term as the product of a local reaction rate per unit flame surface and the flame surface area per unit volume (the *flame surface density* Σ, in $\mathrm{m}^2/\mathrm{m}^3$):

$$\overline{\dot{\omega}}_c = \dot{\Omega}\,\Sigma \tag{3.32}$$

A common assumption is to approximate the reaction rate per flame surface $\dot{\Omega}$ by the density of the unburnt gases times the laminar flame speed, yielding:

$$\overline{\dot{\omega}}_c = \rho_u\, S_L\, \Sigma \tag{3.33}$$

This form has the advantage of clearly separating the chemical contribution ($\rho_u S_L$) from the geometric contribution (Σ) in the source term. The challenge is then to provide a suitable closure for Σ, either through an *algebraic expression* or via a *transport equation* for its evolution.

Flame Wrinkling Factor: In practice, it is common to relate Σ to the flame surface resolved on the computational mesh via a *flame wrinkling factor* Ξ, defined as the ratio of the true flame surface density to the surface density captured by the resolved flame front (often approximated by $|\nabla \tilde{c}|$):

$$\Sigma = \Xi\, |\nabla \tilde{c}| \tag{3.34}$$

Substituting into Eq. 3.33 gives:

$$\overline{\dot{\omega}}_c = \rho_u\, S_L\, \Xi\, |\nabla \tilde{c}| \tag{3.35}$$

Moreover, the flame wrinkling factor is equal to the ratio of turbulent to unstrained laminar flame speed, i.e. $\Xi = S_T/S_L$ assuming equilibrium conditions. The modelling of Ξ is therefore central to FSD approaches. Two broad strategies exist:

- **Algebraic Wrinkling Models**, where Ξ is expressed via empirical or semi-empirical correlations based on local turbulence parameters.

- **Transport-Based Wrinkling Models**, where an additional equation for Ξ or Σ is solved to capture its spatial and temporal evolution.

In this work, the focus is on algebraic wrinkling models, specifically:

- Turbulent Flame Speed Closure (TFC) [63]
- Extended Turbulent Flame Speed Closure (ETFC) [53]

which are described below.

- *Turbulent Flame Speed Closure (TFC) [63]:* Developed by Zimont, the TFC model assumes that the flame surface area scales with the turbulence intensity u' and the integral length scale. It is one of the earliest algebraic models and provides a straightforward closure for the turbulent flame speed S_T based on turbulence parameters. The turbulent diffusivity is modeled as:

$$D_t = D_t^{\infty} = \frac{C_\mu}{\mathrm{Pr}_t}\frac{k^2}{\varepsilon}, \tag{3.36}$$

  where C_μ is a turbulence model constant,D_t^{∞} is the asymptotic turbulent diffusivity, Pr_t is the turbulent Prandtl number, k is the turbulent kinetic energy, and ε is the turbulent dissipation rate.

  The turbulent flame speed S_T is then approximated using a Damköhler number-based relation:

$$S_T = S_T^{\infty} = Au'\,\mathrm{Da}^{1/4} = Au'\left(\frac{l_t}{u'\tau_c}\right)^{1/4}, \tag{3.37}$$

  where A is a model constant, l_t is the turbulent integral length scale, and τ_c is the chemical time scale of the corresponding laminar flame, given by:

$$\tau_c = \frac{\alpha_u}{(S_{L,0})^2}, \tag{3.38}$$

  where α_u is the thermal diffusivity of unburnt gases and $S_{L,0}$ is the unstrained laminar flame speed.

- *Extended Turbulent Flame Speed Closure (ETFC) [53]:* Proposed by Lipatnikov and Chomiak, ETFC introduces modifications to the original TFC to improve its applicability across a wider range of flame regimes. It corrects for deficiencies in predicting flame quenching or re-ignition by incorporating time-dependent flame development and a laminar source term. Specifically, the model accounts for the transient buildup of turbulence by introducing a time-dependent turbulent flame speed S_t and turbulent diffusivity $D_t(t)$, expressed as:

$$D_t(t) = D_t^{\infty}\left[1 - e^{-t/\tau_L}\right] = \frac{C_\mu}{\mathrm{Pr}_t}\frac{k^2}{\varepsilon}\left[1 - e^{-t/\tau_L}\right], \tag{3.39}$$

$$S_T = S_T^{\infty}\left[1 + \frac{\tau_L}{t}\left(e^{-t/\tau_L} - 1\right)\right]^{1/2} = Bu'\,\mathrm{Da}^{1/4}\left[1 + \frac{\tau_L}{t}\left(e^{-t/\tau_L} - 1\right)\right]^{1/2}, \tag{3.40}$$

  where:

  - t is the time since ignition (flame development time),
  - τ_L is the Lagrangian timescale of turbulence,
  - D_t^{∞} is the asymptotic turbulent diffusivity,
  - C_μ is a turbulence model constant,
  - Pr_t is the turbulent Prandtl number,
  - k is the turbulent kinetic energy,
  - ε is the turbulence dissipation rate,
  - u' is the root-mean-square of the turbulent velocity fluctuations,

- Da is the Damköhler number,
- B is a model constant (often taken equal to the TFC constant A).

The timescale τ_L is computed via dimensional analysis as:

$$\tau_L = \frac{D_t^{\infty}}{u'^2} = \frac{1}{u'^2} \cdot \frac{C_\mu}{\mathrm{Pr}_t} \frac{k^2}{\varepsilon}. \tag{3.41}$$

In these models, as mentioned above, the source term is typically expressed as:

$$\bar{\dot{\omega}}_c = \bar{\rho} S_T |\nabla \tilde{c}| = \bar{\rho_u} \, S_L \, \Xi \, |\nabla \tilde{c}| \tag{3.42}$$

where S_T is defined through the selected flame speed correlation.

Transport-Based Models offer a more detailed representation by solving an additional transport equation for the flame surface density Σ or the wrinkling factor Ξ. These models can better capture the spatial and temporal evolution of flame geometry, especially in complex or unsteady flow configurations.

Finally, the turbulent diffusivity D_t used in these models may be enhanced using time-dependent formulations, such as those based on the Lagrangian time scale τ_L, to more accurately reflect transient diffusion effects:

$$D_t(t) = \frac{C_\mu}{Sc_t} \frac{k^2}{\varepsilon} \left(1 - e^{-t/\tau_L}\right), \tag{3.43}$$

where C_μ is a turbulence model constant, and Sc_t is the turbulent Schmidt number.

These FSD models provide a flexible framework for capturing the interaction of turbulence and flame propagation in premixed combustion, making them a valuable tool in the modeling of turbulent reacting flows.

Summary

The modelling of turbulent combustion within the RANS framework necessitates closure strategies for both scalar transport and mean reaction rate. While algebraic models like EBU provide simplicity and computational efficiency, PDF-based and flame surface density (FSD) models offer greater physical realism by explicitly accounting for turbulence–flame interactions. The choice of model must balance accuracy with computational cost, depending on the flame regime and application context.

In the next chapter, the specific transport equations and modelling assumptions adopted in this study will be discussed in detail, as part of the numerical methodology. This includes the implementation of the Favre-averaged transport equations, as well as the algebraic and transport-based formulations for the flame wrinkling factor Ξ. The selection and application of turbulent flame speed correlations will also be elaborated with their governing expressions and model constants.

4

Numerical Methodology

This chapter outlines the numerical framework used to simulate turbulent premixed combustion in `OpenFOAM` [22]. The simulation approach is based on the finite volume method (FVM), with pressure-velocity coupling handled using the SIMPLE, PISO, and PIMPLE algorithms, along with transonic corrections for compressible flow stability. The `XiFoam` solver is employed for combustion modeling, and its validity is first assessed using Sod's shock tube problem. Key turbulent combustion modeling components - such as flame radius extraction, thermophysical property specification, laminar flame speed correlations, and flame wrinkling factor models are also introduced. Together, these tools form the computational foundation for the combustion simulations discussed in this chapter. The structure of `OpenFOAM` is discussed in Appendix B.1.

4.1. Finite Volume Method

`OpenFOAM` employs the finite volume method (FVM) to discretize and solve partial differential equations (PDEs) arising in fluid dynamics and combustion. The FVM is particularly suited for conservation laws, as it ensures that conserved quantities such as mass, momentum, and energy remain conserved across the computational domain.

A general transport equation for a scalar quantity f can be written in its differential form as [64]:

$$\underbrace{\frac{\partial}{\partial t}(\rho f)}_{\text{Temporal derivative}} + \underbrace{\frac{\partial}{\partial x_i}(\rho u_i f)}_{\text{Convective term}} - \underbrace{\frac{\partial}{\partial x_i}\left(\rho D \frac{\partial f}{\partial x_i}\right)}_{\text{Diffusion term}} = \underbrace{S_f(f)}_{\text{Source term}} \quad . \tag{4.1}$$

To apply the FVM, this equation is integrated over a control volume V:

$$\iiint_V \frac{\partial}{\partial t}(\rho f)\, dV + \iiint_V \frac{\partial}{\partial x_i}(\rho u_i f)\, dV - \iiint_V \frac{\partial}{\partial x_i}\left(\rho D \frac{\partial f}{\partial x_i}\right) dV = \iiint_V S_f(f)\, dV \,. \tag{4.2}$$

The convective and diffusive terms can be transformed into surface integrals using the Gauss divergence theorem:

$$\iiint_V \frac{\partial f}{\partial x_i}\, dV = \iint_{\partial V} f\, dS_i \,, \tag{4.3}$$

where dS_i represents the oriented infinitesimal surface element pointing outward from the control volume boundary ∂V. This formulation naturally converts volume-based fluxes into surface fluxes across control volume faces, aligning with the cell-centered structure used in OpenFOAM.

OpenFOAM handles the discretization and interpolation of these terms internally using well-established FVM schemes. This allows users to focus on setting up physical models and boundary conditions, while the numerical infrastructure ensures conservative and stable solution procedures.The specific spatial and temporal discretization schemes employed in these simulations are not detailed in this thesis.

4.2. Pressure–Velocity Coupling

In compressible flow simulations, the momentum and continuity equations are tightly coupled through the pressure and velocity fields. To decouple and solve them efficiently, segregated algorithms such as SIMPLE [64], PISO [64], and PIMPLE [64] are used. These rely on deriving an equation for pressure from the discretized momentum and continuity equations.

Starting with the semi-discretized form of the Favre-averaged momentum equation (refer to Equation (3.4)), we retain the pressure gradient in its original form and rewrite the equation as:

$$\mathbf{M}\,\tilde{\mathbf{U}} = \mathbf{r} - \nabla\tilde{p}, \tag{4.4}$$

where:

- $\mathbf{M}$ is the full coefficient matrix from discretization,
- $\tilde{\mathbf{U}}$ is the vector of Favre-averaged velocity components,
- $\nabla\tilde{p}$ is the pressure gradient term,
- $\mathbf{r}$ is a source term that may include contributions from time discretization and non-linear terms.

$$\underbrace{\begin{bmatrix} a_{1,1} & a_{1,2} & a_{1,3} & \cdots & a_{1,n} \\ a_{2,1} & a_{2,2} & a_{2,3} & \cdots & a_{2,n} \\ a_{3,1} & a_{3,2} & a_{3,3} & \cdots & a_{3,n} \\ \vdots & \vdots & \vdots & \ddots & \vdots \\ a_{n,1} & a_{n,2} & a_{n,3} & \cdots & a_{n,n} \end{bmatrix}}_{\text{Full momentum matrix } \mathbf{M}} \begin{bmatrix} \tilde{u}_1 \\ \tilde{u}_2 \\ \tilde{u}_3 \\ \vdots \\ \tilde{u}_n \end{bmatrix} = \begin{bmatrix} r_1 \\ r_2 \\ r_3 \\ \vdots \\ r_n \end{bmatrix} + \begin{bmatrix} \left(\frac{\partial\tilde{p}}{\partial x}\right)_1 \\ \left(\frac{\partial\tilde{p}}{\partial x}\right)_2 \\ \left(\frac{\partial\tilde{p}}{\partial x}\right)_3 \\ \vdots \\ \left(\frac{\partial\tilde{p}}{\partial x}\right)_n \end{bmatrix} \tag{4.5}$$

We perform a matrix decomposition of $\mathbf{M}$ into a diagonal matrix $\mathbf{A}$ and off-diagonal contributions. This gives:

$$a_P^u \tilde{u}_P + \sum_N a_N^u \tilde{u}_N = r - \nabla\tilde{p}, \tag{4.6}$$

where a_P^u and a_N^u are the diagonal and off-diagonal coefficients of the velocity equation for cell P and its neighbors N, respectively.

This matrix system can be represented explicitly as:

$$\underbrace{\begin{bmatrix} a_{1,1} & 0 & 0 & \cdots & 0 \\ 0 & a_{2,2} & 0 & \cdots & 0 \\ 0 & 0 & a_{3,3} & \cdots & 0 \\ \vdots & \vdots & \vdots & \ddots & \vdots \\ 0 & 0 & 0 & \cdots & a_{n,n} \end{bmatrix}}_{\text{Diagonal matrix } \mathbf{A}} \begin{bmatrix} \tilde{u}_1 \\ \tilde{u}_2 \\ \tilde{u}_3 \\ \vdots \\ \tilde{u}_n \end{bmatrix} + \underbrace{\begin{bmatrix} 0 & a_{1,2} & a_{1,3} & \cdots & a_{1,n} \\ a_{2,1} & 0 & a_{2,3} & \cdots & a_{2,n} \\ a_{3,1} & a_{3,2} & 0 & \cdots & a_{3,n} \\ \vdots & \vdots & \vdots & \ddots & \vdots \\ a_{n,1} & a_{n,2} & a_{n,3} & \cdots & 0 \end{bmatrix}}_{\text{Off-diagonal terms}} \begin{bmatrix} \tilde{u}_1 \\ \tilde{u}_2 \\ \tilde{u}_3 \\ \vdots \\ \tilde{u}_n \end{bmatrix} = \begin{bmatrix} r_1 \\ r_2 \\ r_3 \\ \vdots \\ r_n \end{bmatrix} + \begin{bmatrix} \left(\frac{\partial\tilde{p}}{\partial x}\right)_1 \\ \left(\frac{\partial\tilde{p}}{\partial x}\right)_2 \\ \left(\frac{\partial\tilde{p}}{\partial x}\right)_3 \\ \vdots \\ \left(\frac{\partial\tilde{p}}{\partial x}\right)_n \end{bmatrix} \tag{4.7}$$

We now define the velocity correction operator $\mathbf{H}(\mathbf{U})$ as:

$$\mathbf{H}(\mathbf{U}) = \mathbf{r} - \sum_N a_N^u \tilde{u}_N, \tag{4.8}$$

which gives the velocity in predictor form:

$$\tilde{u}_P = \frac{1}{a_P^u} \left(\mathbf{H}(\mathbf{U}) - \nabla \tilde{p} \right) \tag{4.9}$$

This predictor velocity is then substituted into the compressible Favre-averaged continuity equation (Equation (3.3)). Assuming a linearized compressibility relation:

$$\frac{\partial \tilde{\rho}}{\partial t} = \psi \frac{\partial \tilde{p}}{\partial t}, \tag{4.10}$$

we obtain the continuity equation:

$$\psi \frac{\partial \tilde{p}}{\partial t} + \nabla \cdot \left(\tilde{\rho} \cdot \frac{1}{a_P^u} \left(\mathbf{H}(\mathbf{U}) - \nabla \tilde{p} \right) \right) = 0. \tag{4.11}$$

Rearranging, the resulting pressure Poisson equation for compressible flow becomes:

$$\nabla \cdot \left(\tilde{\rho} \cdot \frac{1}{a_P^u} \nabla \tilde{p} \right) = \psi \frac{\partial \tilde{p}}{\partial t} + \nabla \cdot \left(\tilde{\rho} \cdot \frac{1}{a_P^u} \mathbf{H}(\mathbf{U}) \right). \tag{4.12}$$

This formulation forms the basis of the pressure–velocity coupling algorithms used in segregated solvers. It allows the continuity and momentum equations to be solved in a decoupled but consistent fashion while fully accounting for compressibility and pressure transients. The following section discusses the most commonly used algorithms used in literature.

4.2.1. Pressure-Velocity Coupling Algorithms

The segregated pressure-based solvers in OpenFOAM rely on iterative algorithms to resolve the coupling between pressure and velocity fields in compressible flows. The momentum equation is solved using a guessed pressure field, which does not, in general, satisfy the continuity equation. This inconsistency is corrected by solving a pressure Poisson equation derived by substituting the velocity predictor into the continuity equation. The three commonly used algorithms: SIMPLE, PISO, and PIMPLE differ in how and when this correction is performed within each time step.

SIMPLE (Semi-Implicit Method for Pressure Linked Equations)

The SIMPLE algorithm [64] is a widely used segregated approach originally developed for steady-state simulations. It decouples the continuity and momentum equations by using a pressure guess and iteratively correcting the velocity field to ensure mass conservation.

The algorithm begins with the *momentum predictor step*, where the Favre-averaged momentum equation (refer equation (3.4)) is solved using the pressure field from the previous iteration or time step. This yields an intermediate velocity field $\tilde{\mathbf{u}}^*$, which does not, in general, satisfy the Favre-averaged continuity equation (equation (3.3)).

Next, the pressure correction equation is obtained (refer equation 4.12) by substituting the predicted velocity into the continuity equation. Solving this pressure Poisson equation allows for a corrected pressure field, which is then used in the *velocity corrector step* to update the velocity via Equation (4.9).

This process is repeated iteratively in what is known as the SIMPLE loop (or outer loop), until both pressure and velocity fields converge and simultaneously satisfy the momentum and continuity equations.

PISO (Pressure-Implicit with Splitting of Operators)

The PISO algorithm [64] was developed for unsteady compressible flow problems and improves upon SIMPLE by incorporating multiple pressure corrections within a single time step. It begins with the

same *momentum predictor step*- solving Equation (3.4) using the known pressure field to obtain an intermediate velocity.

This velocity is then used to derive and solve the pressure Poisson equation (refer equation (4.12)) to enforce continuity. The pressure correction is used in a *velocity corrector step* - again using Equation (4.9) to update the velocity field.

Unlike SIMPLE, PISO then returns to the corrected velocity and performs additional pressure corrections within the same time step. These repeated corrector steps (known as the inner loop) increase the accuracy of the pressure-velocity coupling in transient simulations.

By performing multiple corrections per time step, the PISO algorithm ensures better temporal accuracy without the need for an outer iteration loop.

PIMPLE (Merged SIMPLE and PISO)

The PIMPLE algorithm [64] combines SIMPLE's outer loop structure with PISO's inner pressure corrections. It is particularly suited for unsteady flows at high Courant numbers ($\mathrm{Co}_{\max} \gg 1$), where under-relaxation and multiple corrections per time step are needed for numerical stability.

Within each time step, one or more inner PISO-like pressure corrections are performed, followed by one or more outer SIMPLE-like loops. Depending on the number of inner and outer iterations, the PIMPLE algorithm can resemble either PISO or SIMPLE:

- One outer + multiple inner corrections $\Rightarrow$ PISO-like behavior,
- Multiple outer + one inner correction $\Rightarrow$ SIMPLE-like behavior.

PIMPLE provides flexibility in balancing stability and convergence, and is thus adopted in this thesis for all compressible, transient flow simulations.

Motivation for Pressure-Based Solvers

Numerical methods for solving the Navier–Stokes equations are usually grouped into pressure-based and density-based approaches, depending on how the governing equations are arranged and which variables are solved for directly. Density-based methods are traditionally used for high-speed compressible flows. In these methods, density is treated as a primary variable, and pressure is obtained from the equation of state. While this works well when there are strong compressibility effects (such as shocks or large temperature gradients), it becomes problematic at low Mach numbers where density changes are small and the coupling between pressure and density becomes weak [65].

Pressure-based methods, on the other hand, solve for pressure directly and treat density as a derived quantity. One major advantage is that pressure remains a well-behaved variable across all Mach numbers. This makes pressure-based solvers more robust in low-speed and mixed-flow regimes. Unlike density-based methods, they can also handle incompressible or low-Mach flows without artificial modifications like pseudo-compressibility or preconditioning.

Because of these reasons, a pressure-based segregated approach is used in this thesis. It allows the solver to operate across a wide range of Mach numbers while still remaining stable and consistent with the physics. However, this comes with some trade-offs,especially at high Mach numbers, where the pressure-velocity coupling becomes weaker. This is discussed in the next section.

Applicability and Limitations of Pressure-Based Solvers

In supersonic flows, the coupling between pressure and velocity breaks down gradually. This happens because the continuity and momentum equations rely more on density changes than on pressure changes. As a result, standard pressure-based methods can struggle to accurately capture flow features like shocks, expansion fans, or discontinuities [66].

Several modifications have been proposed in the literature to address this. These include compressibility corrections [64, 66], energy-consistent pressure discretization, and other formulations that are more suited to high-speed regimes. In pressure based solvers in `OpenFOAM`, such corrections have

been applied and tested to extend the applicability of pressure-based methods to the transonic and supersonic regimes. The full details of the formulation and the `OpenFOAM` implementation are presented in Appendix A.2.

The following section will present the formulation of the baseline `XiFoam` solver, outlining its governing equations and numerical algorithm. Once the base solver is established, its performance together with the applied compressibility corrections will be assessed using the standard Sod shock tube problem. This benchmark, which contains both subsonic and supersonic regions separated by a shock, provides an ideal first test to verify that the solver can accurately capture transonic transitions while maintaining the robustness of the pressure-based framework across a wide range of Mach numbers.

4.3. XiFoam Solver

4.3.1. Overview

`XiFoam` is a pressure-based, segregated solver in `OpenFOAM` developed to simulate turbulent premixed combustion using the b-Ξ [67] model. It extends the capabilities of `rhoPimpleFoam` by including additional transport equations for combustion dynamics. Despite its formulation for low-Mach and incompressible flows, several studies have demonstrated its robustness in handling shock waves and compressible flow regimes.

The solver simultaneously evolves the momentum, pressure, energy, and scalar equations, including the regress variable b, and flame surface density effects through the wrinkling factor Ξ. These equations are solved within the PIMPLE loop to ensure tight coupling between combustion chemistry and fluid dynamics. This is discussed in section 4.3.3.

4.3.2. Regress Variable Formulation

To track the burned and unburned zones of the mixture, XiFoam uses the *regress variable* b, defined as:

$$b = 1 - c \tag{4.13}$$

where c is the combustion progress variable. Here, $b = 1$ corresponds to unburned gases and $b = 0$ to fully burned gases. The transport equation for b, derived from the Favre-averaged scalar transport (see equation 3.20), is written as:

$$\frac{\partial}{\partial t}(\tilde{\rho}\,\tilde{b}) + \frac{\partial}{\partial x_k}(\tilde{\rho}\,\tilde{u}_k\,\tilde{b}) - \frac{\partial}{\partial x_k}\left(\tilde{\rho}\,D_{\text{eff}}\frac{\partial \tilde{b}}{\partial x_k}\right) = \widetilde{\dot{\omega}_c}, \tag{4.14}$$

where D_{eff} is the effective diffusivity and $\widetilde{\dot{\omega}_c}$ is the source term modeled via the FSD Model.

$$\widetilde{\dot{\omega}_c} = -\tilde{\rho}_u S_L \Xi \left|\widetilde{\nabla b}\right| \tag{4.15}$$

with S_L being the laminar flame speed.

This formulation improves numerical stability and is particularly useful during ignition and flame propagation, where a clear distinction between burned and unburned zones is essential. The descriptions for calculating S_L, Ξ will be explained in later sections in this chapter.

4.3.3. Numerical Procedure

The equations for velocity $\widetilde{\mathbf{u}}$, pressure $\widetilde{p}$, regress variable $\widetilde{b}$, flame wrinkling factor Ξ, and total energy are solved in a tightly coupled fashion within each time step using a PIMPLE-based outer iteration. A schematic of the numerical procedure implemented in XiFoam is shown in Figure 4.1. Each simulation step in XiFoam involves advancing the time, solving the continuity equation, and sequentially solving the equations for momentum, the regress variable b, flame wrinkling, and energy. The pressure equation is then solved using the velocity predictor, and this loop continues until both the pressure and the overall solution converge.

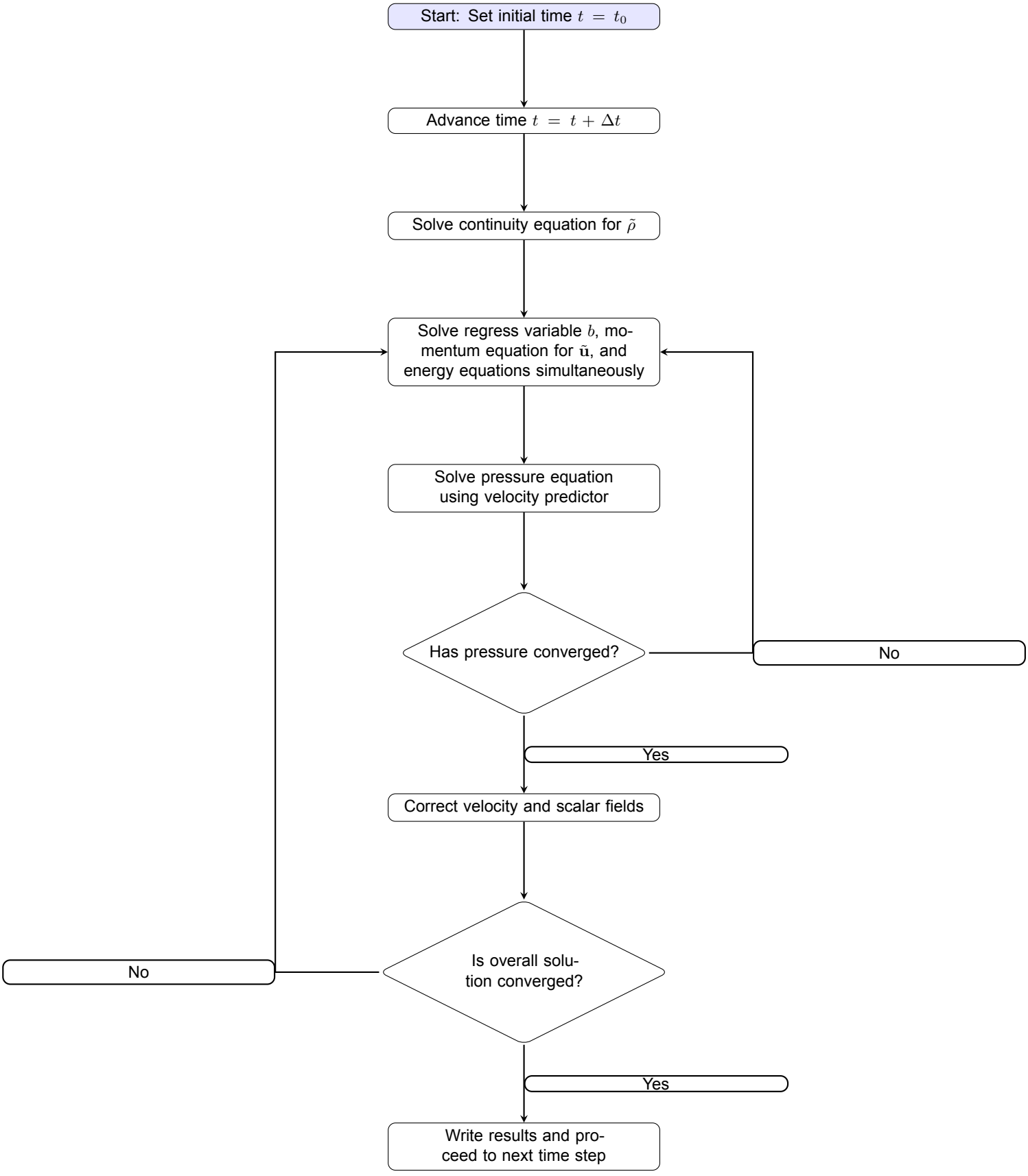

Figure 4.1: Flowchart of XiFoam solver algorithm.

4.4. Validation with Sod's Shock Tube Problem

Before applying XiFoam to reactive flow cases, it is essential to evaluate its ability to handle compressible flow phenomena such as shocks, rarefaction waves, and contact discontinuities. As discussed earlier in the context of solver applicability, the performance of pressure-based algorithms in transonic and supersonic regimes requires careful assessment. To this end, the classical Sod's shock tube problem is considered as a validation case.

Originally proposed by Sod in 1978 , this one-dimensional Riemann problem is a standard benchmark in computational fluid dynamics [68]. It captures all three fundamental discontinuities - shock waves, contact surfaces, and rarefaction waves - and provides an exact analytical solution against which numerical results can be compared. This test case thus serves as a robust benchmark for assessing the shock-capturing capability and accuracy of the compressible solver.

4.4.1. Description of the Sod tube test case

The computational domain spans a unit-length channel in the x-direction, with the initial condition consisting of a diaphragm placed at the center ($x = 0.5$ m)(see figure 4.2). The diaphragm separates two regions of gas with distinctly different initial thermodynamic states. Upon diaphragm removal at $t = 0$, a series of waves emanates from the discontinuity, generating five physically distinct regions(see figure 4.3). These include two undisturbed initial states on either end (Regions I and V), a rarefaction wave, a contact surface, and a shock wave propagating rightward. The fluid in each region is at rest but has distinct thermodynamic properties, leading to the development of non-linear wave phenomena upon diaphragm removal.

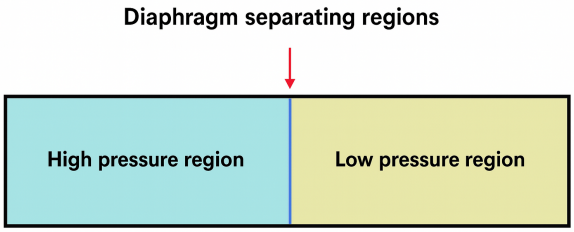

Figure 4.2: Sod Shock tube Schematic

The initial state of the system is defined by a piecewise distribution of density and pressure:

$$\rho(x,0) = \begin{cases} \rho_L = 1.0 & \text{for } x < 0.5, \\ \rho_R = 0.125 & \text{for } x > 0.5, \end{cases}$$

$$p(x,0) = \begin{cases} p_L = 1.0 & \text{for } x < 0.5, \\ p_R = 0.1 & \text{for } x > 0.5, \end{cases}$$

$$u(x,0) = 0 \quad \text{for all } x.$$

These conditions define a Riemann problem for the Euler equations, and the resulting evolution is governed entirely by compressible dynamics without viscosity or thermal diffusion.

Once the diaphragm (see figure 4.2) is removed at $t = 0$, the initial discontinuity evolves into three distinct wave structures that propagate in opposite directions, leading to five distinct regions in the domain, as shown in figure 4.3:

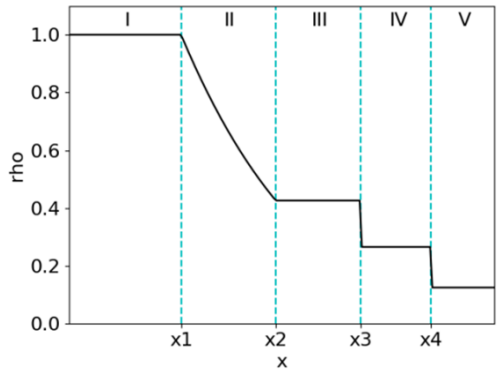

Figure 4.3: Exact solution of the density profile. at t = 0.1 s

- **Region 1 ($x < x_1$):** This is the undisturbed high-pressure region to the left of the rarefaction wave. All flow quantities remain constant and equal to the left initial values.
- **Region 2 ($x_1 < x < x_2$):** Here, the rarefaction wave expands into the high-pressure region. Flow variables such as density, velocity, and pressure vary smoothly. This expansion fan accelerates the flow and decreases its density and pressure.
- **Region 3 ($x_2 < x < x_3$):** A region of uniform flow lies between the rarefaction wave and the contact discontinuity. Pressure and velocity remain constant and continuous here, but density changes across the next region.
- **Region 4 ($x_3 < x < x_4$):** This region lies between the contact discontinuity and the shock front. While pressure and velocity are still continuous across the contact surface, density and temperature exhibit a discontinuity.
- **Region 5 ($x > x_4$):** The rightmost region represents the undisturbed low-pressure fluid. Similar to Region 1, all properties remain at their initial right-side values.

Wave Characteristics

- **Shock Wave:** Propagates into the low-pressure region on the right. It compresses the fluid, increasing both density and pressure abruptly.
- **Rarefaction Wave:** Moves into the left high-pressure region, causing an expansion of the gas and a gradual decrease in pressure and density.
- **Contact Discontinuity:** Lies between the two wave fronts. Here, there is a discontinuity in density and temperature, but the pressure and velocity remain continuous.

Each of these structures arises as a direct consequence of the hyperbolic nature of the Euler equations and represents one of the fundamental building blocks of compressible flow. The Sod shock tube problem remains a benchmark for evaluating the capability of CFD solvers in accurately capturing these non-linear features, primarily because an analytical solution exists and can be directly compared against numerical predictions.

Two solvers from the OpenFOAM framework were assessed for this case:

- `XiFoam`: A pressure-based transient solver for combustion, developed on top of `rhoPimpleFoam`, with a segregated solution strategy.
- `rhoCentralFoam`: A density-based solver that solves the governing conservation equations in their conservative form using a central-upwind Godunov-type scheme [69]. It evolves the flow field by explicitly updating density, momentum, and energy, while pressure is recovered through the equation of state. This approach naturally satisfies the continuity equation and is particularly well-suited for compressible flows involving shocks, expansions, and other wave phenomena. As a result, `rhoCentralFoam` provides robust shock-capturing capabilities and serves as a reliable reference in high-Mach number regimes.

4.4.2. Numerical Simulation Setup

The original tutorial for Sod's problem in OpenFOAM is based on the `rhoCentralFoam` solver, which is specifically designed for solving compressible flows using the density-based formulation. This case was adapted for use with `XiFoam`, and necessary modifications to the solver configuration, thermophysical properties, and numerical schemes were made to ensure consistency and stability of the adapted setup.

The computational domain consists of a one-dimensional geometry extending from $x = 0$ to $x = 1$, with the fluid initially separated by a diaphragm at the midpoint ($x = 0.5$). A uniform hexahedral mesh was used, discretized in the x-direction while maintaining a single cell in the other two directions to enforce one-dimensional behavior.

The complete set of test cases used in this study is summarized in Tables 4.1–4.3. The default initial conditions of the Sod shock tube problem generate a subsonic flow field, with the resulting maximum Mach number reaching approximately 0.93. To evaluate the solver's robustness in the supersonic regime, it becomes essential to modify the initial thermodynamic states - particularly pressure and density - such that the resulting flow field includes stronger shock and expansion features. The high Mach number cases defined in Table 4.3 enable a progressive assessment of solver performance as compressibility effects become increasingly dominant.

First, a mesh sensitivity analysis was conducted for the subsonic case using three resolutions at a fixed Courant number of 0.1 (Table 4.1). Based on the results, mesh M2 (600 cells) was selected for further testing. Next, a Courant number sensitivity study was carried out using this mesh (Table 4.2), from which Co $= 0.1$ was determined to be optimal. This configuration was then carried forward into the supersonic test cases (Table 4.3) to evaluate solver robustness under high-Mach number flow. In addition, the importance of appropriate numerical schemes for supersonic shock-capturing (see section 4.2.1) was investigated by comparing results obtained with different time integration schemes, as discussed in the following sections.

Table 4.1: Mesh sensitivity study for subsonic Sod case ($M \approx 0.93$), performed at fixed Courant number Co $= 0.1$.

Case	Mach Number	Mesh Resolution	Courant Number
MS_M1	0.93 (Subsonic)	300 cells	0.1
MS_M2	0.93 (Subsonic)	600 cells	0.1
MS_M3	0.93 (Subsonic)	1200 cells	0.1

Table 4.2: Courant number sensitivity study for subsonic Sod case ($M \approx 0.93$), performed using mesh M2 (600 cells).

Case	Mach Number	Mesh Resolution	Courant Number
CFL_005	0.93 (Subsonic)	600 cells	0.05
CFL_01	0.93 (Subsonic)	600 cells	0.1
CFL_05	0.93 (Subsonic)	600 cells	0.5
CFL_1	0.93 (Subsonic)	600 cells	1.0

Table 4.3: Final solver setup for all Sod cases using optimal mesh and Courant number from previous sensitivity studies.

Case	Mach Number	Mesh Resolution	Courant Number
SOD_M0.93	0.93 (Subsonic)	600 cells	0.1
SOD_M1.5	1.5 (Supersonic)	600 cells	0.1
SOD_M2.0	2.0 (Supersonic)	600 cells	0.1

All meshes were generated using the `blockMesh` utility and share identical boundary and initial conditions, enabling direct comparison of solution accuracy and convergence behavior. The initial condition

defines a classic Riemann problem with two quiescent fluid regions characterized by different thermodynamic states:

$$(p_L,\, U_L,\, \rho_L) = (1.0,\, 0.0,\, 1.0)\,, \qquad (p_R,\, U_R,\, \rho_R) = (0.1,\, 0.0,\, 0.125)$$

To satisfy OpenFOAM's requirement of specifying temperature instead of density, the initial temperatures were computed using the ideal gas law. The molar mass was set to $M = 0.02897$ kg/mol (corresponding to dry air), and the resulting temperatures were:

$$(T_L,\, T_R) = (0.00348,\, 0.00278)\ \mathrm{K}$$

For the supersonic test cases, the left state is varied while maintaining the right-side conditions identical to those of the standard Sod configuration. The flow is initially stagnant on both sides ($u_L = u_R = 0$), but the pressure and density on the left are modified to introduce stronger wave phenomena. Specifically:

- **Supersonic Case 1 (M ≈ 1.5):** $p_L = 5.0$, $\rho_L = 2.5$, $T_L = 0.00696$
- **Supersonic Case 2 (M ≈ 2.0):** $p_L = 20.0$, $\rho_L = 5.0$, $T_L = 0.01395$

Reflective (wall-type) boundary conditions were applied on both sides of the domain to mimic a closed shock tube configuration. Time integration was performed using the implicit second-order backward Euler method with a dynamically adjusted time step to maintain a maximum Courant number as specified in Table 4.2. The initial time step was set to 1×10^{-7} s, with a maximum allowable $\Delta t = 0.01$. Spatial discretization employed a combination of high-resolution and stabilized schemes:

- **Gradient terms:** `Gauss linear`
- **Divergence terms:** `limitedLinear` with limiter coefficient 1
- **Laplacian terms:** `Gauss linear corrected`
- **Interpolation:** `Linear`

The solver tolerances were chosen to be sufficiently strict to ensure accurate resolution of the discontinuities, with absolute tolerances set to 10^{-8}. These settings were applied uniformly to all solved variables.

Simulations for all three cases were performed using both `XiFoam` and `rhoCentralFoam`. This dual-solver strategy allows for a comparative evaluation of pressure-based and density-based solver performance under increasingly compressible conditions, with quantitative and qualitative assessment enabled by the test matrices from Tables 4.1–4.3.

4.4.3. Results

Mesh Independence Analysis

Three different mesh resolutions (M1, M2, and M3) were evaluated to assess the sensitivity of the simulation results to grid refinement. All cases correspond to the subsonic Sod shock tube configuration with a target Mach number of $M = 0.93$, and the results are shown in Figure 4.4.

Mesh Convergence Behavior: From Figure 4.4, it is evident that all three meshes capture the overall wave structure, including the rarefaction fan, contact discontinuity, and shock wave. However, discrepancies arise in the local resolution of these features:

- **Mesh M1 (300 cells)** exhibits visible numerical diffusion at the shock location and under-resolves the density jump across the contact surface. Additionally, velocity overshoots and slight pressure flattening are observed.
- **Mesh M2 (600 cells)** shows improved shock resolution and better agreement with the exact Riemann solution, particularly in the plateau and post-shock regions. This mesh captures discontinuities with acceptable sharpness while keeping spurious oscillations minimal.
- **Mesh M3 (1200 cells)** offers slightly better resolution of steep gradients and sharper transitions. However, the improvement over M2 is marginal and comes at twice the computational cost.

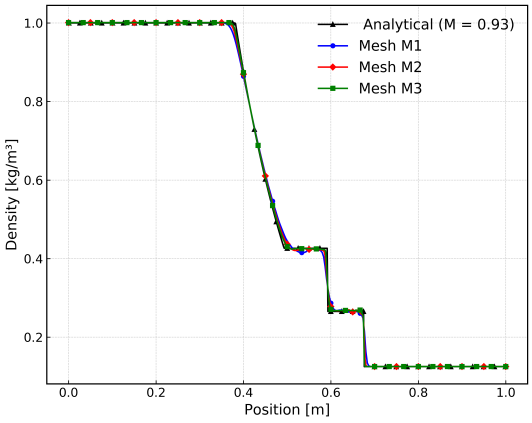

(a) Density vs Position at $\mathrm{t} = 0.1\,\mathrm{s}$

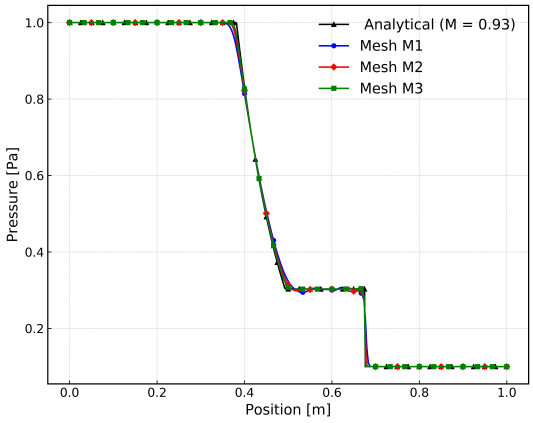

(b) Pressure vs Position at $\mathrm{t} = 0.1\,\mathrm{s}$

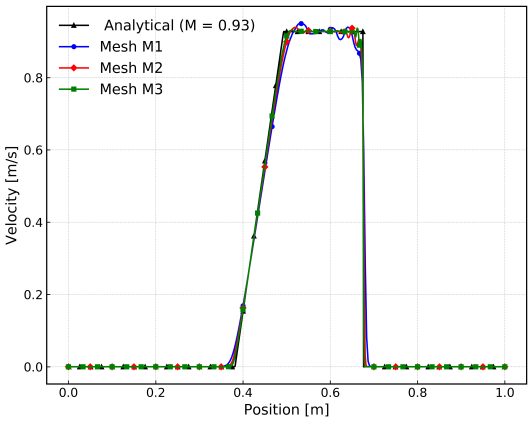

(c) Velocity vs Position at $\mathrm{t} = 0.1\,\mathrm{s}$

Figure 4.4: Mesh independence study for the subsonic Sod shock tube case ($M \approx 0.93$) using `XiFoam`. Results are shown for density, pressure, and velocity at $t = 0.1$ s for three different mesh resolutions (M1–M3).

To further illustrate this behavior, a zoomed-in view of the density field around the shock location is provided in Figure 4.5.

A closer inspection of Figure 4.5 reveals the following:

- **M1** shows significant numerical diffusion across the shock and contact discontinuity, leading to poor resolution of key flow features. The shock is noticeably smeared, and pre-shock gradients are poorly captured.
- **M3** delivers the most accurate representation of the density profile, with the sharpest resolution of the shock and minimal numerical diffusion.
- **M2**, while not as sharp as M3, performs considerably better than M1. It captures all key features of the solution with sufficient accuracy and stability, without introducing spurious oscillations. More importantly, it strikes a good balance between numerical fidelity and computational efficiency.

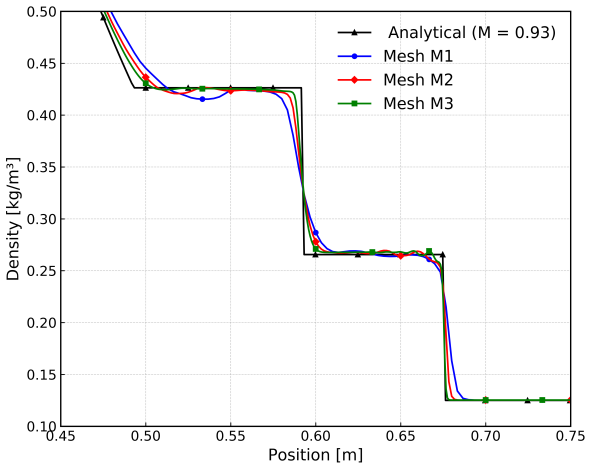

Figure 4.5: Zoomed-in density profile near the shock front for different mesh resolutions at $t = 0.1\,\text{s}$.

Although M3 technically offers the highest accuracy, mesh M2 was selected as the baseline for the remainder of this study. This choice is justified not only by the accuracy–cost tradeoff but also by the practical intent of examining how well pressure-based solvers behave on moderately coarse grids. Using extremely fine meshes may mask potential limitations or artifacts intrinsic to pressure-based formulations, especially in shock-dominated flows. Therefore, mesh M2 provides a more realistic basis for evaluating solver performance under conditions commonly encountered in engineering simulations.

These observations are particularly significant for pressure-based solvers like `XiFoam`, where accurate shock capturing is sensitive to grid resolution. Unlike density-based solvers that inherently propagate discontinuities through wave-speed based fluxes, pressure-based solvers require sufficient spatial resolution to resolve sharp gradients without inducing spurious pressure-velocity decoupling or excessive dissipation.

Final Mesh Selection: Based on this analysis, mesh M2 (600 cells) was selected as the baseline configuration for subsequent Courant number and Mach number sensitivity tests. From this point onward, only the density field will be shown in similar validation plots, as it exhibits the most prominent discontinuities and is the most sensitive metric for evaluating numerical artifacts. The trends observed in density extend similarly to pressure and velocity, thereby allowing for reduced visual clutter in result sections without compromising the rigor of analysis.

Courant Number Sensitivity Analysis

Having identified the optimal mesh resolution (M2) from the previous section, a Courant number sensitivity analysis was conducted to assess the influence of temporal resolution on solution accuracy. Four Courant numbers were tested: Co $= 0.05$, 0.1, 0.5, and 1.0, and the results are shown in Figure 4.6.

From Figure 4.6a, it is evident that all Courant numbers yield broadly similar global density profiles for the subsonic Sod shock tube case. However, closer inspection of the shock region in Figure 4.6b reveals important differences in local resolution and numerical behavior:

- Co $= 0.05$ produces the sharpest shock with minimal numerical diffusion and the closest agreement with the analytical solution. This can be attributed to the smaller time step and reduced temporal dissipation.
- Co $= 0.1$ also captures the shock well, with only a slight degradation in resolution compared to Co $= 0.05$. The difference between the two is marginal and does not significantly affect the overall accuracy of the result.
- For Co $= 0.5$ and Co $= 1.0$, the solution begins to exhibit small oscillations near the shock and contact discontinuity. These are likely the result of increased dispersion and reduced temporal resolution, which are particularly critical in pressure-based solvers.

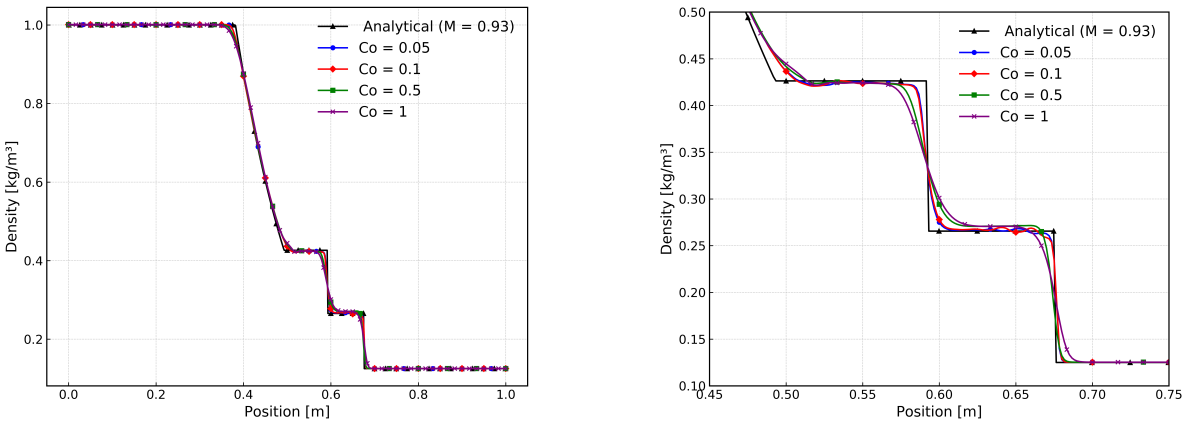

(a) Density vs Position at $\mathrm{t} = 0.1\,\mathrm{s}$

(b) Zoomed-in density profile near the shock front at $\mathrm{t} = 0.1\,\mathrm{s}$

Figure 4.6: Density profile for varying Courant numbers ($M = 0.93$), full domain view, and zoomed near the shock front

Although Co $= 0.05$ provides the most accurate representation of the shock, the incremental gain over Co $= 0.1$ is minimal. Therefore, in the interest of reducing computational cost, Co $= 0.1$ is selected as the optimal Courant number for the remainder of this study. This choice maintains a good trade-off between accuracy and efficiency, while remaining robust across both subsonic and supersonic flow regimes.

Mach Number Study

Having established an appropriate configuration from the mesh and Courant number sensitivity studies (i.e., Mesh M2 and Co $= 0.1$), the validated solver setup was used to simulate the Sod shock tube problem at three Mach numbers: $M = 0.93$, $M = 1.5$, and $M = 2.0$. These cases represent a progression from subsonic to supersonic regimes, and provide a basis for evaluating the capability of the pressure-based `XiFoam` solver in comparison with the density-based `rhoCentralFoam`. The simulation setup - including initial and boundary conditions, mesh resolution, and numerical schemes - was kept identical for both solvers to allow a direct and fair comparison.

Figures 4.7 to 4.9 present the results for each Mach number, including both a full-domain and a zoomed-in view near the shock region.

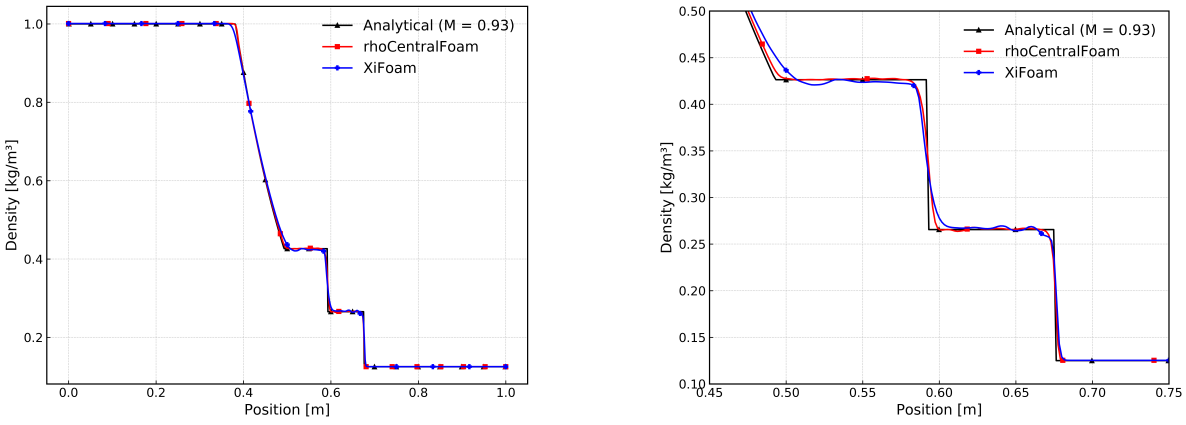

(a) Full domain view

(b) Zoomed-in view near shock

Figure 4.7: Comparison of Density profiles by `XiFoam` and `rhoCentralFoam` for the subsonic case ($M = 0.93$).

Observations:

- Across all Mach numbers, both solvers accurately resolve the essential features of the Sod shock tube problem - namely, the shock front, contact discontinuity, and rarefaction wave.
- For the subsonic case ($M = 0.93$)(refer figure 4.7), the agreement between `XiFoam`, `rhoCentralFoam`, and the analytical solution is nearly exact. The shock structure, expansion, and density jump are captured with high fidelity, and the difference between the solvers is minimal.
- At $M = 1.5$ (refer figure 4.8), both solvers continue to perform well. However, in the zoomed-in region, small-amplitude oscillations (or wiggles) are observed ahead of the density drop in the `XiFoam` solution. These are typical of pressure-based solvers and may result from the interplay between the gradient schemes or time stepping schemes under moderately strong shocks. Despite this, the shock location and overall wave structure remain physically consistent.
- At $M = 2.0$ (refer figure 4.9), the wiggles in `XiFoam` become slightly more pronounced, particularly just before the shock front. Meanwhile, `rhoCentralFoam` retains a slightly sharper shock resolution. This behavior is expected due to the inherently stronger shock-capturing nature of density-based solvers. Nevertheless, `XiFoam` continues to match the analytical solution well, and the amplitude of oscillations remains bounded and does not destabilize the solution.

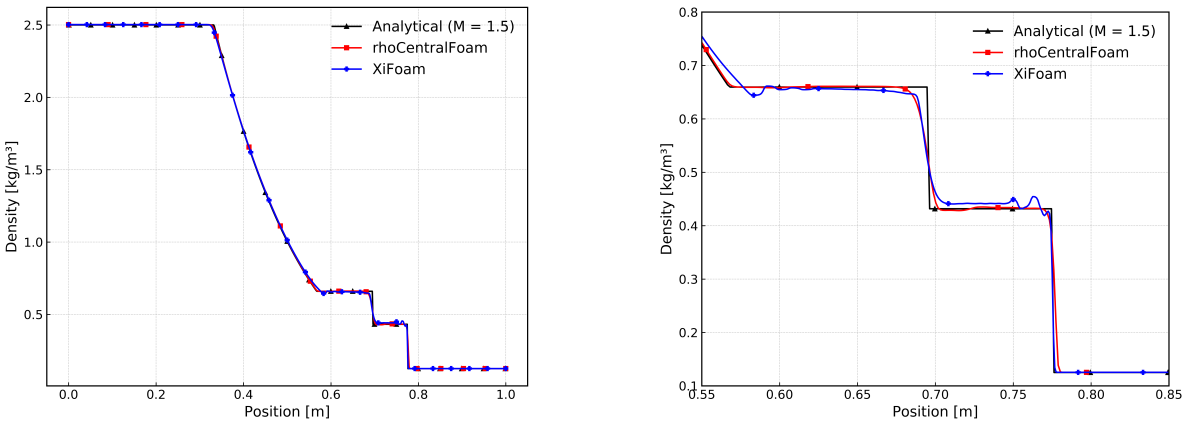

(a) Full domain view

(b) Zoomed-in view near shock

Figure 4.8: Comparison of Density profiles by `XiFoam` and `rhoCentralFoam` for the supersonic case ($M = 1.5$).

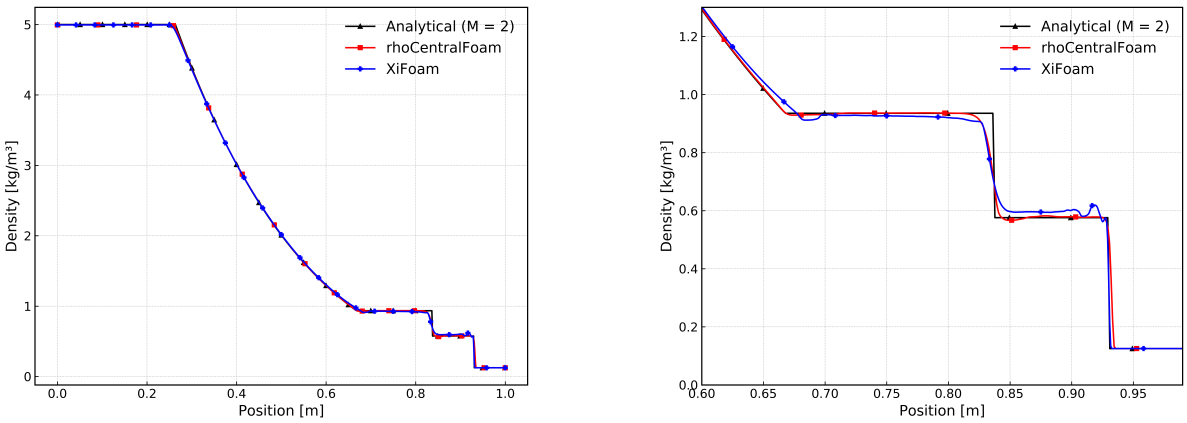

(a) Full domain view

(b) Zoomed-in view near shock

Figure 4.9: Comparison of Density profiles by `XiFoam` and `rhoCentralFoam` for the highly supersonic case ($M = 2.0$).

Influence of Numerical Schemes on Shock Resolution in Supersonic Flows

To further examine the role of numerical schemes in high-speed compressible flows, simulations were conducted using two different time integration schemes: first-order implicit Euler and second-order

implicit backward Euler. The test was performed for the strongest case considered ($M = 2.0$) to isolate the effect of time discretization in the presence of strong shocks and expansion waves.

Figure 4.10 shows a comparison of the predicted density profiles using the two schemes. At the full domain level, both methods capture the overall shock structure well, including the rarefaction wave, contact discontinuity, and shock front. However, the differences become more apparent in the zoomed-in view.

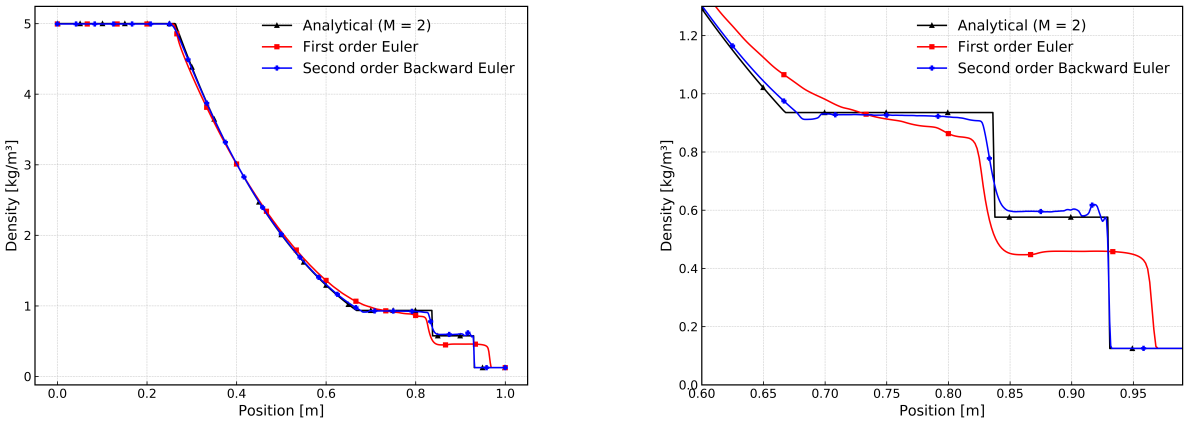

(a) Full domain density profile

(b) Zoomed-in view near the shock

Figure 4.10: Comparison of Density profiles by `XiFoam` with different time integration schemes at $M = 2.0$.

From Figure 4.10b, it is evident that the first-order Euler scheme produces a more diffused shock front, with smearing of the density discontinuity and loss of sharpness. This is consistent with the high numerical dissipation typically associated with low-order time discretization. On the other hand, the second-order backward Euler method yields a noticeably sharper shock profile that aligns more closely with the analytical solution. The improved temporal accuracy translates directly to better resolution of steep gradients.

These observations reinforce the need for higher-order time schemes in shock-dominated flows, especially when using pressure-based solvers that are already susceptible to dissipation due to spatial interpolation errors.

General Implication on Numerical Scheme Selection:
In addition to the time integration method, other discretization schemes - such as those for gradient, divergence, interpolation, and Laplacian terms -play a critical role in determining solver accuracy and robustness. In this study, consistent and shock-aware schemes were selected for the Sod shock tube problem, and they were shown to perform well across a range of Mach numbers. Therefore, to ensure consistency and reliability, the same suite of numerical schemes will be adopted in the main hydrogen combustion simulations.

These results demonstrate that `XiFoam`, with appropriate numerical configuration, is capable of simulating weak and moderate strength shocks with high fidelity. Although minor differences appear in the supersonic regime due to the inherent differences between pressure-based and density-based solvers, the overall performance of `XiFoam` is robust and suitable for compressible flow applications involving deflagration or shock wave propagation.

Having established the solver's accuracy in handling shock dominated flows, we now turn our attention to the next key components for turbulent combustion modelling: the calculation of flame radius. The next section outlines the methods implemented for tracking flame propagation, which form the basis for evaluating flame front velocities in later validation and application cases.

4.5. Flame Radius Calculation Methods

An important quantity extracted from both experiments and numerical simulations is the flame radius, which provides insight into the spatial propagation of the flame front. In OpenFOAM, three different approaches have been implemented to compute this flame radius during runtime, depending on the dimensionality of the problem and the level of flame distortion. In this work, the configurations considered involve flame propagation predominantly along a specific axis; therefore, only the method applicable to such cases is described here.

Axial-Based Method (axialBased) This method is particularly useful in configurations where the flame front does not exhibit spherical symmetry. The flame radius is computed along a specified axis direction $\vec{n}_r$, by identifying the maximum coordinate in that direction for cells satisfying the isosurface bounds. The radius is then computed as:

$$R_f = \|\vec{x}_i - \vec{x}_{\mathsf{ign}}\| \tag{4.16}$$

where

$$\vec{x}_i = \begin{cases} \tilde{f}_{\mathsf{low}} < \tilde{f}(\vec{x}_i) < \tilde{f}_{\mathsf{up}} \\ \max\left(\vec{x}_i \cdot \vec{n}_r\right) \end{cases}$$

This approach directly measures the flame front distance along $\vec{n}_r$, making it suitable for flames propagating predominantly in a single direction.

In all simulations presented in this thesis, the `axialBased` method is used to calculate the flame radius. Now, the next section outlines the methods implemented for calculating the laminar flame speed of hydrogen-air mixtures, which form the basis for evaluating turbulent flame speeds during combustion, that is enhanced by wrinkling.

4.6. Laminar Flame Speed Models

The source term $\widetilde{\dot{\omega}_c}$ introduced in Equation 4.15 depends on the laminar flame speed S_L, which plays a critical role in determining flame propagation in reactive flow simulations. It is important to remember that the laminar flame speed correlations provided by the experiments is always the Unstrained Laminar Flame Speed , denoted as $S_{L,0}$ .OpenFOAM provides multiple correlations for evaluating $S_{L,0}$, depending on the type of fuel and desired accuracy. These include:

Constant Flame Speed Model This simplest approach assumes a constant laminar flame speed throughout the domain. Here, the initial laminar flame speed is provided as an input (calculated using Cantera [70]) and its held constant throughout the simulation.

$$S_{L,0} = \text{constant.} \tag{4.17}$$

Gülder Correlation [71] Originally developed for hydrocarbon fuels such as methane and propane, the Gülder model expresses $S_{L,0}$ as a function of equivalence ratio ϕ, unburned gas temperature T_u, unburned gas pressure p_u, and the mole fraction of diluent species X_{D}:

$$S_{L,0} = \left[a_4\phi^{a_5} - \exp^{-a_3(\phi-1.075)^2}\right]\left(\frac{T_u}{T_{\mathrm{ref}}}\right)^{a_1}\left(\frac{p_u}{p_{\mathrm{ref}}}\right)^{a_2}(1 - X_{\mathrm{D}}a_3)\,. \tag{4.18}$$

Ravi-Petersen Correlation [72] An alternative empirical model also developed for hydrocarbon fuels, the Ravi-Petersen formulation is given by:

$$S_{L,0} = \left[b_1 + b_2\phi + b_3\phi^2 + b_4\phi^3 + b_5\phi^4\right]\left(\frac{T_u}{T_{\mathrm{ref}}}\right)^{b_6+b_7\phi+b_8\phi^2+b_9\phi^3}. \tag{4.19}$$

The Gülder and Ravi-Petersen correlations, while widely used for methane-air and propane-air flames, are not rigorously validated for hydrogen-air combustion, particularly in very lean mixtures. These formulations exhibit similar behavior for hydrogen equivalence ratios between 0.3 and 0.5, but deviate significantly at lower concentrations. Notably, the Ravi-Petersen model tends toward unphysical flame speeds below equivalence ratios of $\phi < 0.1$. For more details, refer to the thesis of De-Palma [31].

Since these existing correlations fail to accurately predict flame speeds in lean hydrogen mixtures, new correlations based on the experimental data of Bentaib and Chaumeix [34] have been implemented in `OpenFOAM`. This is served as an input to the source term $\widetilde{\dot{\omega}_c}$ in equation 4.15. The details of this new implementation are presented in the next section.

4.6.1. New Laminar flame speed correlations for non uniform hydrogen−air mixtures

To improve the accuracy of laminar flame speed predictions in non-uniform mixtures, a probability density function (PDF)-based approach has been implemented. This method accounts for sub-grid scale variability in the mixture fraction fields, enabling the calculation of an effective laminar flame speed that reflects local compositional fluctuations. Such an approach is particularly important for partially premixed or stratified flames, where the interaction between turbulence and chemistry plays a significant role.

This methodology has been implemented in `OpenFOAM` as a generic flame speed library. A central contribution of the present work is the optimisation of this implementation and its validation for lean, stratified hydrogen-air mixtures.

Liu and MacFarlane [73] measured the laminar flame speed of hydrogen-air-diluent (generally steam) mixtures in a bunsen burner. The experiment covers hydrogen concentrations in the range of 18–65 vol.%, steam concentrations in the range of 0–15 vol.%, a temperature range of 296–523 K, and pressure of 1 atm. They fitted their experiments into an empirical formula as follows:

$$S_{L,0}^{\mathsf{LMF}} = BT_u^C \exp(DX_d) \tag{4.20}$$

where T_u is the local unburnt temperature and the coefficients B, C and D depend on the mixture content of hydrogen, X_d is the mole fraction of the diluent. X_d can be related to the diluent mixture fraction Z_d by :

$$X_d = \frac{W_d}{\overline{W}} Y_d = \frac{W_d}{\overline{W}} \cdot \frac{\widetilde{Z}_d}{1 - \widetilde{Z}} \tag{4.21}$$

where Y_d is the diluent mass fraction, W_d is the diluent molecular weight and $\overline{W}$ is the mixture mean molecular weight. The constants B,C and D in 4.20 are given by :

$$\begin{aligned} B &= A_1 + A_2(0.42 - x_{H_2}) + A_3(0.42 - x_{H_2})^2 \\ C &= A_4 + A_5(0.42 - x_{H_2}) \\ D &= A_6 \end{aligned}$$

The values of the constant A1, A2... A6 are summarized in the Table 4.4

Table 4.4: Values of constants used in the correlations for B, C, and D_1 based on x_{H_2}.

	$x_{H_2} \leq 0.42$	$x_{H_2} \geq 0.42$
A_1	4.644×10^{-4}	4.644×10^{-4}
A_2	-2.119×10^{-3}	9.898×10^{-4}
A_3	2.344×10^{-3}	-1.264×10^{-3}
A_4	1.571	1.571
A_5	0.3839	-0.2476
A_6	-2.21	-2.24

where x_{H_2} is the vol % of hydrogen. This can be calculated using the mixture fraction and the equivalence ratio in a straightforward manner. The equivalence ratio can be calculated from Z using equation 2.5, where Z_{st} for a hydrogen air mixture is 0.028. From ϕ, the hydrogen mixture content is computed for a mixture with air as:

$$x_{H_2} = \frac{2\Phi}{2\Phi + 4.77} \tag{4.22}$$

A newer correlation for lean hydrogen mixtures was suggested by Bentaib and Chaumeix [34]:

$$S^B_{L,0} = \left(1.44\Phi^2 + 1.07\Phi - 0.29\right)(1 - X_d)^4 \tag{4.23}$$

The Bentaib correlations can be used to obtain laminar flame speeds for mixtures with hydrogen concentrations less than 18 %, which is outside the limit of the experiments Liu and Macfarlane performed. However, the use of both is required as the Bentaib correlations is unbounded for high values of the equivalence ratio, returning infinite velocities. Hence, the minimum operator is used, computing the reference laminar flame speed as (see figure 4.11):

$$S^{\text{ref}}_{L,0} = min(S^B_{L,0}, S^{\text{LMF}}_{L,0}) \tag{4.24}$$

Next, if the flame propagates in a closed vessel, the unburned gas ahead of the flame is compressed. This accounts to an increase in temperature and pressure that is modelled by:

$$S^{\text{corr}}_{L,0} = S^{\text{ref}}_{L,0} \times C \tag{4.25}$$

where C can be calculated in two ways:

$$C = \left(\frac{\widetilde{p}}{p_{\text{ref}}}\right)^m \left(\frac{\widetilde{T}_u}{T_{\text{ref}}}\right)^n \tag{4.26}$$

where m and n are pressure and temperature coefficients, or by using an overall thermokinetic index ϵ:

$$C = \left(\frac{\widetilde{p}_i}{p_{\text{ref}}}\right)^\epsilon \tag{4.27}$$

where p_{ref} is 101325 Pa, and T_{ref} is 298 K. The exponents m and n can be obtained by polynomial fittings from the data provided in [74] and [75]. Usually, for lean hydrogen air mixtures with steam as a diluent, m and n can be approximated as -0.5 and 2.2, respectively. The overall kinetic index can be calculated using the following expression [76]:

$$\epsilon = 1.122417x^3_{H_2} + 0.536407x^2_{H_2} - 1.260739x_{H_2} + 0.852327 \tag{4.28}$$

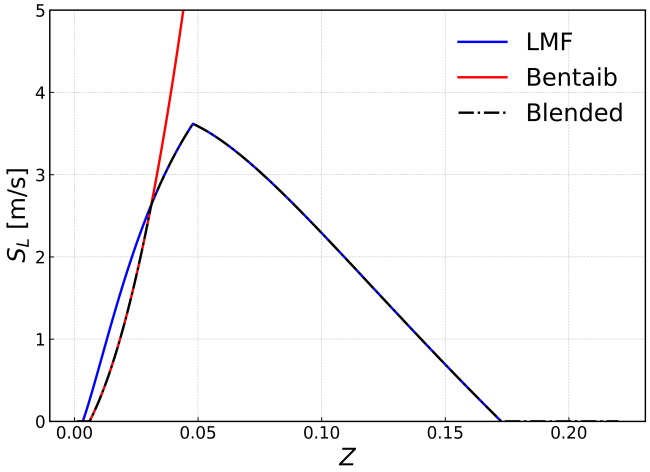

Figure 4.11: Variation of laminar flame Speed with mixture fraction

These polynomial fittings were obtained by performing regression of different order polynomials to the data originally provided in [76]. However, for lean hydrogen air mixtures (< 15 %), the values of ϵ are not available and hence, they are obtained by extrapolation.

Based on the corrected value of the laminar flame speed $S_{L,0}^{\text{corr}}$, the final laminar flame speed $\widetilde{S_{L,0}}$ for each cell can be computed in three different ways depending on the mixture fraction values of the mixture and the diluent of the cell, as shown in figure 4.12.

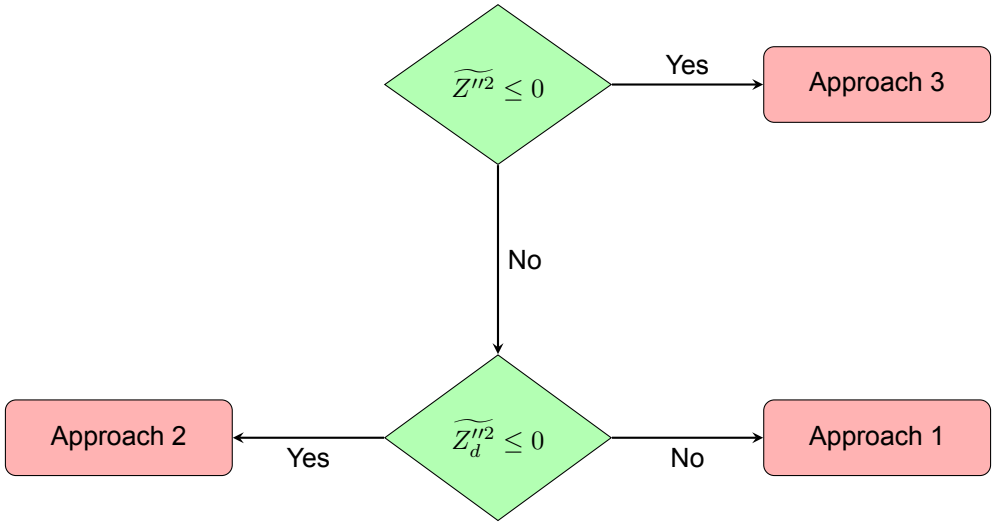

Figure 4.12: Decision logic for selecting the laminar flame speed calculation approach based on mixture fraction variance $\widetilde{Z''^2}$ and diluent mixture fraction variance $\widetilde{Z_d''^2}$.

In Figure 4.12, Approach 3 is coded as:

$$\widetilde{S}_{L,0}(\vec{x},t) = S_{L,0}^{\text{corr}}\left(\widetilde{Z}(\vec{x},t), \widetilde{Z}_d(\vec{x},t)\right) \tag{4.29}$$

Upon closer look, it can be seen that this is equivalent to the blended correlations to which temperature and pressure corrections have been applied.

Approach 2 in Figure 4.12 is implemented for a non-zero variance $\widetilde{Z''^2}$ in the fuel mixture stream and a zero variance in the diluent stream $\widetilde{Z_d''^2} = 0$. It is coded as:

$$\widetilde{S}_{L,0}(\vec{x},t) = \int_0^1 S_{L,0}^{\text{corr}}\left(\zeta, \widetilde{Z}_d(\vec{x},t)\right) \mathbb{P}\left(\widetilde{Z}(\vec{x},t), \widetilde{Z''^2}(\vec{x},t), \zeta\right) d\zeta \tag{4.30}$$

where $\mathbb{P}$ is the mass weighted probability density function (PDF) of the mixture fraction fraction ($\tilde{Z}$) field. As mentioned earlier, a beta PDF model is used to construct the PDF. The beta distribution is defined as [54]:

$$\mathbb{P}(a,b,\zeta) = \frac{\Gamma(a+b)}{\Gamma(a)\Gamma(b)}\zeta^{a-1}(1-\zeta)^{b-1} \tag{4.31}$$

where the parameters a(> 0) and b(> 0) can be computed as:

$$a = \widetilde{Z}\left[\frac{\widetilde{Z}(1-\widetilde{Z})}{\widetilde{Z''^2}} - 1\right] \qquad \text{and} \qquad b = \frac{a}{\widetilde{Z}} - a \tag{4.32}$$

This choice is done so that the mean of the beta distribution is exactly $\widetilde{Z}$ and the variance is $\widetilde{Z''^2}$. It can be seen that the beta PDF can be rewritten as previously done in terms of its mean and variance with 4.33 as:

$$\mathbb{P}(a,b,\zeta) = \mathbb{P}(\widetilde{Z}, \widetilde{Z''^2}, \zeta) \tag{4.33}$$

It can be seen that the beta distribution depends on the gamma function $\Gamma(x)$ which is commonly used as a continuation of the factorial to the complex numbers. It is formally defined as:

$$\Gamma(x) = \int_0^\infty \theta^{x-1} e^{-\theta}\, d\theta \tag{4.34}$$

In this consideration, only the real part of the complex number is taken. There is not a closed expression to evaluate the gamma function. Thus, different approximations have been proposed throughout the years. The Lanczos approximation [77] has a simple implementation yet it is accurate for the range of interest. Once the beta PDF is evaluated, numerical integration is required to compute the integral in equation 4.30.

Approach 1 in Figure 4.12is implemented for a non-zero variance in the fuel mixture stream and a non zero variance in the diluent stream. It is coded as a double integral :

$$\widetilde{S}_{L,0}(\vec{x},t) = \int_0^1 \int_0^1 S_{L,0}^{\mathsf{corr}}(\zeta,\zeta_d)\, \mathbb{P}\left(\widetilde{Z}(\vec{x},t), \widetilde{Z''^2}(\vec{x},t), \zeta\right) \mathbb{P}_d\left(\widetilde{Z}_d(\vec{x},t), \widetilde{Z_d''^2}(\vec{x},t), \zeta_d\right) d\zeta\, d\zeta_d \tag{16}$$

where $\mathbb{P}$ and $\mathbb{P}_d$ are mass-weighted PDF's of the mixture fraction $\widetilde{Z}$ and diluent mixture fraction $\widetilde{Z_d}$, respectively.

This work deals only with gradients in the $\widetilde{Z}$ field. Thus, approach 2 will be considered for all the test cases. Henceforth, this implementation will be referred to as the *Bentaib flame speed library*. During each simulation time step, the library first computes the base laminar flame speed from the mean mixture fraction $\widetilde{Z}$, applies the corresponding pressure and temperature corrections in every computational cell. Based on the variance calculated through a transport equation(refer section 4.7.2), the integrated flame speed is then obtained through the appropriate PDF-based formulation, and the resulting value is used as the laminar input to the turbulent flame speed model for all cells in the domain.

4.6.2. Laminar Flame Speed Corrections

Once the unstrained laminar flame speed $S_{L,0}$ has been computed as described in the previous section, it is necessary to account for the effects of flow strain and curvature to obtain the actual strained laminar flame speed S_L. OpenFOAM provides three models for this correction, each offering a different level of complexity and fidelity.

Unstrained Model (SuModel unstrained) This model assumes that the laminar flame speed is unaffected by strain and curvature, and simply sets:

$$S_L = S_{L,0}. \tag{4.35}$$

This is the simplest model and is primarily used in scenarios where strain effects are negligible.

Equilibrium Model (SuModel equilibrium) Here, strain effects are incorporated by computing the resolved strain rate σ_{rs}. The strained laminar flame speed is then given as:

$$S_L = S_L^\infty = S_{L,0} \max\left(1 - \frac{\sigma_{rs}}{\sigma_{\mathsf{ext}}}, 0.01\right), \tag{4.36}$$

where σ_{ext} is a user-defined extinction strain rate, and σ_{rs} is calculated as:

$$\sigma_{rs} = \left[n_i n_i \frac{\partial u_j}{\partial x_j} - n_i \frac{\partial u_j}{\partial x_i} n_j\right] \frac{1}{\Xi} + \left[n_i n_i \frac{\partial S_L n_j}{\partial x_j} - n_i \frac{\partial S_L n_j}{\partial x_i} n_j\right] \frac{\Xi + 1}{2\Xi}, \tag{4.37}$$

with the flame normal vector $\vec{n}$ computed as:

$$\vec{n} = \frac{\nabla \tilde{b}}{\left\|\nabla \tilde{b}\right\|}. \tag{4.38}$$

This approach assumes a local equilibrium between strain effects and flame propagation.

Transport Model (SuModel transport [78, 67]) The most advanced option involves solving a transport equation for S_L directly, considering the effects of strain and curvature dynamically:

$$\frac{\partial(\rho S_L)}{\partial t} + \frac{\partial}{\partial x_i}\left[(\rho u_i + \phi_\Xi) S_L\right] - S_L \frac{\partial}{\partial x_i}(\phi_\Xi) = -S_L \left(-\rho R_c \frac{S_{L,0}}{S_L}\right) - S_L \left[\rho\left(\sigma_s + R_c\right)\right] \tag{4.39}$$

where ϕ_Ξ is the flux term defined as:

$$\phi_\Xi = \tilde{\rho}_u S_{t,\text{corr}} S_L \Xi \left(S_{f,i} \cdot n_{f,i}\right) - \left[\frac{1}{|\partial \tilde{b}/\partial x_i|} \cdot \frac{\partial}{\partial x_i}\left(\alpha_{\text{eff}} \frac{\partial \tilde{b}}{\partial x_i}\right)\right] \left(S_{f,i} \cdot n_{f,i}\right) + \rho \left[S_L \left(\frac{1}{\Xi} - \Xi\right)\right] \left(S_{f,i} \cdot n_{f,i}\right) \tag{4.40}$$

and R_c is a coefficient accounting for extinction effects:

$$R_c = \frac{\sigma_s S_L^\infty (S_{L,0} - S_L^\infty) + (0.01 \mu_{S_L})^2 \sigma_{\text{ext}}}{(S_{L,0} - S_L^\infty)^2 + (0.01 \mu_{S_L})^2} \tag{4.41}$$

This model provides higher accuracy in cases where flame response to strain is critical but incurs additional computational cost due to the need to solve an extra transport equation.

Among these models, the **transport model** provides the most detailed representation of strain effects and is theoretically the most accurate for strain-sensitive flows. However, in this thesis, the **unstrained model** is employed for all simulations. This choice is further supported by the findings of Lobato Pérez [30], who, through a series of numerical simulations conducted for the ENACCEF(see section 5.2) and ENACCEF-2(see section 5.1) facilities that are investigated in this work, demonstrated that the influence of compression and strain on the laminar flame speed was not pronounced for the configurations considered.

Having now described the flame radius calculation method, the laminar flame speed correlations, and the associated corrections, the only remaining component required to close the chemical source term $\widetilde{\dot{\omega}_c}$ is the wrinkling factor Ξ. In the following section, we present the new solvers developed and employed in this work, along with the updated correlations for the wrinkling factor Ξ.

4.7. NRGXiFoam and ppNRGXiFoam

To address the limitations observed in `XiFoam`, two new solvers were developed and employed in this thesis: `NRGXiFoam` and `ppNRGXiFoam`. These solvers were specifically designed to improve the treatment of turbulent flame propagation, particularly in lean hydrogen mixtures and partially premixed environments, by incorporating updated algebraic correlations for Ξ and extended modeling capabilities.

The need for these new solvers arose from the constraints of `XiFoam`, which lacked the ability to use robust laminar flame speed formulations suitable for hydrogen–air systems in lean combustion regimes and could not handle fuel concentration gradients essential for partially premixed combustion. Both solvers retain a structure similar to `XiFoam`, with additional intermediate steps and enhanced algorithms implemented in their source codes.

4.7.1. `NRGXiFoam`

The `NRGXiFoam` solver is designed for fully premixed combustion cases. It implements updated algebraic wrinkling factor models, including the Turbulent Flame Speed Closure (TFC) and Extended Turbulent Flame Speed Closure (ETFC) formulations described in Chapter 3. These correlations provide a more accurate representation of flame wrinkling and turbulent flame propagation in fully premixed flows.

In terms of implementation, the new Ξ correlations are introduced directly within `bEqn.H`, which governs the solution of the regress variable transport equation (see Figure 4.1). The solver architecture ensures that, during the sequential solution of the relevant transport equations, the wrinkling factor is evaluated at the appropriate stage in the algorithm. The selection of the desired Ξ model is made through the `CombustionProperties` dictionary in the `constant` directory, allowing the user to switch between different wrinkling factor formulations without modifying the solver code. In this way, the flame wrinkling

factor is consistently obtained within the main loop, feeding directly into the calculation of the mean chemical source term.

4.7.2. ppNRGXiFoam

The ppNRGXiFoam solver extends the capabilities of NRGXiFoam to account for partially premixed combustion, with explicit treatment of mixture fraction fields and their variances. This allows the solver to handle fuel stratification and scalar inhomogeneities in a physically consistent manner. In addition to solving the regress variable transport equation (see Figure 4.1), the solver computes the transport of the fuel mixture fraction $\widetilde{Z}$, its variance $\widetilde{Z''^2}$, the diluent mixture fraction $\widetilde{Z_d}$, and its variance $\widetilde{Z_d''^2}$.

The transport equation for the mean fuel mixture fraction $\widetilde{Z}$ is:

$$\frac{\partial}{\partial t}\left(\bar{\rho}\widetilde{Z}\right) + \frac{\partial}{\partial x_i}\left(\bar{\rho}\widetilde{u}_i\widetilde{Z}\right) - \frac{\partial}{\partial x_i}\left(\bar{\rho}D_{\mathrm{eff},t}\frac{\partial\widetilde{Z}}{\partial x_i}\right) = 0, \tag{4.42}$$

where $D_{\mathrm{eff},t}$ is the sum of laminar and turbulent diffusivities. The variance $\widetilde{Z''^2}$ is solved via:

$$\frac{\partial}{\partial t}\left(\bar{\rho}\widetilde{Z''^2}\right) + \frac{\partial}{\partial x_i}\left(\bar{\rho}\widetilde{u}_i\widetilde{Z''^2}\right) - \frac{\partial}{\partial x_i}\left(\bar{\rho}D_{\mathrm{eff},t}\frac{\partial\widetilde{Z''^2}}{\partial x_i}\right) = 2\bar{\rho}D_t\frac{\partial\widetilde{Z}}{\partial x_i}\frac{\partial\widetilde{Z}}{\partial x_i} - C_\chi\bar{\rho}\frac{\varepsilon}{k}\widetilde{Z''^2}, \tag{4.43}$$

where D_t is the turbulent diffusivity, and C_χ is the variance dissipation coefficient.

Similarly, for the diluent mixture fraction $\widetilde{Z_d}$, the governing equation is:

$$\frac{\partial}{\partial t}\left(\bar{\rho}\widetilde{Z_d}\right) + \frac{\partial}{\partial x_i}\left(\bar{\rho}\widetilde{u}_i\widetilde{Z_d}\right) - \frac{\partial}{\partial x_i}\left(\bar{\rho}D_d\frac{\partial\widetilde{Z_d}}{\partial x_i}\right) = 0, \tag{4.44}$$

and its variance $\widetilde{Z_d''^2}$ is given by:

$$\frac{\partial}{\partial t}\left(\bar{\rho}\widetilde{Z_d''^2}\right) + \frac{\partial}{\partial x_i}\left(\bar{\rho}\widetilde{u}_i\widetilde{Z_d''^2}\right) - \frac{\partial}{\partial x_i}\left(\bar{\rho}D_d\frac{\partial\widetilde{Z_d''^2}}{\partial x_i}\right) = 2\bar{\rho}D_{dt}\frac{\partial\widetilde{Z_d}}{\partial x_i}\frac{\partial\widetilde{Z_d}}{\partial x_i} - C_\chi\bar{\rho}\frac{\varepsilon}{k}\widetilde{Z_d''^2}, \tag{4.45}$$

where D_d is the effective diffusivity for the diluent mixture fraction:

$$D_d = D_{\mathrm{dil}} + D_{dt} = D_{\mathrm{dil}} + 0.09\frac{k^2}{\varepsilon}\frac{\alpha_{\mathrm{dil}}}{\nu_{\mathrm{dil}}}. \tag{4.46}$$

These equations are implemented in ppNRGXiFoam and are solved in the same step as the regress variable (bEqn.H) in OpenFOAM, ensuring consistent coupling with the regress variable evolution, necessary for the laminar flame speed and the chemical source term. Solver modes allow the user to control whether the variance equations are solved. For example, the evolution of variance $\widetilde{Z''^2}$ is only computed if solveZp is set to true, and $\widetilde{Z_d''^2}$ is only computed if solveZd is enabled. As seen in Figure 4.12, Approach 3 is taken when both solveZp and solveZd are set to False. Approach 2 is taken when solveZp is set as true and solveZd is set to False. Approach 1 is taken when both solveZp and solveZd are set to true. However, the solver does not allow solving for $\widetilde{Z_d}$ without also solving for its variance $\widetilde{Z_d''^2}$; all other combinations are possible.

The computed $\widetilde{Z}$, $\widetilde{Z_d}$, and their variances are passed directly to the Bentaib laminar flame speed library at each time step. The library uses these quantities to calculate the effective laminar flame speed for every computational cell by integrating over the beta-distribution of the mixture fraction (and diluent fraction when relevant), applying the temperature and pressure corrections before passing the result to the turbulent flame speed closure. Essentially, two modes of usage are possible when initializing the mixture fraction variance. A non-zero initial value of $\widetilde{Z''^2}$ can be prescribed while setting solveZp = false. In this case, $\widetilde{Z''^2}$ is retained as a non-evolving field, but it is still employed at every time step in the computation of the effective integrated laminar flame speed. In the second case, if solveZp = true, then the variance equation will be solved for every time step, and then fed to the computation of the effective integrated laminar flame speed.

4.7.3. Flame Wrinkling Models in `XiFoam` and New Solver Extensions

The flame wrinkling factor Ξ plays a critical role in turbulent premixed combustion modeling by accounting for the increase in flame surface area due to turbulence. In `XiFoam`, several models are implemented to compute Ξ, ranging from simple fixed coefficients to more advanced transport equations. Additionally, in this work, new models have been developed and incorporated into the `NRGXiFoam` and `ppNRGXiFoam` solvers to improve the prediction of flame wrinkling in premixed and partially premixed flows.

Existing Models in `XiFoam`

- **Fixed (`XiModel fixed`):** The wrinkling factor Ξ is kept constant during the simulation and initialized from user-specified values. This is primarily useful for debugging or laminar flame calculations where $\Xi = 1$.
- **Algebraic (`XiModel algebraic`[79]):** This model uses an empirical correlation derived from turbulent flame speed scaling laws. The wrinkling factor is calculated as:

$$\Xi = 1 + (1 + 2\Xi_{sc}(0.5 - b))\,\Xi_c \left(\sqrt{\frac{u'}{S_L + 0.01\mu_{S_L}}}\right) \mathrm{Re}_\eta, \tag{4.47}$$

  where $\mathrm{Re}_\eta = u'/\sqrt{\epsilon\tau_\eta}$ is the Kolmogorov-scale Reynolds number, $\Xi_c = 0.62$ is the wrinkling factor coefficient, and $\Xi_{sc} = 1$ is a shape coefficient. This formulation has shown good agreement with experimental and spectral results.
- **Transport (`XiModel transport` [78]):** In this model, Ξ is computed by solving a transport equation that includes production and destruction terms:

$$\frac{\partial}{\partial t}(\rho\Xi) + \frac{\partial}{\partial x_i}\left[(\rho u_i + \phi_\Xi)\, S_L\right] - \Xi\frac{\partial}{\partial x_i}\left(\phi_\Xi\right) = \rho R' - \Xi\rho\left(R' - G'\right) - \Xi\rho\max\left(\sigma_t - \sigma_s, 0\right), \tag{4.48}$$

  where τ_η is the Kolmogorov timescale and the model coefficients are defined as:

$$\begin{aligned} G^* &= \frac{0.28}{\tau_\eta}, \\ R' &= \frac{G^*\Xi^*_{eq}}{\Xi^*_{eq} - 1}, \\ G' &= \frac{R'\left(\Xi_{eq} - 1.001\right)}{\Xi_{eq}}. \end{aligned}$$

  Different equilibrium flame wrinkling factors are used:

$$\begin{aligned} \Xi^*_{eq} &= 1.001 + \Xi_c \left(\sqrt{\frac{u'}{S_L + 0.01\mu_{S_L}}}\right) \mathrm{Re}_\eta, \\ \Xi_{eq} &= 1.001 + \left[1 + 2\Xi_{sc}(0.5 - \min[\max(b, 0), 1])\right](\Xi^*_{eq} - 1.001). \end{aligned}$$

While the algebraic model is computationally inexpensive, the transport model is more physically consistent as it also includes strain effects on the flame. However, the transport equation is computationally more demanding.

New Models in `NRGXiFoam` and `ppNRGXiFoam`

Two new flame wrinkling models have been implemented in these solvers:

- **Zimont-TFC [63]:**

$$\Xi = A\frac{u'}{S_L}\left(\frac{\tau_t}{\tau_c}\right)^{0.25} \tag{4.49}$$

  where A is Zimont's constant (typically $A \in [0.42, 0.50]$), τ_t is the turbulent time scale, and $\tau_c = D/S_L^2$ is the chemical time scale.

- **Lipatnikov-ETFC [53]:**

$$\Xi = A\frac{u'}{S_L}\left(\frac{\tau_t}{\tau_c}\right)^{0.25}\left[1+\frac{\tau_L}{t}\exp\left(-\frac{t}{\tau_L}\right)\right]^{0.5} \tag{4.50}$$

where τ_L is the Lagrangian timescale and is calculated as:

$$\tau_L = \frac{1}{u'^2}\frac{C_\mu}{\mathrm{Pr}_t}\frac{k}{\epsilon}.$$

The implementation of these correlations enables improved predictions for turbulent flame propagation, especially in lean hydrogen-air mixtures where conventional models tend to underperform.

In all simulations presented in this thesis, the **Zimont-TFC model** is adopted for its balance of accuracy and computational efficiency.

With the development of `NRGXiFoam` and `ppNRGXiFoam`, the different strategies for evaluating the wrinkling factor Ξ and the laminar flame speed S_L have now been described in detail. These modelling components form the essential elements required to close the mean chemical source term in the turbulent combustion equations. Having established the procedures for flame wrinkling and laminar flame speed evaluation, the discussion now turns to the modelling of thermodynamic and transport properties, which are equally critical for accurately representing turbulent premixed and partially premixed combustion.

4.8. Thermodynamic Properties Calculation

The accurate calculation of thermodynamic and transport properties is critical for modeling reacting flows. In OpenFOAM, these properties are computed at runtime based on the mixture composition and local thermodynamic state, allowing for a consistent coupling with the combustion and turbulence models.

The solver starts from initial temperature and regress variable (b) fields, from which the enthalpy values are computed using mixture-specific coefficients. These enthalpy fields account for both the sensible enthalpy and the enthalpy of formation at a standard reference state, ensuring that heat release from chemical reactions is already embedded in the formulation. After initialization, the transport equations for enthalpy are solved at each time step, and the resulting enthalpy field is inverted to obtain the temperature field using the regress variable field.

Two transport equations are used in `XiFoam`: the mixture enthalpy equation and the unburnt enthalpy equation. The former is given by:

$$\frac{\partial}{\partial t}(\tilde{\rho}\tilde{h}) + \frac{\partial}{\partial x_k}(\tilde{\rho}\tilde{u}_k\tilde{h}) + \frac{\partial}{\partial t}(\tilde{\rho}\tilde{K}) + \frac{\partial}{\partial x_k}(\tilde{\rho}\tilde{u}_k\tilde{K}) = \frac{\partial p}{\partial t} + \frac{\partial}{\partial x_k}\left(\tilde{\rho}D_{\mathsf{eff}}\frac{\partial\tilde{h}}{\partial x_k}\right), \tag{4.51}$$

where $\tilde{K} = |\tilde{\mathbf{u}}|^2/2$ is the specific kinetic energy. Similarly, the unburnt enthalpy equation is expressed as:

$$\frac{\partial}{\partial t}(\tilde{\rho}\tilde{h}_u) + \frac{\partial}{\partial x_k}(\tilde{\rho}\tilde{u}_k\tilde{h}_u) + \frac{\partial}{\partial t}(\tilde{\rho}\tilde{K}) + \frac{\partial}{\partial x_k}(\tilde{\rho}\tilde{u}_k\tilde{K}) - \frac{\partial p}{\partial t}\frac{\tilde{\rho}}{\rho_u} = \frac{\partial}{\partial x_k}\left(\tilde{\rho}D_{\mathsf{eff}}\frac{\partial\tilde{h}_u}{\partial x_k}\right), \tag{4.52}$$

where ρ_u is the unburnt gas density. Both equations omit explicit source terms since the heat release is embedded in the enthalpy definitions.

4.8.1. Enthalpy Models

To compute temperature from enthalpy, OpenFOAM provides multiple models:

- **Constant Heat Coefficients:** In the simplest case (`hConst`), the specific heat capacity c_p is assumed constant. The relation between enthalpy and temperature simplifies to:

$$h = c_pT + \Delta h_f \quad \rightarrow \quad T = \frac{h-\Delta h_f}{c_p}, \tag{4.53}$$

where Δh_f is the heat of formation. This approach is computationally efficient but insufficient for high-temperature reacting flows.

- **Temperature-Dependent Heat Coefficients:** To account for temperature variations of c_p, polynomial models are used. In this work, the JANAF thermodynamic database is employed due to its accuracy across a wide temperature range. Thermodynamic quantities are calculated as:

$$\frac{hM}{RT} = \sum_{i=0}^{N} \left[\frac{Y_i}{M_i} \left(\sum_s \frac{M_s}{Y_s} \right) \right] \left(a_1' + \frac{a_2' T}{2} + \frac{a_3' T^2}{3} + \frac{a_4' T^3}{4} + \frac{a_5' T^4}{5} + \frac{a_6'}{T} \right), \tag{4.54}$$

$$\frac{c_p M}{R} = \sum_{i=0}^{N} \left[\frac{Y_i}{M_i} \left(\sum_s \frac{M_s}{Y_s} \right) \right] \left(a_1' + a_2' T + a_3' T^2 + a_4' T^3 + a_5' T^4 \right), \tag{4.55}$$

$$\frac{sM}{R} = \sum_{i=0}^{N} \left[\frac{Y_i}{M_i} \left(\sum_s \frac{M_s}{Y_s} \right) \right] \left(a_1' \ln(T) + a_2' T + \frac{a_3' T^2}{2} + \frac{a_4' T^3}{3} + \frac{a_5' T^4}{4} + a_7' \right), \tag{4.56}$$

where a_j' are species-specific polynomial coefficients and M_i the molar mass of species i.

4.8.2. Transport Properties

Transport properties such as thermal diffusivity (α_{eff}) and dynamic viscosity (μ) are computed based on the mixture composition:

$$D_{\text{eff}} = D + D_t, \tag{4.57}$$

$$D = \frac{\kappa}{\rho c_p}, \quad D_t = \frac{\nu_t}{\text{Pr}_t}, \tag{4.58}$$

where κ is the thermal conductivity, ν_t is the turbulent viscosity, and Pr_t is the turbulent Prandtl number (commonly assumed unity).

The dynamic viscosity μ is evaluated using either:

- **Constant Viscosity (`const`):** μ is fixed throughout the simulation.
- **Temperature-Dependent Viscosity:** Sutherland's law is applied:

$$\mu = \frac{A_s \sqrt{T}}{1 + T_{\text{ref}}/T}, \tag{4.59}$$

where A_s and T_{ref} are mixture-specific parameters fitted from Cantera data.

4.8.3. Mixture Composition

Thermodynamic and transport properties are evaluated separately for reactants and products. A linear blending based on the regress variable b is used:

$$\text{mixture} = \begin{cases} \text{products}, & b < 0.001, \\ b \cdot \text{reactants} + (1-b) \cdot \text{products}, & 0.001 \leq b \leq 0.999, \\ \text{reactants}, & b > 0.999. \end{cases}$$

4.8.4. Tools and Preprocessing

Thermodynamic properties for the initial mixture are computed using `Cantera` [70], an open-source tool for chemical equilibrium and transport properties. The preprocessed coefficients are then used by `OpenFOAM` to initialize fields and perform runtime evaluations.

4.9. Concluding Remarks

The description of the solver framework and the newly developed flame speed library is now complete. Finally, and as a recommendation to further increase the predictive capability of the solver, it is important

to note that no dedicated library is currently implemented to adapt the thermodynamic properties to the use of the mixture fraction. When only the regress variable $\tilde{b}$ is considered, the thermodynamics can be represented by two species only: reactants and products. However, when $\widetilde{Z}$ is included, the mixture can locally consist of fuel, oxidizer, or products. In the present formulation, only reactants and products are accounted for, whereas in reality, the individual components of the products (fuel and oxidizer) possess different thermodynamic and transport properties, which could be treated more accurately.

This chapter began with a discussion of the pressure–velocity coupling algorithms and their applicability, followed by an introduction to the baseline `XiFoam` solver. The solver was then validated using the Sod shock tube benchmark to verify its capability to capture both subsonic and supersonic features within a pressure-based framework. Subsequently, the key physical and numerical models required to represent turbulent combustion were presented, including:

- Flame radius calculation methods,
- Laminar flame speed correlations and correction models,
- Wrinkling factor Ξ formulations,
- Modelling of thermodynamic and transport properties.

The summary of modelling parameters adopted for all the simulations performed is highlighted in table 4.5. The chapter concluded with the presentation of the newly developed solvers `NRGXiFoam` and `ppNRGXiFoam`, alongside a detailed description of their implementation strategy. In particular, `ppNRGXiFoam` was extended to solve transport equations for the mixture fraction and its variance, as well as for the diluent mixture fraction and its variance, enabling the handling of partially premixed and stratified flows. Furthermore, a generic laminar flame speed library-referred to in this work as the Bentaib flame speed library was integrated into the solver and optimised for efficient computation.

The novel contributions of this work lie in the validation of the new `ppNRGXiFoam` solver for lean, stratified hydrogen-air mixtures, and in the modification, optimisation, and testing of the generic Bentaib flame speed library for its application to turbulent combustion modelling in `OpenFOAM`.

Table 4.5: Summary of modeling parameters adopted for the simulations

Modeling Aspect	**Choice Implemented**
Flame radius calculation	Axial-based method
Laminar flame speed correlation	Constant, Bentaib Approach 2, Bentaib Approach 3
S_L model	Unstrained laminar flame speed
Ξ model (wrinkling factor)	Zimont TFC closure

5

Results

In this chapter, the results and key findings of this work are presented. Having addressed the first research question regarding the range of applicability of a pressure-based solver and implemented the newly derived laminar flame speed correlations in `OpenFOAM`, the focus now shifts to the validation of the solvers, combustion model and newly implemented correlations through selected experimental test cases under different scenarios.

To begin, moving forward from the validation of the solver with Sod's shock tube problem, the ENACCEF-2 case is considered to test the shock-capturing capabilities of a pressure-based solver in the presence of combustion. Building upon this, the ENACCEF facility is investigated, where tests with both homogeneous and inhomogeneous hydrogen-air mixtures have been conducted. The solvers used in this work - `NRGXiFoam` and `ppNRGXiFoam`, are tested and validated against these experimental configurations to assess their performance under a range of relevant conditions.

5.1. ENACCEF-2: Flame Acceleration Enclosure

The experimental facility used to validate the combustion model implementation and the new solver is ENACCEF-2, which stands for *Enceinte d'Accélération de Flamme* (flame acceleration enclosure). This newly developed vessel is designed to investigate flame acceleration phenomena in confined geometries. Although the facility is still under active development and not all experimental results are publicly available, its configuration provides an excellent benchmark for testing the solver's capabilities in predicting shock-flame interactions and flame acceleration. In this work, the Step0 case is considered, where a homogeneous mixture of hydrogen and air is used to validate the implementation of the turbulent combustion model. This scenario also serves as a limiting case for partially premixed combustion providing an appropriate edge test, as this scenario provides an ideal benchmark to verify that the new solver `ppNRGXiFoam` correctly reduces to the base behaviour of `NRGXiFoam`.

5.1.1. Facility Description

The ENACCEF-2 enclosure consists of a vertical tube with a total height of 7.65 m and an internal diameter of 0.23 m. Nine annular obstacles (or baffles) are installed along the flow direction to promote flame acceleration by constraining the available cross-sectional area (see figure 5.1). The obstacles have a thickness of 4 mm and a blockage ratio defined as:

$$BR = 1 - \left(\frac{d}{D}\right)^2 \tag{5.1}$$

where d is the diameter of the obstacle and D is the inner diameter of the tube. For the obstacles used in this work, $BR = 0.63$.

The facility is assembled from nine submodules of three types (T1, T2, and T3), arranged vertically. Submodule T1 includes ports for gas sampling, sapphire windows for detecting flame passage using photomultipliers (PM), and pressure transducers to record combustion-induced pressure variations. Submodule T2 provides similar instrumentation but also features four rectangular windows ($282\ \mathrm{mm} \times 50\ \mathrm{mm}$) for optical access, enabling high-speed particle image velocimetry (PIV) measurements of the flow field ahead of the flame. The ignition system is located in Submodule T3, which houses the spark plug and a draining port.

5.1.2. Experimental Setup and Measurements

The Step0 experimental condition involves a premixed hydrogen-air mixture containing 13% hydrogen and 87% air by volume, at an initial temperature of 363 K and a pressure of 1 bar. Prior to filling, the vessel is evacuated to a residual pressure of 80 Pa to ensure the removal of residual gases from previous tests. The mixture is prepared by blending high-purity hydrogen (99.95%) with dried air and introduced into the vessel at atmospheric pressure. Combustion is initiated at the bottom of the facility using a spark plug.

The instrumentation enables measurement of flame arrival times, determined from voltage drops in the photomultipliers, and calculation of flame front velocities from the flame trajectory. Pressure transducers record the dynamic pressure profiles along the enclosure height. Figure 5.2 illustrates the physical configuration of the facility and highlights key phenomena such as the incident and reflected shock waves. The initial flame acceleration in the baffles leads to the formation of a shock wave, which travels upwards and subsequently reflects at the top of the vessel, resulting in complex flame-shock interactions.

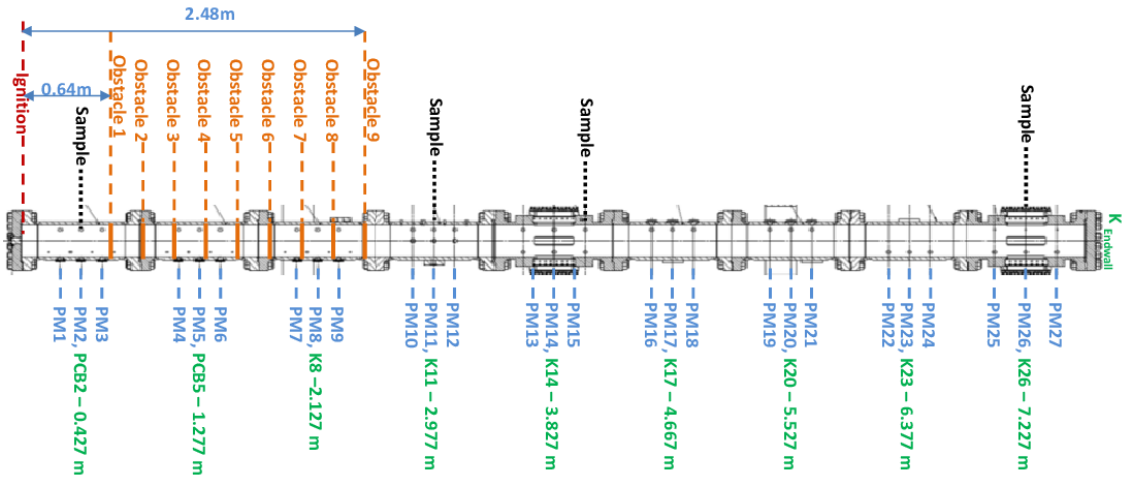

Figure 5.1: Diagram of the ENACCEF-2 facility [33]), the real orientation of the vessel is vertical

Relevance for Validation

The ENACCEF-2 facility provides a rigorous and multi-faceted validation environment for turbulent combustion solvers. Its vertically confined geometry, combined with repeated flame-shock interactions and accelerating flame fronts, presents a demanding scenario for numerical modeling. These characteristics are representative of critical safety scenarios in nuclear containment environments, making the facility particularly suitable for benchmarking solver robustness.

Two key aspects underscore the relevance of ENACCEF-2 for this study:

- **Shock-Capturing in Confined Geometries:** The facility enables assessment of shock-capturing capabilities by a pressure-based solver in the presence of combustion, under highly confined and obstacle-rich conditions. Additionally, it provides the opportunity to validate the turbulent combustion model (TFC) by analyzing flame–shock interactions and the accurate resolution of

reflected pressure waves in conjunction with turbulent flame fronts.

- **Limiting Case Test of the Solver:** The Step0 test case, involving a spatially uniform hydrogen-air mixture, serves as a limiting case for partially premixed combustion. This provides an ideal benchmark to verify that the newly implemented `ppNRGXiFoam` solver correctly reduces to the expected behavior of the base `NRGXiFoam` formulation. Successful reproduction of results in this edge case builds confidence in the solver's correctness and consistency when transitioning to a premixed from a partially premixed regime.

Future experimental campaigns at ENACCEF-2 will expand its validation potential further, incorporating tests with stratified mixtures, diluents, variable ignition locations, and temperature or species gradients. These enhancements will provide progressively complex scenarios to evaluate the generality and applicability of the implemented numerical models.

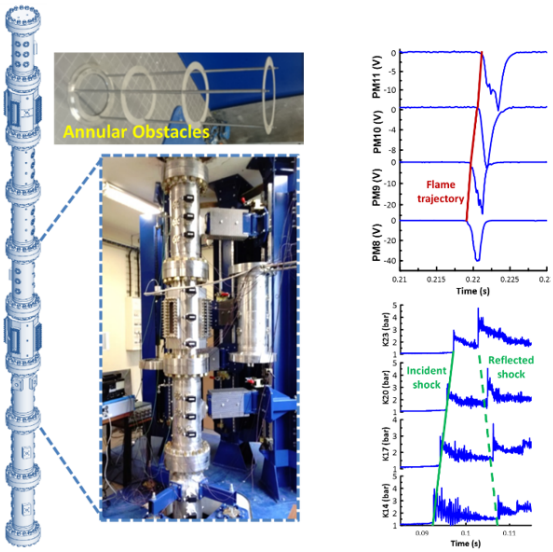

Figure 5.2: Physical appearance of ENACCEF-2 facility and illustration of relevant phenomena, including flame acceleration, incident and reflected shock waves. Adapted from [33]

5.1.3. Numerical Simulation Setup

The numerical setup for the ENACCEF-2 simulations follows the methodology described in the work of Lobato Pérez [30] and is reproduced here to evaluate the performance of the newly implemented solver. The computational mesh for the ENACCEF-2 facility was generated using OpenFOAM's native utilities. A 2D axisymmetric wedge mesh was created by revolving a rectangular domain with `extrudeMesh`, capturing the cylindrical geometry efficiently. The mesh includes both the acceleration tube and the dome, with hexahedral cells discretized using `blockMesh`. Nine annular obstacles were inserted as zero-thickness baffles via `createBafflesDict`, matching the experimental configuration. Local mesh refinement was performed near the ignition zone using `refineMesh` to resolve transient gradients. Mesh quality constraints were enforced, and boundary patches were assigned appropriate types for axisymmetric simulations.

Overview of Simulations

To systematically examine the shock capturing capabilities of the baseline solver `NRGXiFoam`, and validate the performance and robustness of the new solver `ppNRGXiFoam`, a structured test plan was adopted for the ENACCEF-2 facility. The test matrix comprises three stages:

1. **Mesh Sensitivity Study:** Using the baseline solver (`NRGXiFoam`) with a fixed 13% hydrogen-air mixture, five different mesh resolutions were tested to identify a mesh-independent solution while maintaining computational efficiency.

2. **Solver Consistency Test:** The solver (`ppNRGXiFoam`) was benchmarked against `NRGXiFoam` on the selected mesh to assess whether the new solver correctly reproduces expected results in a uniformly premixed mixture. This test serves as an edge case for the partially premixed model, verifying that the solver correctly reduces to the known behavior in the uniform limit.
3. **Flame Speed Correlation Validation:** The newly implemented flame speed model was evaluated within `ppNRGXiFoam`, the constant flame speed against the Bentaïb correlation-based formulation using the new flame speed library. These models were validated by comparing simulation outputs against available experimental data for Step0 conditions.

All simulations were performed under Step0 conditions - defined as a uniformly mixed 13% hydrogen–air mixture - representing the base case for validation. The test case description is summarized in Table 5.1.

Table 5.1: Step0 test case for ENACCEF-2 validation.

RUN	[H_2] vol.%	Blockage ratio	Gas mixture
Step0	13	0.63	Uniform hydrogen–air mixture

Initial and Boundary Conditions

The simulations were initialized with stagnant flow conditions, i.e., the velocity field was set to zero throughout the domain. As the ENACCEF-2 experiments do not report measurements of turbulence quantities such as turbulent kinetic energy (k) or turbulent length scale (l), representative values were adopted based on prior validation studies [30].

The initial turbulent kinetic energy was prescribed as $1.5 \times 10^{-4}\,\mathrm{m}^2/\mathrm{s}^2$, and the corresponding turbulent dissipation rate (ε) was set to $4.8 \times 10^{-5}\,\mathrm{m}^2/\mathrm{s}^3$. These values imply a characteristic turbulent length scale of 7 mm and a turbulent intensity of approximately 0.01 m/s. It is important to emphasize that these turbulence parameters were not tuned to fit experimental observations; rather, they were adopted as nominal inputs and kept fixed across all runs. This modeling assumption is consistent with previous validation efforts in similar hydrogen deflagration studies [35].

Boundary conditions were assigned to all fields based on physical assumptions consistent with the ENACCEF-2 facility. A no-slip boundary condition was applied to the velocity field (equivalent to a fixed value of 0 m/s), while thermal and turbulence fields followed standard wall-function treatments where applicable. The complete set of boundary and initial conditions for all transported variables is summarized in Table 5.8.

Table 5.2: Boundary conditions for the ENACCEF-2 enclosure. Subscript zero represents the conditions used to initialize the fields.

Field	Wall patches	Initial value
`alphat`	`fixedValue`	0
`b`	`zeroGradient`	–
`epsilon`	`epsilonWallFunction`	ε_0
`k`	`kqRWallFunction`	k_0
`nut`	`nutkWallFunction`	0
`omega`	`omegaWallFunction`	ω_0
`p`	`zeroGradient`	–
S_L	`zeroGradient`	–
`T`	`fixedValue`	363.0
`U`	`noSlip`	–
`Xi`	`zeroGradient`	–

Thermophysical Property Modeling

The calculation of thermodynamic and transport properties was carried out using OpenFOAM's built-in `heheuPsiThermo` framework, combined with the `janaf` thermodynamic model, the `perfectGas` equation of state, and a `homogeneousMixture` approach. Thermochemical data (such as molecular weight, Δh_f, and polynomial coefficients for $c_p(T)$) were extracted from Cantera [70] for hydrogen–air mixtures according to the compositions for each RUN mentioned previously. The coefficients were then fitted and used within OpenFOAM for runtime property evaluation. This modeling approach enables efficient and accurate coupling of chemical energy release with transport equations, ensuring that the flame propagation is correctly influenced by local mixture composition and temperature-dependent thermodynamic properties. The thermophysical and transport properties for the ENACCEF-2 Step0 case are summarized in section C.1.

Numerical Methods and Solver Configuration

The governing equations for mass, momentum, energy, species transport, and turbulent scalars are solved using a segregated approach within the PIMPLE algorithm to ensure stability in transient simulations. All cases in this work were simulated using the `NRGXiFoam` solver, with the Turbulent Flame Closure (TFC) model employed to account for flame wrinkling due to turbulence. The laminar flame speed was computed using the *Constant S_L Model* under the *Unstrained* assumption, consistent with the implementation described in section 4.6.

The flame front location was determined using the *Axial-Based Radius Calculation Method* (described in section 4.5), which is particularly suited for configurations where the flame propagates predominantly in a single direction.

Time integration was performed using the second-order backward Euler scheme, with dynamic time-stepping controlled by the CFL condition. A maximum Courant number of 0.1 was enforced, and a constant upper time step limit of $\Delta t_{\max} = 0.1$ was applied. The minimum time step was set to $1 \times 10^{-6}\,\mathrm{s}$, which would be relevant during ignition and early flame development.

Second-order accurate schemes were employed for spatial discretization, based on the studies performed on the Sod shock tube:

- **Gradient terms:** `Gauss linear`
- **Divergence terms:** `limitedLinear` with limiter coefficient 1
- **Laplacian terms:** `Gauss linear corrected`
- **Interpolation:** `Linear`

All numerical schemes - including the time integration and spatial discretization methods - were selected based on detailed sensitivity analyses from the Sod shock tube tests. This ensured that the chosen configurations would reliably capture sharp gradients and wave dynamics while maintaining numerical stability in the ENACCEF-2 simulations.

Linear systems arising from discretization were solved using Krylov subspace solvers:

- **Pressure and density fields:** Solved with `PBiCG` using `DILU` preconditioning, with absolute tolerances of 10^{-10}.
- **Scalar fields:** Velocity, turbulence quantities, and species fractions were solved using `PBiCG` or `smoothSolver` with `symGaussSeidel` smoothing.

Coupled pressure-velocity iterations were handled using a PIMPLE loop with two outer correctors and one inner corrector, and the `transonic` option was enabled. Residual-based convergence criteria were applied to velocity, turbulent kinetic energy, and specific dissipation rate to ensure solution accuracy.

Additional Considerations

The simulation setup employs adaptive time-stepping and includes libraries for the specialized laminar flame speed models (i.e., Bentaib flame speed library). The implementation of this flame speed library

will be tested and validated in this study to ensure their reliability under varying conditions. Field probes are enabled for tracking pressure, velocity, and species evolution at specified locations throughout the domain.

Overall, the numerical framework is tailored to handle the rapid transients and steep gradients characteristic of hydrogen deflagration in confined geometries, while maintaining solution stability and accuracy across the entire domain.

5.1.4. Results - Step0

Flame Propogation Dynamics in ENACCEF-2

Before initiating the mesh sensitivity studies, it is essential to first understand the key physics occurring within the ENACCEF-2 configuration. Figure 5.3 presents a series of Schlieren contours illustrating the evolution of the shock and flame interaction within the confined tube.

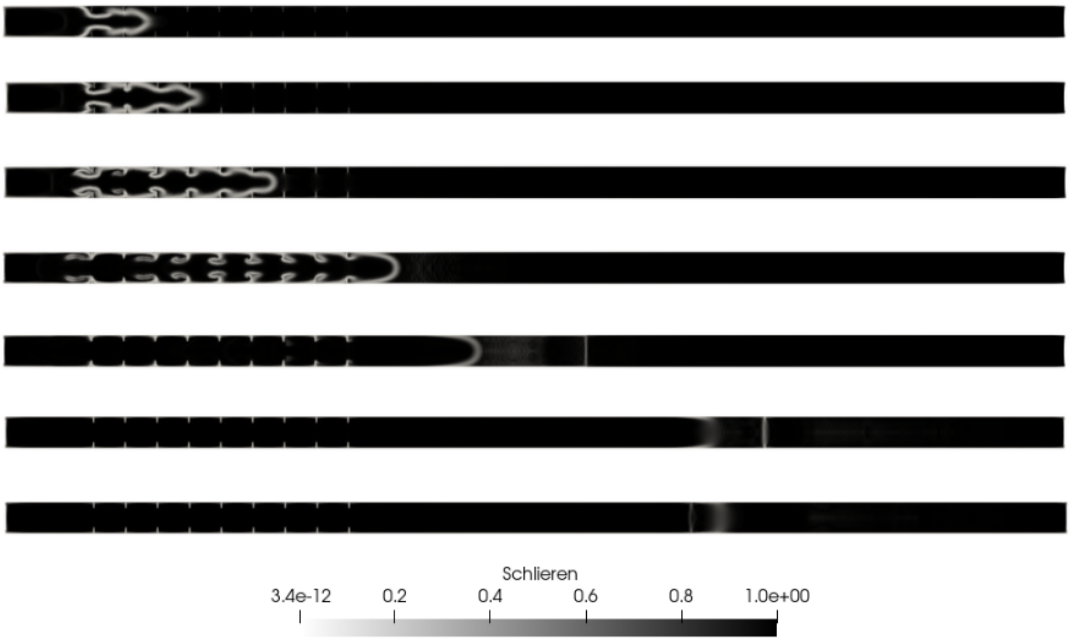

Figure 5.3: Schlieren visualization of the ENACCEF-2 simulation showing shock–flame interaction

Immediately after ignition, the flame propagates slowly through the initially quiescent mixture. As it encounters the annular baffles placed along the length of the tube, turbulence is generated, resulting in a sharp increase in the flame front velocity. This rapid flame acceleration produces a steep pressure rise, leading to the formation of a detached shock wave ahead of the flame front.

This shock wave propagates rapidly downstream and reflects off the closed upper boundary of the tube. The reflected wave then travels back upstream and impinges on the advancing flame front, causing a sudden stagnation in its motion and reducing the flame speed to zero. This moment is clearly visible in the Schlieren visualization, where the flame front appears arrested. Over time, the shock continues to reflect between the tube walls, gradually weakening due to dissipative losses. The progressive attenuation of shock intensity is seen as the Schlieren gradients diminish in the later frames.

The transient pressure and flame evolution during this period is presented in Figure 5.4. The plot shows

pressure probe signals along the axis of the tube, along with the predicted flame front position from simulation (blue line) and experimental flame tracking data (black dots). Initially, the flame advances steadily through the early section of the domain and then accelerates rapidly in the region with obstacles, as expected.

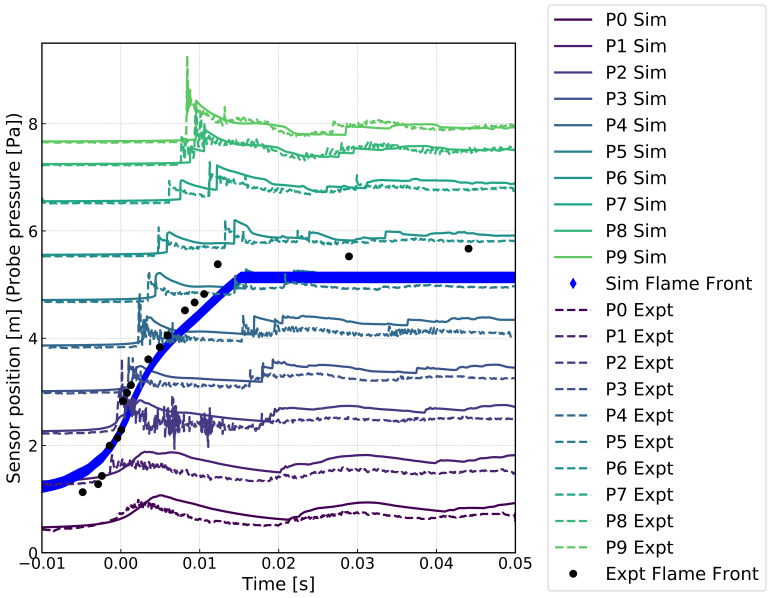

Figure 5.4: Axial pressure evolution and flame front position from simulation and experiment.

As the flame progresses downstream, the leading shock gains strength and reflects off the top of the tube, returning as a wave that disrupts the flame propagation. This is the point at which the flame front abruptly slows down and stagnates, visible as a sudden plateau in the flame trajectory. As seen in the plot, each time the shock travels across a pressure probe, a sharp spike is registered in the corresponding pressure trace. The magnitude of these spikes gradually diminishes in successive reflections, indicating the decay in shock strength. The process repeats with subsequent reflections, eventually leading to full attenuation of the pressure wave.

The flame–shock interaction and the repeated shock reflections are critical to reproduce accurately, as they test the solver's capability to resolve compressible flame dynamics in confined geometries. The ENACCEF-2 case, therefore, offers a demanding benchmark for assessing both turbulence–combustion interaction and transient shock handling in reacting flow solvers.

Mesh Independence Analysis

In RANS-based simulations, ensuring mesh independence is critical to establishing the reliability and generality of the numerical solution. A solution that exhibits strong dependence on the underlying mesh cannot be considered physically robust or predictive. Therefore, a detailed mesh sensitivity analysis was carried out for the ENACCEF-2 configuration using the Step0 case as the test scenario. The mesh configurations and their corresponding run times are summarized in Table 5.3.

Table 5.3: Mesh configurations and simulation run times used in the grid sensitivity study.

Mesh	Total cells	Run time (s)
M1	7,600	2,567
M2	35,400	6,587
M3	141,600	35,125
M4	566,400	159,876

Figure 5.5 presents the flame front velocity as a function of axial flame location for all four meshes,

alongside the experimental data. The results demonstrate a clear dependence of the predicted flame dynamics on grid resolution. Mesh M1, the coarsest configuration, underpredicts the flame speed significantly and fails to capture the sharp acceleration occurring between 1.5-3.5 m, corresponding to the region of maximum turbulence generation. M2 shows an improvement, capturing the qualitative trend but still lagging in peak velocity prediction.

A notable transition is observed with Mesh M3, which matches the experimental flame acceleration and deceleration phases with high accuracy. The peak flame velocity is well captured, and the flame slows down appropriately after obstacle interaction ceases.

Interestingly, Mesh M4 - despite having four times the resolution of M3 - shows a slight underprediction of the peak velocity. This deviation may be attributed to increased numerical dissipation at higher resolutions. However, distinguishing whether this behavior stems from over-resolution of small-scale flow features or from solver-induced dissipation requires further investigation.

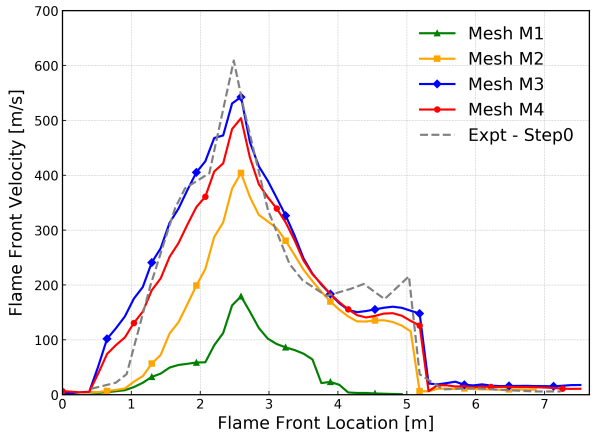

Figure 5.5: Flame front velocity as a function of flame front location for different mesh resolutions in the ENACCEF-2 Step0 case. Experimental data is included for comparison.

To probe further mesh convergence, a fifth mesh (M5) with approximately 2 million cells was considered. However, given the already significant computational expense of M4 (over 44 hours), and the marginal gains observed between M3 and M4, this simulation was not pursued. Mesh M3 was therefore selected as the reference configuration for all subsequent studies. It offers an optimal trade-off between numerical accuracy and computational cost, and it reproduces the flame dynamics with sufficient resolution and physical consistency.

Validation for `ppNRGXiFoam`

Before evaluating the newly implemented flame speed models through the Bentaib Flame Speed Library, it is essential to verify that the baseline behavior of the new solver `ppNRGXiFoam` matches that of the established `NRGXiFoam` implementation in the limiting case of a spatially uniform hydrogen–air mixture. This scenario corresponds to the Step0 configuration of the ENACCEF-2 experiments, and serves as a strict benchmark: since partial premixing is absent, both solvers should reproduce identical flame dynamics governed purely by the TFC combustion model.

Accordingly, the variance in the mixture fraction field was set to zero ($Z''^2 = 0$) and `solveZp = false`, thus effectively recovering the behavior of a premixed configuration while leveraging the `ppNRGXiFoam` framework. The diluent-related fields and transport equations were also deactivated to maintain consistency with the experimental conditions of Step0.

The initial and boundary conditions, as well as numerical schemes and thermophysical models, were retained from the original configuration to ensure a direct comparison. In addition to the standard regress variable b, the mixture fraction $\widetilde{Z}$ was initialized to a constant value representing the equivalence ratio of the test case.

Figure 5.6 shows the flame front velocity as a function of flame front location for both solvers, overlaid with experimental data. The agreement between the solvers is excellent throughout all phases of flame propagation. Both predict the acceleration zone, peak flame speed, and subsequent deceleration with comparable accuracy. Notably, the numerical predictions are also consistent with the experimental trends in terms of both magnitude and location of peak flame speed, validating the solver's fidelity.

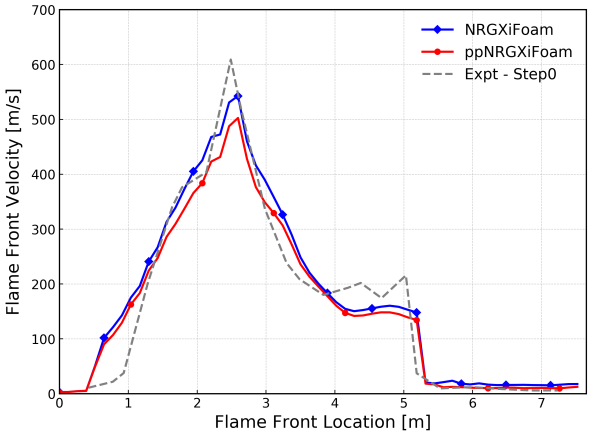

Figure 5.6: Flame front velocity vs. location for `NRGXiFoam` and `ppNRGXiFoam` compared to experimental results (Step0).

While the flame front predictions are consistent, a closer inspection of the time-stepping behavior reveals minor differences in solver dynamics. Figure 5.7a displays the variation of time step Δt over the course of the simulation. Both solvers enforce the same Courant condition and upper bound for Δt, and exhibit similar trends overall. However, zooming into the time window during which the flame undergoes peak acceleration and time steps rapidly decrease, (Figure 5.7b) reveals that `ppNRGXiFoam` sustains a slightly larger time step for longer durations. This could explain the minor deviations in the results of Figure 5.6.

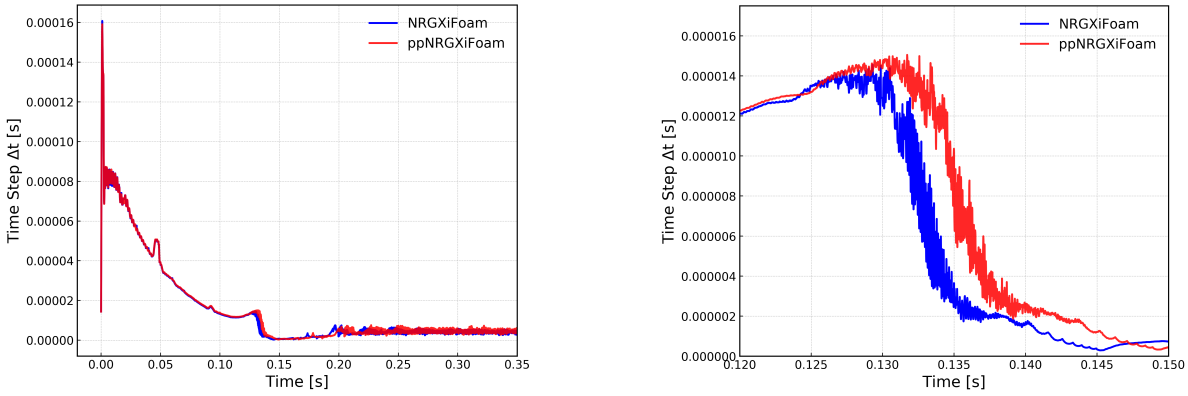

(a) Time step evolution for the entire simulation duration.

(b) Zoomed view near peak flame acceleration.

Figure 5.7: Comparison of time step behavior between `NRGXiFoam` and `ppNRGXiFoam`.

These subtle distinctions in adaptive time stepping arise due to implementation-level differences in how the two solvers update flame propagation terms and evaluate local Courant numbers during stiff transitions. However, their impact on the solution is negligible, and the flame trajectory remains largely unaffected.

To complement the flame speed and time step analysis, Figure 5.8 shows a combined view of the pressure probe signals and flame front trajectories for both solvers, overlaid against experimental measurements from the Step0 case. Each curve represents the temporal evolution of pressure at a fixed axial sensor location, while the flame front path is traced using symbols across time.

The flame front motion predicted by both `NRGXiFoam` and `ppNRGXiFoam` is virtually identical in shape and timing, closely tracking the experimental flame front (black dots) up to the point of shock–flame interaction. The pressure peaks at each sensor location are also in excellent agreement with experiment, capturing the shock arrival time and strength accurately, with minor amplitude differences.

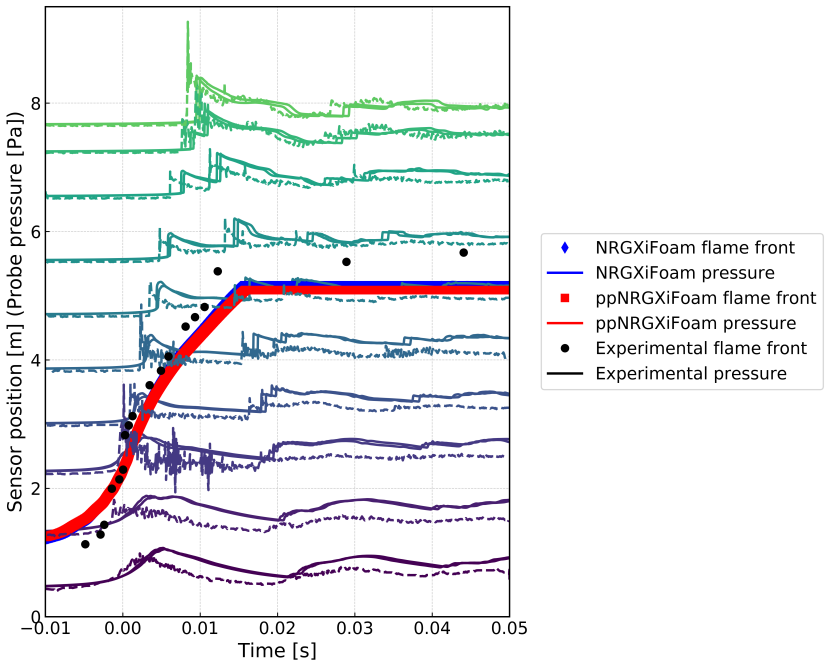

Figure 5.8: Comparison of axial pressure traces and flame front trajectories from simulation and experiment.

Importantly, both solvers reproduce the timing of the initial shock wave, the flame deceleration following shock reflection, and the subsequent pressure oscillations. This validates that the partially premixed extensions introduced in `ppNRGXiFoam` do not alter its core behavior when applied to a homogeneously premixed flame.

This test confirms that `ppNRGXiFoam` faithfully reproduces the base solver behavior in the absence of premixing effects, and therefore serves as a robust foundation for further model extensions.

Validation of the Flame Speed Correlation Implementation

In the final step of ENACCEF-2 validation, the focus shifts to evaluating the implementation and behavior of the newly incorporated flame speed correlation. Two laminar flame speed models were compared using the `ppNRGXiFoam` solver: a constant flame speed model, and the Bentaïb flame speed library that dynamically computes S_L based on local pressure and temperature.

Given that the Step0 configuration involves a spatially uniform hydrogen-air mixture, the laminar flame speed should ideally remain constant throughout the simulation. This presents an ideal testbed for isolating numerical effects and verifying the flame speed correlation logic. In the first approach, the laminar flame speed is calculated at the initial thermodynamic conditions using the Bentaïb correlations in Cantera, and is held constant throughout the simulation (see equation 4.17). In the second approach, the same correlation is embedded into the OpenFOAM framework and used to dynamically evaluate S_L at each time step, incorporating corrections due to evolving pressure and temperature. This dynamic implementation corresponds to Bentaïb Approach 3 as defined in Equation (4.29).

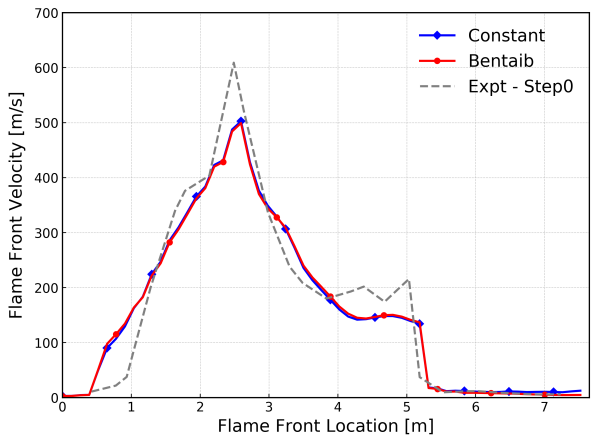

Figure 5.9: Comparison of flame front velocity profiles for the constant S_L model and the dynamic Bentaïb library in the ENACCEF-2 Step0 case.

Figure 5.9 shows the flame front velocity plotted against its axial location for both models, along with experimental data. The predictions from both approaches exhibit excellent agreement with the measured flame propagation, capturing the sharp acceleration phase and subsequent deceleration with high fidelity. This close match confirms two important observations.

First, it validates that the Bentaïb flame speed library has been correctly implemented in `OpenFOAM`. The dynamically calculated flame speed closely follows the trajectory of the constant S_L model, with only minor deviations near the flame acceleration peak. These small differences arise from the pressure and temperature corrections applied at each time step in the dynamic model, which slightly modulate the local burning velocity. Second, the comparison demonstrates that for a uniform mixture such as Step0, the impact of these thermodynamic corrections on the global flame behavior is relatively minor.

Final Remarks for Step0

The Step0 simulation campaign marks the successful completion of all key objectives defined for the ENACCEF-2 validation phase. First, the Turbulent Flame Closure (TFC) model has demonstrated its effectiveness in capturing the dynamics of turbulent flame acceleration and flame - shock interactions in confined environments. This confirms its suitability for modeling combustion regimes characterized by high-pressure gradients and transient flame front behavior.

Second, the pressure-based `ppNRGXiFoam` solver has proven to be robust and accurate when tested against its limiting case - a spatially uniform hydrogen–air mixture - by reproducing the results obtained from the validated `NRGXiFoam` formulation. This ensures that the newly extended solver maintains consistency with the theoretical expectations of premixed combustion in the absence of mixture inhomogeneity.

Finally, the implementation of the Bentaïb flame speed library within OpenFOAM has been rigorously tested and shown to perform as intended. Both constant and dynamically evaluated flame speed models were applied, with consistent agreement in flame front trends, thereby verifying the accuracy of the runtime interpolation and correlation routines.

With the numerical framework now fully verified under these controlled conditions, the next stage of the study shifts focus to the ENACCEF facility. This earlier experimental platform offers a broader range of test scenarios, including both homogeneous and inhomogeneous mixture configurations. Details of these configurations and their relevance to practical hydrogen safety assessments are discussed in Section 5.2.

5.2. ENACCEF: The First Flame Acceleration Enclosure

The ENACCEF facility (*Enceinte d'accélération de flamme*) is a closed-vessel experimental setup developed to investigate hydrogen deflagration under geometries and thermodynamic conditions representative of nuclear reactor containment. Designed and operated prior to ENACCEF-2, the facility played a pivotal role in post-Fukushima research efforts and provided the experimental foundation for numerous combustion modeling studies.

The test environment is highly configurable, allowing for a wide range of ignition scenarios including homogeneous hydrogen–air mixtures, stratified configurations, and cases involving inert diluents such as helium or carbon dioxide. This makes ENACCEF particularly suited for evaluating combustion models across varying degrees of complexity.

In this study, two representative test cases from ENACCEF are selected to continue the validation and extension of the numerical framework:

- **RUN 153:** A spatially uniform hydrogen–air mixture, used to verify solver consistency and cross-validate results obtained from ENACCEF-2. This case provides a baseline for assessing flame acceleration and pressure dynamics in the absence of mixture inhomogeneity.
- **RUN 765:** A stratified hydrogen–air mixture with axial variation in composition. This case introduces mixture fraction gradients and is used to evaluate the solver's ability to accurately simulate partially premixed combustion regimes.

The transition from RUN 153 to RUN 765 enables a stepwise increase in modeling complexity—from validating the solver in homogeneous conditions to investigating its robustness in the presence of mixture inhomogeneity. This is aligned with the core research goals presented in Chapter 1, where the following questions were posed:

- Can a pressure-based solver reliably simulate combustion under accident-relevant, stratified mixture conditions?
- Does the inclusion of mixture fraction variance (Z''^2) improve the predictive fidelity of the model in such scenarios?

The ENACCEF facility offers the necessary experimental data and physical configurations to investigate these questions systematically. The following sections present simulation results for both RUN 153 and RUN 765 using the validated solver setup developed from ENACCEF-2, with particular emphasis on quantifying the effects of mixture inhomogeneity and evaluating the performance of the extended modeling framework.

5.2.1. Facility Description

The ENACCEF setup consists of two vertically aligned cylindrical sections. The first section, referred to as the *acceleration tube*, is 3.3 m tall with an internal diameter of 0.154 m. It incorporates a series of annular obstacles designed to enhance turbulence and promote flame propagation. The second section, known as the *dome*, is 1.7 m in height and has a larger internal diameter of 0.738 m. The dome acts as an expansion chamber, accommodating the combustion products following ignition. An overview of the facility and geometry is shown in Figures 5.10 and 5.11.

In this Facility, the annular obstacle configuration was fixed at a height of 4 mm, with a total of nine obstacles evenly spaced at 0.154 m intervals along the acceleration tube. One of the key geometric parameters used to characterize the obstacle configuration is the blockage ratio (BR), which is defined previously in Equation (5.1).

For the present test configurations, the blockage ratio was set to 0.63.

Figure 5.10: Photos of the ENACCEF facility [33]

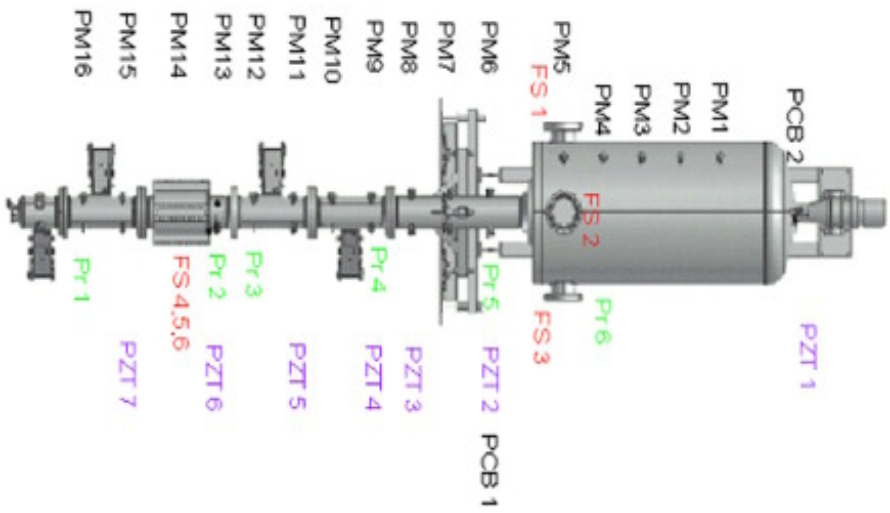

Figure 5.11: ENACCEF schematic with obstacle configuration and ignition location [33] (real orientation is vertical)

Ignition is initiated 0.138 m from the bottom of the acceleration tube using two tungsten electrodes, each 2 mm in diameter. The ignition energy required for flame initiation is in the range of 10-20 mJ.

The facility is instrumented with pressure transducers, flame sensors, and gas analyzers to monitor pressure rise, flame front propagation, and mixture composition throughout the experiment. This level of instrumentation ensures that detailed spatio-temporal data are available for model validation.

5.2.2. Experimental Setup and Measurements

The ENACCEF facility is equipped with an extensive array of diagnostic tools designed to capture transient phenomena associated with hydrogen deflagration, including flame acceleration, pressure waves, and shock reflections. The schematic in Figure 5.11 illustrates the sensor layout, showing the positions of pressure transducers (PM), piezoelectric transducers (PZT), photomultiplier tubes (FS), and PCB sensors along the vertical axis of the setup.

Pressure Measurements: Pressure transducers are distributed throughout the height of the facility, with a dense concentration in the acceleration tube to capture high-frequency events such as flame-induced pressure rise and shock reflections. Table 5.4 lists the PM sensor positions with respect to the ignition point, and these can also be visually located in Figure 5.11.

Table 5.4: Pressure transducer positions relative to the ignition point, corresponding to PM sensors in Figure 5.11.

Sensor	Distance from ignition point [m]
PM1	4.3415
PM2	4.0915
PM3	3.8415
PM4	3.5915
PM5	3.3415
PM6	2.8770
PM7	2.6270
PM8	2.3770
PM9	2.0370
PM10	1.7720
PM11	1.5270
PM12	1.2770
PM13	1.0270
PM14	0.7770
PM15	0.5270
PM16	0.2770

Additional high-frequency transducers (PZT) and PCB sensors are also installed near critical locations, particularly around the dome-acceleration tube interface. These are summarized in Table 5.5. Their placement provides detailed local measurements of shock wave characteristics and flame–structure interactions, as indicated in the schematic.

Table 5.5: Additional pressure and piezoelectric sensor positions, also shown in Figure 5.11

Sensor	Distance from ignition point [m]
PCB2	4.879
PCB1	2.877
PZT1	4.779
PZT2	2.627
PZT3	2.377
PZT4	2.139
PZT5	1.527
PZT6	1.027
PZT7	0.527

Flame Front Detection: The flame front is tracked using photomultiplier tubes (FS in the schematic), which detect ultraviolet radiation emitted by combustion radicals such as OH and CH. The detection wavelength is centered around 306–309 nm, where OH emission peaks, enabling high-fidelity measurement of flame arrival at various axial locations. These sensors are critical for deriving flame speed profiles and validating flame propagation models.

Experimental Test Matrix: To facilitate combustion model validation and inter-code comparison, a number of ENACCEF test cases have been made publicly available by IRSN through collaborative research initiatives. The test matrix relevant to this work is summarized in Table 5.6, comprising both homogeneous and stratified hydrogen-air mixtures.

Table 5.6: ENACCEF experiments selected for CFD code benchmarking and validation.

RUN	[H_2] vol.%	Blockage ratio	Gas mixture
153	13	0.63	Uniform hydrogen–air mixture
765	11.6–8.1	0.63	Hydrogen–air mixture with negative concentration gradient
736	11.4–5.8	0.63	Hydrogen–air mixture with negative concentration gradient
733	5.7–12	0.63	Hydrogen–air mixture with positive concentration gradient

All experiments were conducted at ambient conditions of 296 K and 100 kPa. However, it is important to note that neither initial turbulence levels nor wall heat losses were measured or reported for these tests. These omissions introduce some modeling uncertainty, which is accounted for in the simulation assumptions.

This carefully instrumented experimental configuration, combined with the availability of both uniform and non-uniform mixture cases, makes ENACCEF a valuable platform for systematically validating the turbulent combustion model and extended solver capabilities under increasingly complex conditions.

5.2.3. Numerical Simulation Setup

The computational mesh for the ENACCEF facility was generated using OpenFOAM's native utilities, similar to the meshing described for ENACCEF-2. A 2D axisymmetric wedge mesh was created by revolving a rectangular domain with `extrudeMesh`, capturing the cylindrical geometry efficiently. The mesh includes both the acceleration tube and the dome, with hexahedral cells discretized using `blockMesh`. Nine annular obstacles were inserted as zero-thickness baffles via `createBafflesDict`, matching the experimental configuration. Local mesh refinement was performed near the ignition zone using `refineMesh` to resolve transient gradients. Mesh quality constraints were enforced, and boundary patches were assigned appropriate types for axisymmetric simulations.

Overview of Simulations

To build upon the insights gained from the ENACCEF-2 facility and further validate the robustness of the numerical framework, a comprehensive simulation campaign was conducted using the ENACCEF configuration. The objective was to assess whether the solver and combustion models maintain predictive accuracy under slightly different geometric conditions and mixture configurations. The test matrix is organized in two stages, beginning with a uniform mixture (RUN 153) and progressing toward a stratified mixture (RUN 765).

RUN 153 – Uniform Mixture Studies: This test case replicates the modeling goals of ENACCEF-2 under a different geometry. It is used to evaluate the following aspects:

1. **Mesh Sensitivity Study:** Multiple grid resolutions were used with the `NRGXiFoam` solver to determine a mesh-independent solution while balancing computational cost.
2. **Turbulence Model Comparison:** The effect of different turbulence closures was examined using RUN 153 to evaluate how flame acceleration and pressure dynamics are affected by the turbulence model.
3. **Solver Consistency Test:** The new solver `ppNRGXiFoam` was benchmarked against the base `NRGXiFoam` using a uniformly premixed hydrogen–air mixture. This test reaffirms that `ppNRGXiFoam` reproduces expected behavior when mixture fraction variance is absent.
4. **Flame Speed Correlation Validation:** The newly implemented Bentaïb flame speed library was evaluated by comparing the results of constant S_L and dynamically computed S_L under homogeneous conditions.

These steps confirm that the solver performs consistently across facilities and geometries, thus establishing confidence in its general applicability.

RUN 765 – Stratified Mixture Study: Having established solver reliability in homogeneous mixtures, the focus then shifts to RUN 765 - a case with a negative hydrogen concentration gradient. This test is designed to investigate whether the inclusion of mixture fraction variance (Z''^2) in the solver leads to meaningful improvements in predicting flame propagation and pressure response in inhomogeneous conditions. The simulation plan includes:

1. **Evaluation of ppNRGXiFoam:** The solver is tested on a stratified mixture using a realistic distribution of hydrogen concentration.
2. **Variance Effect Assessment:** The role of mixture fraction variance is analyzed by enabling and disabling the Z''^2 term in the flame speed model, allowing direct comparison of results.

This tiered approach allows for a gradual increase in modeling complexity and provides a controlled framework to isolate the impact of stratification and turbulence–chemistry interaction.

Table 5.7: ENACCEF test cases used for numerical validation and inhomogeneity analysis.

RUN	[H_2] vol.%	Blockage Ratio	Mixture Description
153	13.0	0.63	Uniform hydrogen–air mixture (used for solver and model validation)
765	11.6–8.1	0.63	Stratified hydrogen–air mixture with negative concentration gradient

Table 5.7 summarizes the two key test cases used in this study. RUN 153 serves as the baseline configuration for verifying mesh sensitivity, turbulence models, solver behavior, and flame speed correlations. RUN 765 introduces stratification effects, offering the opportunity to examine the solver's capability in handling mixture inhomogeneity and the influence of mixture fraction variance on simulation outcomes.

Initial and Boundary Conditions

The simulations were initialized with stagnant flow conditions, i.e., the velocity field was set to zero throughout the domain. As the ENACCEF experiments do not report measurements of turbulence quantities such as turbulent kinetic energy (k) or turbulent length scale (l), representative values were adopted based on prior validation studies [35]. The initial turbulent kinetic energy was prescribed as $1.5 \times 10^{-4}\,\mathrm{m^2/s^2}$, and the corresponding turbulent dissipation rate (ε) was set to $4.8 \times 10^{-5}\,\mathrm{m^2/s^3}$. These values imply a characteristic turbulent length scale of 7 mm and a turbulent intensity of approximately 0.01 m/s. It is important to emphasize that these turbulence parameters were not tuned to fit experimental observations; rather, they were adopted as nominal inputs and kept fixed across all runs. This modeling assumption is consistent with previous validation efforts in similar hydrogen deflagration studies [35]. Boundary conditions were assigned to all fields based on physical assumptions consistent with the ENACCEF facility. A no-slip boundary condition was applied to the velocity field (equivalent to a fixed value of 0 m/s), while thermal and turbulence fields followed standard wall-function treatments where applicable. The complete set of boundary and initial conditions for all transported variables is summarized in Table 5.8.

Table 5.8: Boundary conditions for the ENACCEF enclosure. Subscript zero represents the conditions used to initialize the fields.

Field	Wall patches	Initial value
`alphat`	`fixedValue`	0
`b`	`zeroGradient`	–
`epsilon`	`epsilonWallFunction`	ε_0
`k`	`kqRWallFunction`	k_0
`nut`	`nutkWallFunction`	0
`omega`	`omegaWallFunction`	ω_0
`p`	`zeroGradient`	–
S_L	`zeroGradient`	–
`T`	`fixedValue`	363.0
`U`	`noSlip`	–
`Xi`	`zeroGradient`	–

Thermophysical Property Modeling

The calculation of thermodynamic and transport properties was carried out using OpenFOAM's built-in `heheuPsiThermo` framework, combined with the `janaf` thermodynamic model, the `perfectGas` equation of state, and a `homogeneousMixture` approach. Thermochemical data (such as molecular weight, Δh_f, and polynomial coefficients for $c_p(T)$) were extracted from Cantera [70] for hydrogen–air mixtures according to the compositions for each RUN mentioned previously. The coefficients were then fitted and used within OpenFOAM for runtime property evaluation. This modeling approach enables efficient and accurate coupling of chemical energy release with transport equations, ensuring that the flame propagation is correctly influenced by local mixture composition and temperature-dependent thermodynamic properties. The thermophysical and transport properties for the ENACCEF cases are summarized in section C.2.

Numerical Methods and Solver Configuration

The governing equations for mass, momentum, energy, species transport, and turbulent scalars are solved using a segregated approach within the PIMPLE algorithm to ensure stability in transient simulations. All cases in this work were simulated using the the Turbulent Flame Closure (TFC) model employed to account for flame wrinkling due to turbulence. The laminar flame speed was computed using the *Constant S_L Model* under the *Unstrained* assumption, consistent with the implementation described in section 4.6.

The flame front location was determined using the *Axial-Based Radius Calculation Method* (described in section 4.5), which is particularly suited for configurations where the flame propagates predominantly in a single direction.

Time integration was performed using the second-order backward Euler scheme, with dynamic time-stepping controlled by the CFL condition. A maximum Courant number of 0.1 was enforced, and a constant upper time step limit of $\Delta t_{\max} = 0.1$ was applied. The minimum time step was set to $1 \times 10^{-6}\,\mathrm{s}$, which would be relevant during ignition and early flame development.

Second-order accurate schemes were employed for spatial discretization, based on the studies performed on the Sod shock tube:

- **Gradient terms:** `Gauss linear`
- **Divergence terms:** `limitedLinear` with limiter coefficient 1
- **Laplacian terms:** `Gauss linear corrected`
- **Interpolation:** `Linear`

All numerical schemes - including the time integration and spatial discretization methods - were selected based on detailed sensitivity analyses from the Sod shock tube tests. This ensured that the chosen configurations would reliably capture sharp gradients and wave dynamics while maintaining numerical stability in the ENACCEF simulations.

Linear systems arising from discretization were solved using Krylov subspace solvers:

- **Pressure and density fields:** Solved with `PBiCG` using `DILU` preconditioning, with absolute tolerances of 10^{-10}.
- **Scalar fields:** Velocity, turbulence quantities, and species fractions were solved using `PBiCG` or `smoothSolver` with `symGaussSeidel` smoothing.

Coupled pressure-velocity iterations were handled using a PIMPLE loop with two outer correctors and one inner corrector, and the `transonic` option was enabled. Residual-based convergence criteria were applied to velocity, turbulent kinetic energy, and specific dissipation rate to ensure solution accuracy.

Additional Considerations

Similar to ENACCEF-2, this simulation setup employs adaptive time-stepping and includes libraries for specialized laminar flame speed models(i.e., Bentaib Flame Speed Library). The implementation of

this flame speed library will be tested and validated in this study to ensure their reliability under varying conditions. Field probes are enabled for tracking pressure, velocity, and species evolution at specified locations throughout the domain.

Overall, the numerical framework is tailored to handle the rapid transients and steep gradients characteristic of hydrogen deflagration in confined geometries, while maintaining solution stability and accuracy across the entire domain.

5.2.4. Results - RUN 153

Flame Propagation Dynamics in ENACCEF

Upon ignition, the combustion dynamics in the ENACCEF facility evolve through a series of physically distinct stages. The analysis presented here focuses on experimental runs (RUN 153 and RUN 765) and describes the various phases of flame propagation based on experimental measurements of flame location, flame speed, and pressure evolution.

The flame propagation is generally categorized into four phases: (i) quasi-laminar flame propagation, (ii) turbulent flame acceleration, (iii) flame deceleration, and (iv) jet flame expansion.

(i) Quasi-laminar flame propagation: Immediately after ignition, the flame begins to propagate through the quiescent premixed mixture. This phase is characterized by slow flame speeds due to low turbulence levels in the early part of the acceleration tube. The flame front progresses steadily and reaches the first obstacle (baffle), initiating the transition to the next regime. As seen in Fig. 5.12a, the axial flame position increases slowly at first, and Fig. 5.12b confirms the low flame front speed in this early phase.

(ii) Turbulent flame acceleration: Upon encountering the first baffle, the flame front experiences a sharp increase in velocity. This is attributed to the turbulence generated by the interaction of the flame with the obstacles. The wrinkling of the flame front and enhanced mixing due to turbulent eddies increase the overall burning rate. This phase continues until the flame reaches the last baffle. The steep rise in flame front speed during this period is evident in Fig. 5.12b, where velocities exceed $600\,\mathrm{m/s}$ in RUN 153.

(iii) Flame deceleration: After the last baffle, the turbulence levels begin to decay, and the flame slows down as it moves toward the dome. The decrease in flame front velocity is captured in the flame location versus speed plot (figure 5.12b). During this phase, pressure waves generated during the acceleration phase begin to interact with the flame, influencing local conditions.

As the flame approaches the dome, the geometry induces a recirculation zone due to abrupt expansion of the cross-sectional area. This recirculation promotes localized turbulence generation, leading to increased flame front wrinkling and a higher local burning rate. Consequently, the flame speed rises again in this transition region, even though the upstream turbulence levels are generally decaying.

(iv) Jet flame expansion: Upon entering the dome, the flame undergoes radial expansion, pushing unburnt gases outward and initiating a final, slower combustion phase. This phase is marked by the expansion of burned gases into a larger volume, accompanied by pressure redistribution. Although flame propagation slows, significant changes in pressure are observed due to the volumetric expansion of hot gases.

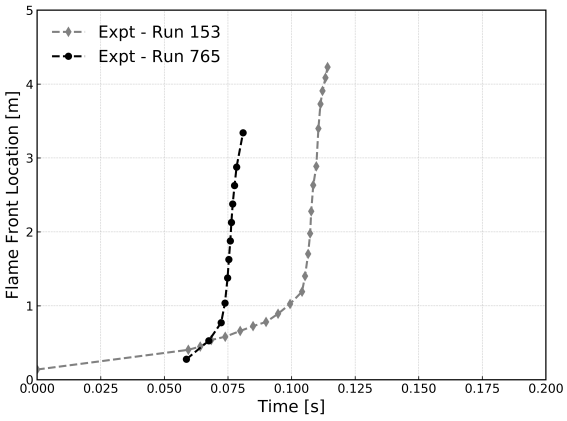

(a) Flame front location vs. time

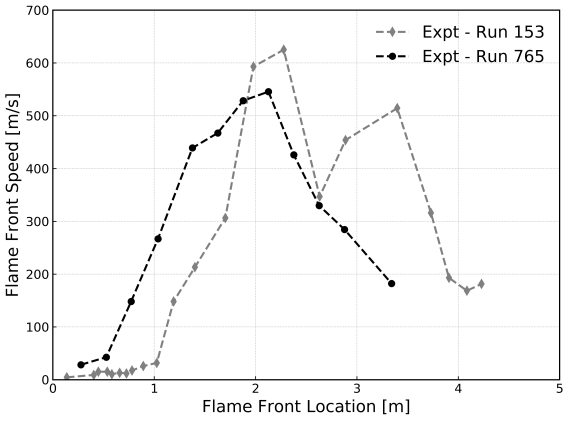

(b) Flame front speed vs. location

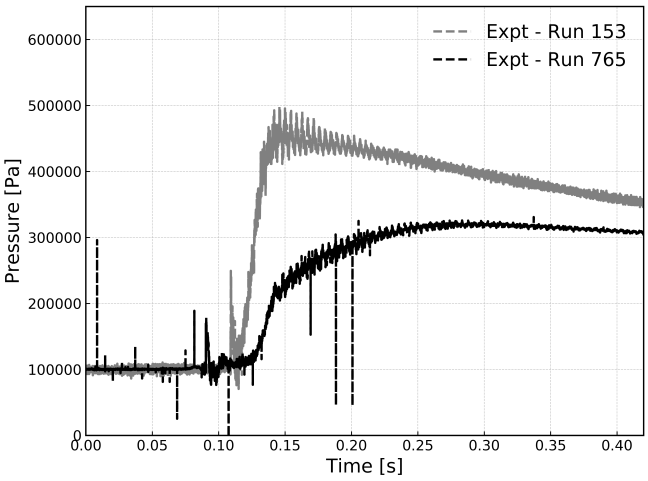

(c) Pressure evolution at the dome entrance

Figure 5.12: Flame propagation and pressure trends for RUN 153 and RUN 765.

Figure 5.12c shows the temporal evolution of pressure at the dome entrance for both experimental runs. During the initial and acceleration phases, pressure rise is negligible. However, as the flame accelerates and pressure waves detach and travel through the domain, a rapid increase in pressure is observed. These pressure waves reflect off the top of the dome and form expansion waves, which lead to the formation of intermediate pressure peaks and transient pressure drops.

After the flame enters the dome and combustion completes, the pressure reaches its maximum value. The pressure signal, especially after peak pressure is reached, exhibits oscillations due to wave reflections within the facility. These pressure oscillations may resonate with the natural frequencies of containment structures, raising concerns about potential structural loading.

Uncertainty in Experimental Flame Speed Measurements The experimental flame speed data presented in Figures 5.12a and 5.12b are derived from the temporal gradient of flame front positions obtained via photomultiplier sensors. This method inherently introduces uncertainty due to both spatial and temporal resolution limitations.

First, the flame front position is inferred from the time at which radical emissions (e.g., OH, CH) are detected at fixed axial locations. The spatial resolution is thus limited by the discrete sensor spacing - often several centimeters - which may lead to under or over estimation of actual flame progression, especially during phases of rapid acceleration or deceleration.

Second, the temporal derivative used to compute velocity amplifies any measurement noise or signal fluctuations. Given that the flame speed is obtained using finite difference approximations over

consecutive sensor times, small timing inaccuracies can propagate into significant velocity deviations, particularly near inflection points in the flame trajectory.

Furthermore, in stratified mixtures (e.g. RUN 765), the flame structure can be more complex and stretched, leading to multi - point flame arrival at individual sensors. This complicates the interpretation of arrival time and can introduce ambiguity in defining a single flame front location. Collectively, these factors highlight the importance of interpreting experimental flame speed trends with an understanding of the underlying data processing limitations.

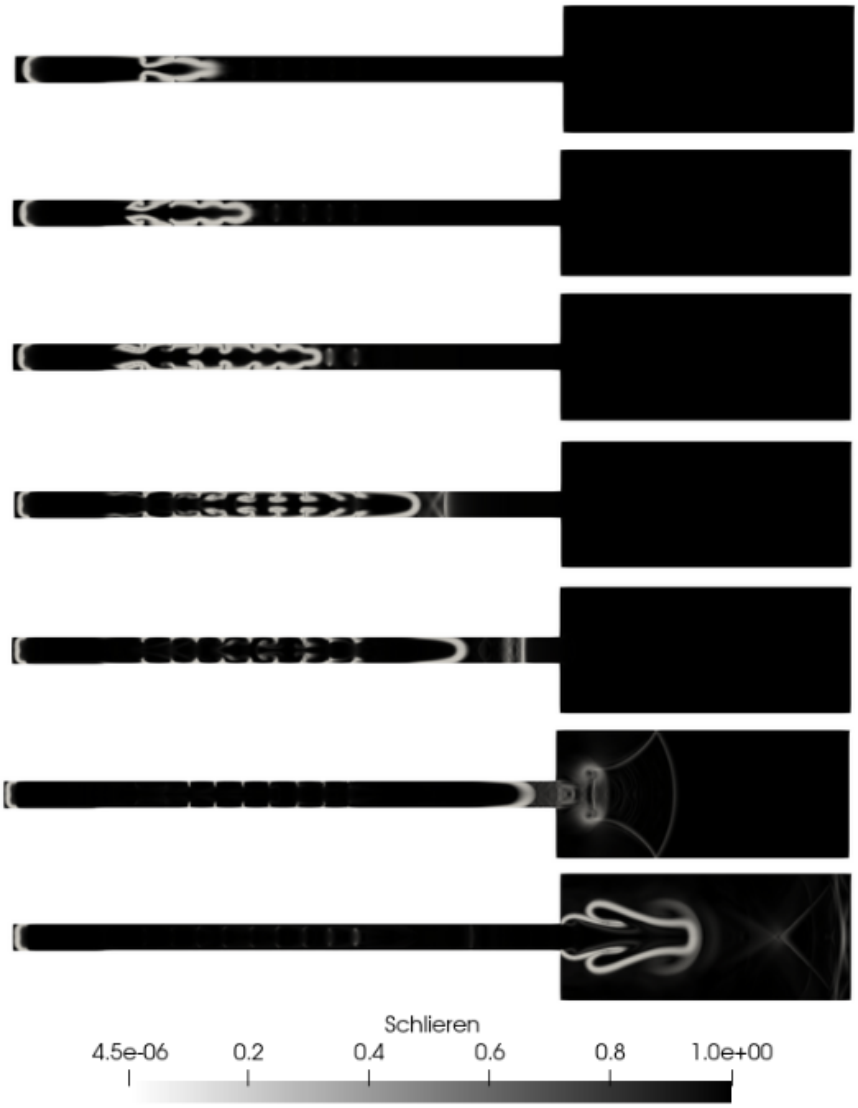

Figure 5.13: Schlieren visualization of flame evolution in ENACCEF (RUN 153). Frames show key stages: laminar propagation, turbulent flame wrinkling due to baffles, shock formation, and jet-like expansion in the dome.

- Flame propagation can be clearly divided into four physical regimes, with distinct effects on pressure and flow field development.
- Pressure evolution is highly sensitive to flame acceleration dynamics and the location of wave reflections.
- RUN 153 corresponds to a uniformly premixed mixture with 13 vol.% hydrogen, whereas RUN 765 features a negatively stratified hydrogen concentration profile ranging from 11.6 to 8.1 vol.%. Given that laminar flame speed increases with hydrogen concentration, it is expected for RUN

153 to exhibit a laminar flame speed higher than RUN 765 near the ignition location.

- Interestingly, during the quasi-laminar flame propagation phase, experimental observations indicate a higher flame velocity in RUN 765 compared to RUN 153, contrary to expectations based on mixture reactivity. However, in the subsequent turbulent flame acceleration phase, RUN 153 displays a more pronounced increase in flame speed, which aligns well with numerical predictions. The reason for the early-phase deviation observed in experiments remains unclear.
- The intermediate peak pressure observed during flame deceleration is higher in RUN 153, a direct consequence of its faster flame propagation and stronger pressure wave generation. This behavior is consistently captured in the experiments.
- Within the dome section, where the final combustion occurs, the hydrogen concentration in RUN 765 is reduced to 8.1 vol.%, while RUN 153 maintains 13 vol.%. This reduced reactivity in RUN 765 results in a lower adiabatic flame temperature and subsequently lower pressure. Consequently, the maximum mean pressure reached in RUN 765 is lower than that in RUN 153.

Figure 5.13 presents a Schlieren visualization from the simulation of RUN 153, capturing the evolution of flame and shock structures over time. The sequence of frames illustrates the transition from smooth laminar flame propagation to turbulent acceleration, and finally to dome-filling expansion. The flame initially propagates as a thin front in the acceleration tube, and strong flame wrinkling and shock formation are observed upon encountering the baffles. As the flame reaches the dome, it expands radially and generates complex wave interactions, consistent with the pressure oscillations seen in the measurements.

The experimental validation provided by RUN 153 and RUN 765 thus serves as a robust benchmark for understanding premixed hydrogen-air combustion under confinement and obstruction, with implications for safety in nuclear and process industries.

Mesh Independence Analysis

In RANS simulations, ensuring mesh independence is critical for the reliability and generality of the computed results. A solution that is significantly influenced by the underlying mesh cannot be considered physically meaningful. Therefore, a detailed mesh sensitivity analysis was conducted using RUN 153 as the benchmark case.

Three different mesh resolutions, ranging from the coarsest (denoted as M1) to the finest (M3), were tested to assess the effect of mesh refinement on key solution metrics. The objective of this study was to determine the minimum mesh resolution required to achieve grid-independent results, ensuring that any further refinement does not materially affect the predictions. In RANS modeling, achieving this level of accuracy must be balanced with computational efficiency. As such, the selected mesh must offer an optimal trade-off between solution accuracy and computational cost. The results of the mesh sensitivity study form the basis for mesh selection in subsequent simulations.

The chosen resolution is determined through a mesh sensitivity study to guarantee that key physical features are adequately captured without introducing grid-induced errors. This conservative approach provides a robust framework for evaluating combustion and pressure dynamics, particularly in geometries that feature fine-scale obstructions and require spatial consistency for accurate turbulence and flame model predictions.

Table 5.9: Mesh configurations and simulation run times used in the grid sensitivity study.

Mesh	Acceleration Tube	Dome	Total cells	Run time (s)
M1	660×15	340×74	35400	3109
M2	1320×30	680×148	141600	22203
M3	2640×60	1360×296	566400	207342

A detailed mesh sensitivity study was carried out for RUN 153 to assess the effect of spatial resolution on the flame propagation and pressure predictions. Three different uniform meshes- denoted M1, M2, and M3 were tested, corresponding to progressively finer cell counts (see Table 5.9). The objective was to identify a mesh configuration that balances computational cost with solution accuracy.

Figure 5.14a shows that increasing the mesh resolution improves agreement with experimental flame speeds and front location. The coarse mesh (M1) underpredicts flame velocity and fails to capture the sharp acceleration observed in experiments. Meshes M2 and M3 exhibit significantly improved results, with M3 showing marginal gains over M2. Notably, both M2 and M3 are able to capture the flame acceleration phase and subsequent deceleration with good fidelity.

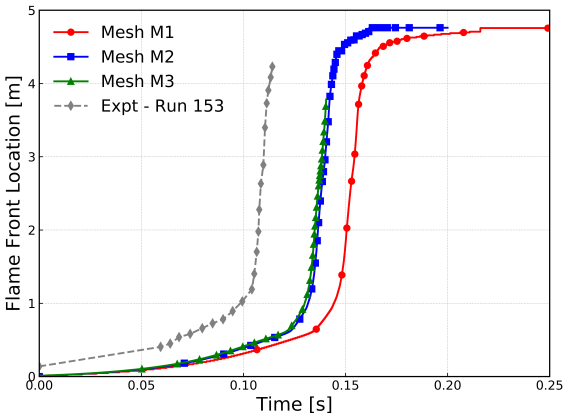

(a) Flame front location vs. time for different Mesh

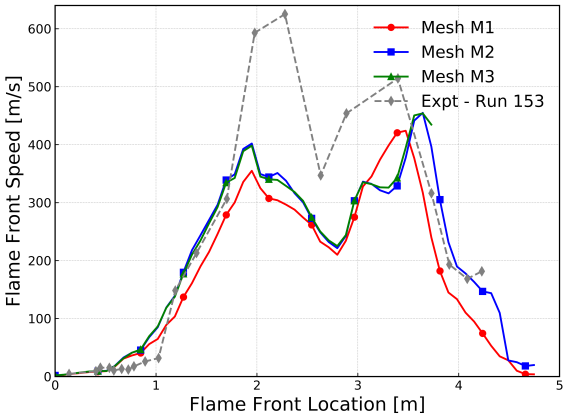

(b) Flame front speed vs. location for different Mesh

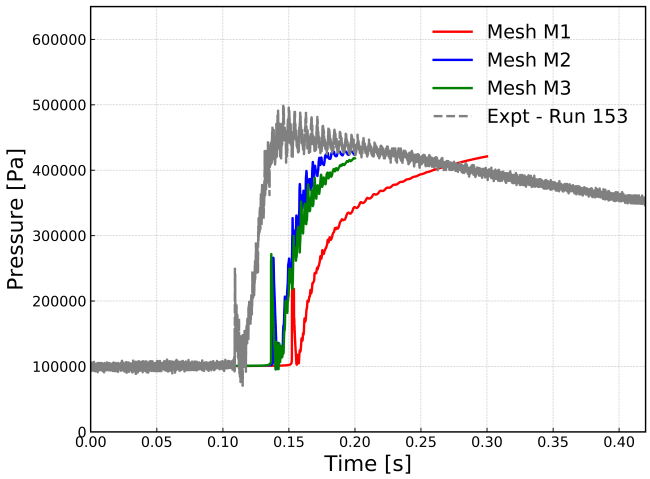

(c) Pressure evolution at the dome entrance for different Mesh

Figure 5.14: Mesh sensitivity study for RUN 153 using NRGXiFoam

From the pressure evolution in Figure 5.14c, it is observed that the peak pressure and pressure rise rate become increasingly accurate with mesh refinement. However, the improvement from M2 to M3 is minor, whereas the computational cost increases significantly (see Table 5.9). Based on this trade-off, mesh M2 was selected as the baseline mesh for all subsequent simulations, providing a reasonable compromise between numerical accuracy and computational efficiency.

A noticeable time shift between the experimental and numerical flame propagation is evident in Figures 5.14a and 5.14c. Specifically, the flame front in the experiments accelerates earlier than in the simulations. All simulations employed the buoyant k-ε turbulence model; however, the time lag is not due to the turbulence model formulation itself, but rather to the prescribed initial turbulence quantities. The initial values of k and ε influence the early evolution of flame-induced turbulence. If these values are underestimated, the model predicts insufficient turbulence intensity in the quasi-laminar regime, resulting in a delayed transition to flame acceleration. Consequently, the onset of shock formation and pressure wave propagation is also delayed relative to experimental observations.

Interestingly, an additional time shift is observed between the coarser mesh M1 and the finer mesh

M2, with the latter demonstrating an earlier flame acceleration. While both simulations adopt the same turbulence model and initial conditions, this difference can be traced to mesh-induced numerical effects. In coarse grids such as M1, spatial resolution is insufficient to capture the sharp gradients in flow quantities—particularly those that arise near the ignition zone and obstacle edges.

These observations reinforce the importance of adequate mesh resolution in capturing flame–turbulence interactions, especially in regions of strong flow gradients. The grid sensitivity study thus highlights not only the expected dependence of solution accuracy on mesh size, but also the nonlinear interplay between mesh resolution, turbulence modeling, and flame propagation dynamics in RANS-based simulations.

Additionally, the simulations assume adiabatic wall boundary conditions. This means no heat loss occurs through the vessel walls, in contrast to real experimental conditions where conductive and radiative heat losses reduce the energy retained within the system. As a result, the simulated pressure continues to rise even after flame arrival at the dome. The peak pressure is slightly underestimated compared to experiments. However, in the experimental setup, pressure gradually decays after peaking due to thermal losses, a behavior not captured by the adiabatic assumption, and hence, not seen in the simulations.

Despite these limitations, the model performs well in capturing the key dynamics of flame acceleration, pressure rise, and peak pressure timing -particularly with mesh M2, validating its use for further simulations.

Turbulence Model Analysis

To assess the influence of turbulence modeling on flame propagation, three two-equation RANS models were evaluated in conjunction with the Turbulent Flame Closure (TFC) model in the ENACCEF facility: the standard *k*–ε, the buoyant *k*–ε, and the standard *k*–ω model. Figure 5.15 presents the predicted flame front evolution and pressure response for each model, benchmarked against experimental data from RUN 153.

As seen in Figure 5.15a, all three models capture the general trend of flame acceleration through the baffled acceleration tube. However, minor differences arise in the timing and sharpness of the flame front evolution. The standard *k*–ω model exhibits a slightly delayed acceleration phase and underpredicts the flame speed across the domain. In contrast, the standard and buoyant *k*–ε models provide better agreement with experimental observations, particularly in the turbulent acceleration phase.

Although the flame speed predictions of the standard and buoyant *k*-ε models are nearly identical, their governing equations differ in one key aspect: the buoyant *k*-ε model includes explicit source terms for buoyancy-driven turbulence production. These terms are proportional to the gradient of density and gravitational acceleration, and allow the model to account for additional turbulence generation in flows where buoyancy is important.

This distinction becomes relevant in the early quasi-laminar phase, where flame propagation induces significant local temperature gradients in a nearly quiescent environment. While the turbulence intensity is initially low, the presence of buoyancy could accelerate the growth of flame-induced turbulence - an effect that the standard *k*-ε model does not explicitly capture. Despite this, the two models show similar results in the ENACCEF configuration. Importantly, however, buoyancy effects are not absent from the governing equations: both solvers include gravity terms in the momentum and energy equations.

It is important to emphasize that what is neglected here is not buoyancy, but the additional turbulence production due to buoyancy-driven instabilities and stratification. This distinction can be tested directly by artificially setting the gravitational acceleration $g = 0$ in the solver. Such a test reveals significant changes in the flame behavior and flame acceleration.

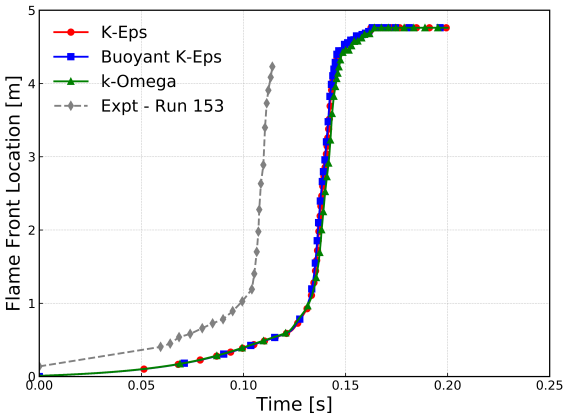

(a) Flame front location vs. time for different turbulence models

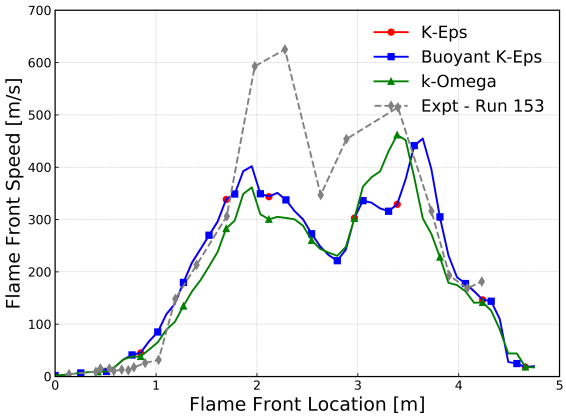

(b) Flame front speed vs. location for different turbulence models

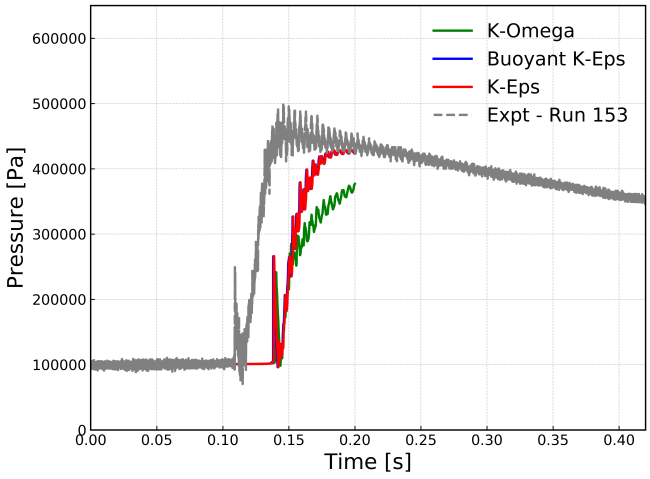

(c) Pressure evolution at the dome entrance for RUN 153 for different turbulence models

Figure 5.15: Turbulence sensitivity study for RUN 153 using NRGXiFoam

The pressure evolution at the dome entrance (Figure 5.15c) further reinforces the above observations. Both k–ε variants match the experimental pressure trends closely, capturing the onset and peak of pressure rise accurately. The k–ω model, on the other hand, underpredicts the magnitude of the pressure peak, reflecting its slower flame progression. The decay of pressure following the peak is not captured due to the assumption of adiabatic walls in the simulation, which neglects radiative and conductive heat losses observed in the physical system.

In light of these results, the buoyant k–ε model is selected for all subsequent simulations. While it shows only marginal improvement over the standard model in the ENACCEF case, its added physical realism and applicability to future configurations involving vertical propagation or significant stratification make it the preferred choice.

Validation for `ppNRGXiFoam`

Similar to the tests done with ENACCEF-2 using the Step0 experiments, it is essential to verify that the baseline behavior of the new solver `ppNRGXiFoam` matches that of the established `NRGXiFoam` implementation in the limiting case of a spatially uniform hydrogen–air mixture. This scenario corresponds to the `RUN 153` configuration of the ENACCEF experiments, and serves as a strict benchmark: since partial premixing is absent, both solvers should reproduce identical flame dynamics governed purely by the TFC combustion model.

Accordingly, the variance in the mixture fraction field was set to zero ($Z''^2 = 0$) and `solveZp = False`,

thus effectively recovering the behavior of a premixed configuration while leveraging the `ppNRGXiFoam` framework. The diluent-related fields and transport equations were also deactivated to maintain consistency with the experimental conditions of `RUN 153`.

The initial and boundary conditions, as well as numerical schemes and thermophysical models, were retained from the original configuration to ensure a direct comparison. In addition to the standard regress variable b, the mixture fraction $\widetilde{Z}$ was initialized to a constant value representing the equivalence ratio of the test case.

Figure 5.16 presents the flame front location, flame speed, and pressure evolution at the dome entrance, comparing both solvers with experimental data. As seen in the flame location and velocity plots, both solvers produce nearly identical flame propagation behavior, closely matching across the quasi-laminar, turbulent acceleration, and deceleration regimes. Importantly, both solvers predict the peak flame speed, acceleration zone, and flame slowdown with equivalent accuracy, confirming that `ppNRGXiFoam` correctly reduces to the expected behavior in the premixed limit.

The pressure plot further supports this consistency. Both solvers accurately capture the rapid pressure rise at the dome entrance associated with flame acceleration and entry. The magnitude and timing of the peak pressure, as well as the oscillatory behavior after dome entry, are consistent across the simulations and match experimental trends.`ppNRGXiFoam` exhibits a slightly delayed pressure rise compared to `NRGXiFoam`. Nevertheless, the peak pressure reached are consistent between both solvers and the experimental results.

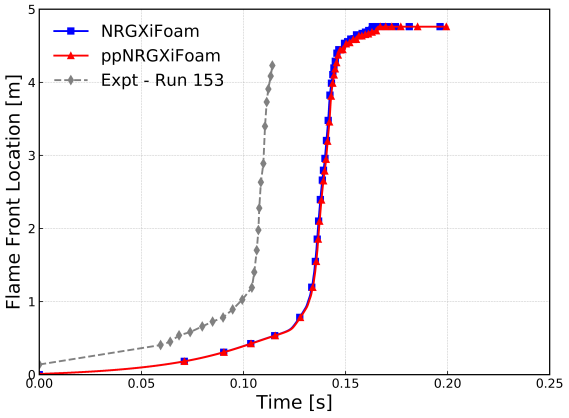

(a) Flame front location vs. time

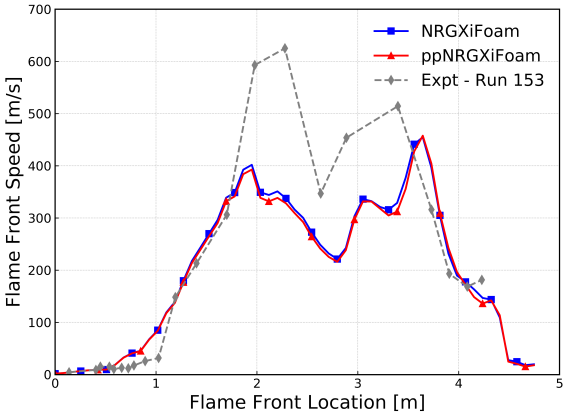

(b) Flame front velocity vs. location

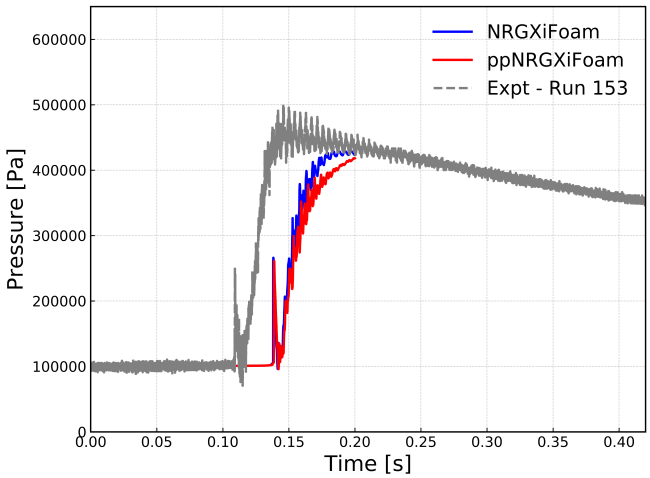

(c) Pressure evolution at the dome entrance

Figure 5.16: Validation of `ppNRGXiFoam` against `NRGXiFoam` for RUN 153.

Figure 5.17a presents the dynamic time step evolution during the simulation. Both solvers use identical Courant number limits, and the overall time-step trends are nearly indistinguishable. A zoomed view in Figure 5.17b reveals subtle differences during rapid transients - `ppNRGXiFoam` occasionally sustains marginally larger Δt during flame acceleration. These differences might stem from the additional scalar equations and source term couplings in the partially premixed formulation but have negligible effect on solution fidelity. This could explain the minor deviations in the results of Figure 5.16.

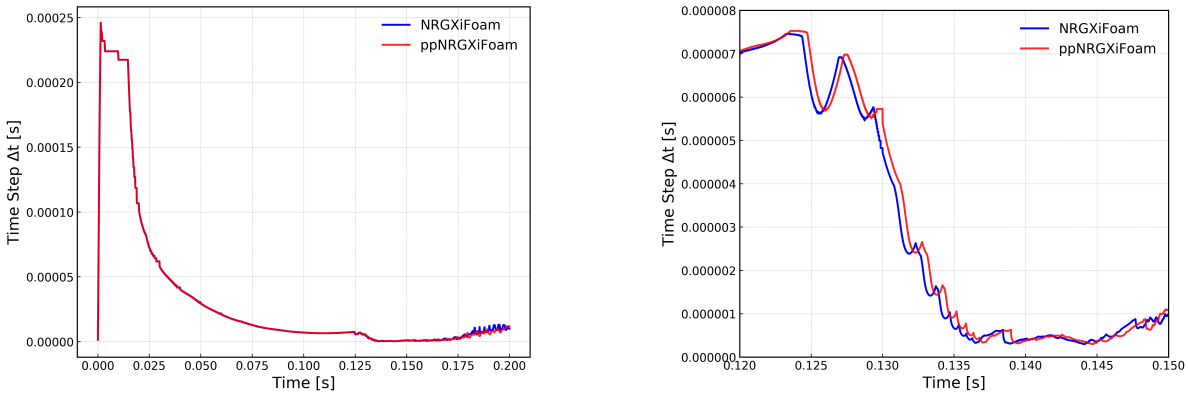

(a) Global Δt evolution

(b) Zoom near flame acceleration

Figure 5.17: Time step evolution for `NRGXiFoam` and `ppNRGXiFoam` during RUN 153.

This test confirms that `ppNRGXiFoam` faithfully reproduces the base solver behavior in the absence of premixing effects, and therefore serves as a robust foundation for further model extensions.

Validation of the Flame Speed Correlation Implementation

In the final step of the validation of ENACCEF using `RUN 153`, the focus shifts to evaluating the implementation and behavior of the newly incorporated flame speed correlation, similar to the tests performed on ENACCEF-2 under Step0 conditions. Two laminar flame speed models were compared using the `ppNRGXiFoam` solver: a constant flame speed model, and the Bentaïb flame speed library that dynamically computes S_L based on local pressure and temperature.

Given that the `RUN 153` involves a spatially uniform hydrogen-air mixture, the laminar flame speed should ideally remain constant throughout the simulation. This presents an ideal testbed for isolating numerical effects and verifying the flame speed correlation logic. In the first approach, the laminar flame speed is calculated at the initial thermodynamic conditions using the Bentaïb correlations in Cantera [70], and is held constant throughout the simulation. In the second approach, the same correlation is embedded into the OpenFOAM framework and used to dynamically evaluate S_L at each time step, incorporating corrections due to evolving pressure and temperature. This dynamic implementation corresponds to Bentaïb Approach 3 as defined in Equation (4.29).

Figure 5.18b and Figure 5.18a show the flame front speed and flame front location, respectively, as predicted by the two models against experimental results. It is evident that both models capture the overall flame acceleration and deceleration trends reasonably well, although slight differences are observed in the timing of key transitions, particularly during the early stages of propagation.

The delay observed in the flame front progression using the Bentaib model can be attributed to its internal formulation. Unlike the constant flame speed model, which assumes a fixed S_L throughout the domain, the Bentaib library applies dynamic corrections for both pressure and temperature at every computational step. During the quasi laminar propagation phase, the pressure and temperature gradients are still evolving. As highlighted in [34], this approach is suitable because pressure and temperature variations in thermodynamic states can significantly affect local flame speeds.

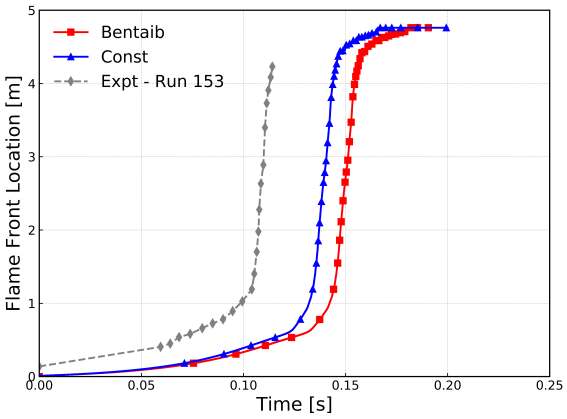

(a) Flame front location vs. time

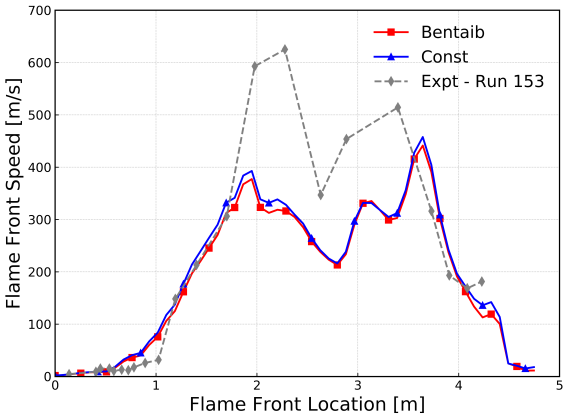

(b) Flame front velocity vs. location

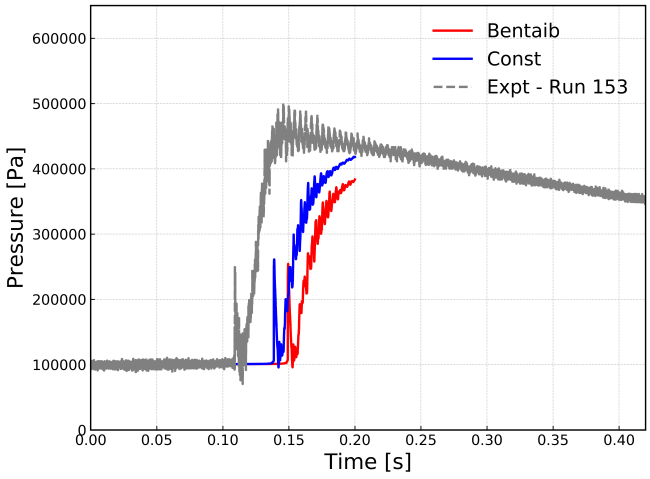

(c) Pressure evolution at the dome entrance

Figure 5.18: Comparison of Bentaib S_L model with Constant S_L Model

While this correction improves physical realism, it introduces slight numerical damping during the early flame development phase when pressure and temperature gradients are still evolving. Despite this, the agreement in flame front location and flame speed between the two models remains within acceptable bounds.

Overall, this comparison confirms that `ppNRGXiFoam` correctly recovers the limiting behaviour of the base solver for uniformly premixed mixtures. The successful reproduction of experimental trends and agreement with `NRGXiFoam` results establishes confidence in the new implementation. It serves as a prerequisite step before deploying `ppNRGXiFoam` on partially premixed test cases involving mixture fraction gradients and variance effects.

Final Remarks for RUN 153

The results obtained from RUN 153 provide a thorough validation of the modeling framework under spatially homogeneous conditions in the ENACCEF facility. This test case, featuring a uniformly premixed hydrogen - air mixture served as a direct analogue to the ENACCEF-2 Step0 case and allowed the following key evaluations to be performed:

- A comprehensive mesh sensitivity study established the minimum spatial resolution required to accurately capture flame acceleration and pressure dynamics, with mesh M2 identified as the optimal compromise between accuracy and computational cost. These mesh settings will be carried out for the next set of tests to be performed.

- The turbulence model analysis confirmed that the buoyant *k*-ε model performs reliably in this configuration. It was selected for use in all subsequent tests due to its physical realism and flexibility for future applications involving stratification.
- The new solver `ppNRGXiFoam` was benchmarked against `NRGXiFoam` and shown to reproduce identical behavior in the limit of zero mixture fraction variance. Flame front location, velocity, and pressure evolution matched well between the solvers and with experimental trends, validating the core consistency of the partially premixed formulation.
- The flame speed library was verified by comparing simulations with constant S_L and dynamically computed S_L from the Bentaïb correlation. Both models yielded comparable results, with the correlation based approach introducing minor temporal delay during early flame development, as expected. These results confirm the correctness of the new library implementation in OpenFOAM.

Collectively, these tests confirm that the solver and combustion models maintain accuracy and robustness across different geometries and facility conditions. The flame acceleration trends, shock formation timing, and peak pressure magnitudes are well captured, lending further confidence to the numerical framework.

With the solver now validated for spatially homogeneous mixtures, the next stage of the study focuses on the role of stratification. The upcoming analysis of RUN 765 - featuring a negatively graded hydrogen concentration profile, aims to assess the effect of mixture fraction variance on flame propagation. By enabling and disabling the Z''^2 term in the new flame speed model, the influence of stratification and turbulence - chemistry interaction will be systematically isolated. This transition represents a step forward in complexity, targeting more realistic accident scenarios involving compositional gradients.

5.2.5. Results - RUN 765

Among the various test campaigns conducted, `Run 765` is of particular interest for its negative hydrogen concentration gradient setup, intended to emulate realistic stratification scenarios in partially premixed environments. In this experiment, the acceleration tube was filled with a gradient mixture of hydrogen and air, ranging from approximately 11.6% molar H_2 near the ignition point to about 8.0% near the dome entrance, as verified by gas chromatography and summarized in Table 5.10. The dome itself was filled with a near-uniform mixture assumed to be 8.0% molar H_2. To achieve a fuel gradient inside the facility, an almost vacuum condition was created, after which hydrogen was injected at different concentrations for different times.

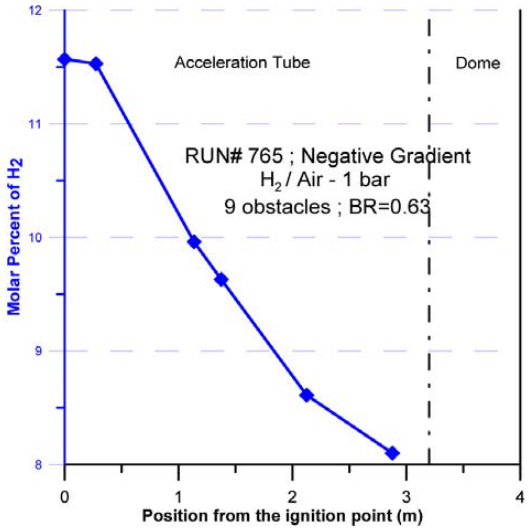

Figure 5.19: Test RUN765 hydrogen gradient-mean value along the tube [80]

This configuration promotes a fast combustion regime, critical for evaluating the performance of turbulent combustion models under non-uniform mixture conditions. Unlike uniform mixtures, gradient

configurations like Run 765 present additional challenges such as differential flame speeds, increased flame surface area, and potential local extinction or intensification effects due to triple flame formations.

As explained previously, the experimental results from Run 765 include detailed pressure and flame front velocity measurements along the tube and dome. These data serve as a benchmark for assessing the fidelity of CFD solvers in capturing the complex dynamics of partially premixed hydrogen-air flames. Accordingly, this test case is selected for further validation of the `ppNRGXiFoam` solver, which is specifically developed to extend the applicability of `NRGXiFoam` to non-uniform mixture conditions.

Table 5.10: Mean molar hydrogen fraction vs. distance from ignition point for Run 765

Position from ignition point (m)	Mean molar H_2 fraction
0.000	0.1160
0.277	0.1150
1.139	0.1000
1.377	0.0960
2.127	0.0860
2.877	0.0810
Dome (assumed)	0.0800

Overview of Simulations – RUN 765

Having established the predictive accuracy of the numerical framework under uniformly premixed conditions in RUN 153, the focus now shifts to a more complex and practically relevant scenario: hydrogen deflagration in the presence of a negative concentration gradient. `RUN 765` provides an ideal testbed to evaluate the solver's ability to handle spatially varying mixture fractions.

The following simulation plan is adopted to systematically analyze the solver behavior, validate the flame speed correlation model, and investigate the role of mixture fraction variance in partially premixed combustion:

1. Comparison with Uniform Mixture Case: A direct comparison between RUN 765 and RUN 153 is carried out to highlight the effect of negative stratification on flame dynamics. Given that flame speed increases with hydrogen concentration, differences in flame acceleration, shock formation, and pressure development are expected between the two cases.
2. Flame Speed Correlation Validation in Stratified Conditions: The Bentaïb flame speed library is re-evaluated in the context of a non-uniform mixture. Two configurations are tested using the `ppNRGXiFoam` solver:
   - Constant laminar flame speed based on initial thermodynamic conditions.
   - Dynamically varying laminar flame speed computed from the Bentaïb correlations, incorporating local pressure and temperature.

   In both cases, the mixture fraction variance term Z''^2 is set to zero and `solveZp = False`to isolate the influence of stratification alone.
3. Assessment of Mixture Fraction Variance via A Priori Comparison: A dedicated study is performed to replicate and build upon the a priori analysis by Sathiah et al. [35]. The goal is to quantify the potential influence of Z''^2 on flame speed predictions and to understand under what conditions variance effects become significant in stratified flows.
4. Parametric Study of Mixture Fraction Variance: A controlled parametric sweep is conducted by prescribing different profiles for Z''^2, while keeping the mean mixture fraction field fixed. This allows isolation of the impact of mixture fraction variance on flame propagation behavior.
5. Sensitivity Tests with Non-Zero Z''^2: Finally, the full simulation of RUN 765 is repeated with non-zero variance profiles informed by the parametric study. The goal is twofold:
   (a) To evaluate whether enabling Z''^2 improves agreement with experimental results.

(b) To determine if the trends observed in the parametric study are consistently reproduced when applied to the actual facility configuration.

This tiered analysis framework enables a progressive investigation of the role of stratification and mixture fraction variance in hydrogen combustion modeling. It ensures that the transition from uniform to inhomogeneous scenarios is grounded in validated methodology and clearly quantifiable physical mechanisms.

Comparison of RUN 153 and RUN 765

To assess the performance of `ppNRGXiFoam` under stratified conditions, simulations were performed for `RUN 765` and compared against the uniform mixture case of `RUN 153`. Both test cases were run using the same solver and turbulence-flame closure configuration. The constant laminar flame speed model was applied in both simulations(equation 4.17). In the stratified case, the hydrogen concentration gradient was initialized using OpenFOAM's `codeStream` functionality, and mixture fraction variance (Z''^2) was set to zero. This configuration allows for an isolated study of stratification effects without the added complexity of turbulence–chemistry interaction through mixture fraction variance.

Figure 5.20b compares the flame front velocity as a function of location for both `RUN 153` and `RUN 765`. As expected, `RUN 765` exhibits consistently lower flame speeds across the domain compared to the uniform mixture case of `RUN 153`. This difference stems from the reduced average hydrogen concentration and the presence of a negative concentration gradient in `RUN 765`, which in reality would lead to a spatially varying laminar flame speed.

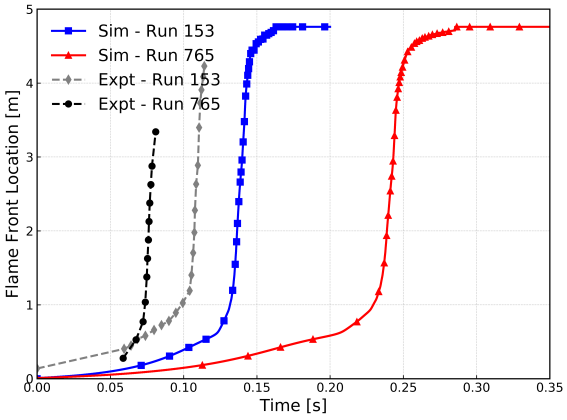

(a) Flame front location as a function of time for RUN 153 and RUN 765

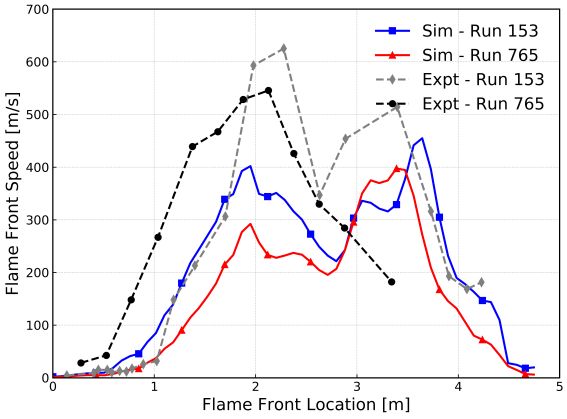

(b) Flame front speed vs. location for RUN 153 and RUN 765

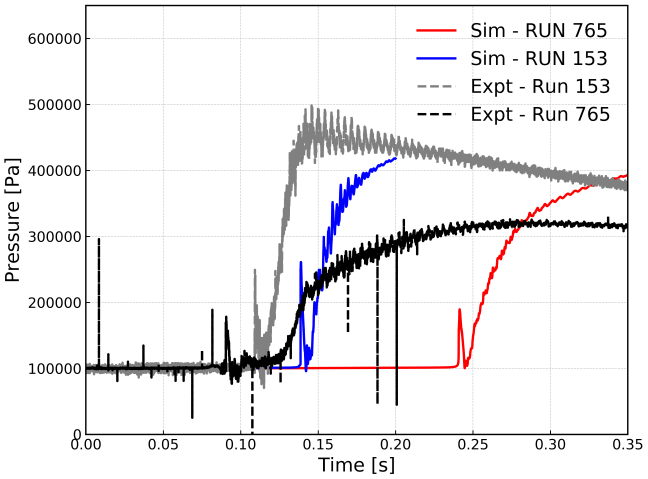

(c) Temporal evolution of pressure at the dome entrance for RUN 153 and RUN 765

Figure 5.20: Comparison of flame propagation and pressure dynamics between `RUN 153` and `RUN 765`

However, since a constant S_L model is used in this simulation, the direct influence of the reducing hydrogen concentration on laminar flame speed is not captured. As a result, while the overall difference in flame acceleration is still evident - particularly during the turbulent acceleration phase where `RUN 153` reaches a significantly higher peak speed, the flame speed profile in `RUN 765` may not fully reflect the expected physical behavior under stratified conditions.

The flame front position over time, shown in Figure 5.20a, confirms the delayed flame propagation in `RUN 765`. The flame in `RUN 153` accelerates more quickly, reaching the dome significantly earlier. This behavior is consistent with the higher reactivity of `RUN 153`, while the stratified mixture in `RUN 765` propagates more slowly due to a lower initial concentration at the time of ignition and increasing lean conditions along the tube.

Figure 5.20c presents the pressure evolution at the dome entrance. As expected, the pressure rise in `RUN 765` is delayed and more gradual than in `RUN 153`, reflecting the slower flame acceleration. Peak pressure in `RUN 765` is also slightly lower due to reduced heat release from leaner hydrogen concentrations. The simulations capture both the timing and relative magnitude of the pressure rise with reasonable fidelity. However, the absolute pressure peak in `RUN 765` is slightly overpredicted, potentially due of the constant S_L model in representing the reduced reactivity of the stratified mixture.

In summary, this comparison highlights the impact of hydrogen stratification on flame acceleration and pressure development. While the constant flame speed model offers useful qualitative insight, its inability to account for spatial changes in mixture composition limits quantitative agreement in the stratified case. The next section addresses this limitation by incorporating the dynamic flame speed correlation that accounts for local mixture fraction variations.

Validation of the Flame Speed Correlation Implementation

To improve the fidelity of flame propagation predictions in partially premixed hydrogen-air mixtures, the Bentaïb flame speed correlation was used using the Bentaib flame speed Library. This correlation dynamically computes the laminar flame speed S_L at each time step based on local pressure, temperature, and hydrogen concentration. In contrast, the fixed flame speed model assumes a constant S_L across the entire domain, calculated at the initial thermodynamic conditions. Both models were tested for `RUN 765`, which involves a negative hydrogen concentration gradient and is thus a prime candidate to assess the influence of spatially varying reactivity.

In Figure 5.21a, the flame front location vs. time shows a consistent delay in the Bentaïb model relative to the constant flame speed case. This behavior is expected. As the flame traverses a domain with declining hydrogen concentration, the dynamically computed S_L decreases, leading to slower local flame propagation rates and a delayed global flame front trajectory. Consequently, the flame requires more time to reach the dome, resulting in the observed rightward shift.

Figure 5.21b further illustrates this effect. The flame front velocity predicted by the Bentaïb model is consistently lower than that of the constant S_L model throughout the acceleration tube. Notably, the peak flame speed, typically associated with the turbulent flame acceleration regime is significantly reduced when using the Bentaïb correlation. This result highlights the model's sensitivity to local thermochemical state.

This trend also propagates into the pressure dynamics, shown in Figure 5.21c. The constant S_L model predicts an earlier and sharper pressure rise due to its faster flame acceleration. In contrast, the Bentaïb model exhibits a more gradual pressure increase, with a visibly lower peak and delayed onset. While this result reflects improved physical realism for non-uniform mixtures, it also reveals a key shortcoming: both models substantially under-predict the experimental pressure signal. Not only is the maximum pressure underestimated, but even the intermediate pre-peak pressure rise, referring to the presence of the pressure wave , is captured poorly.

This raises a critical modeling question: if the Bentaïb model accurately reflects the reduction in reactivity due to hydrogen depletion, what explains the significant gap in predicted versus measured flame speeds and pressure levels?

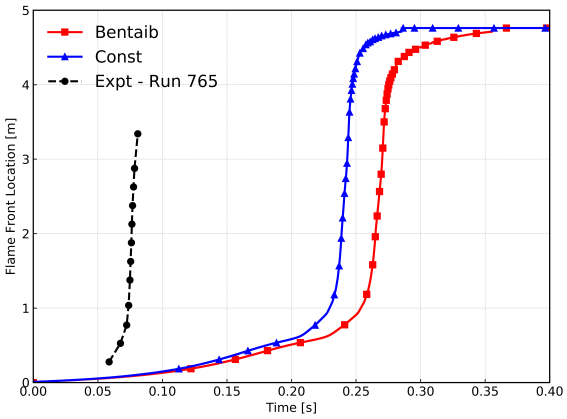

(a) Flame front location vs. time

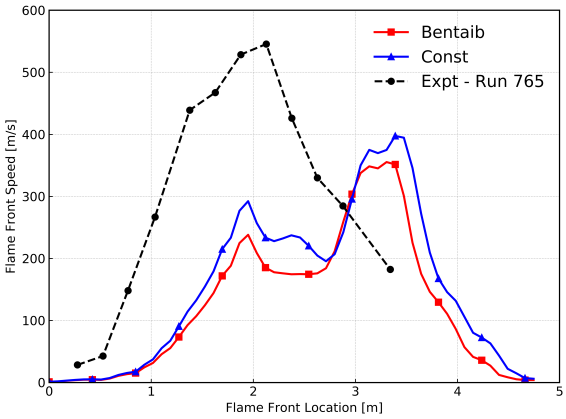

(b) Flame front velocity vs. location

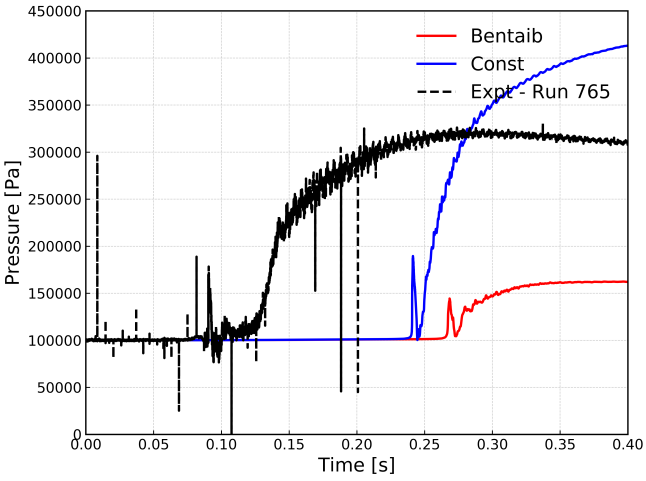

(c) Pressure evolution at the dome entrance

Figure 5.21: Comparison of Bentaïb flame speed correlation and constant S_L model for `RUN 765` using `ppNRGXiFoam`.

To answer this, we revisit the assumption made in this run - that the mixture fraction variance, Z''^2, is zero. As discussed in Chapter 3, the influence of mixture fraction fluctuations is expected to be more pronounced in stratified flows (see equation 3.29). The earlier study by Sathiah et al. [35] assumed these fluctuations to be negligible, based on an *a priori* mathematical analysis of the ENACCEF facility. However, the results that we have obtained now using these underlying assumptions warrants a re-examination of the analysis.

Given the consistent underprediction of both flame acceleration and pressure build-up, even when using dynamic flame speed correlations-it becomes increasingly clear that neglecting Z''^2 may be overly simplistic. Small-scale composition fluctuations can play a non-trivial role in enhancing local burning velocities, especially in turbulent, stratified regimes. This motivates the next section, where the *a priori* analysis is redone with updated simulation data to evaluate whether mixture fraction variance must be explicitly modeled for accurate predictions in partially premixed flames.

A Priori Analysis of Mixture Fraction Fluctuations

To investigate the effect of subgrid-scale mixture fraction fluctuations on flame propagation in stratified hydrogen-air mixtures, *a priori* analysis was conducted to quantify the influence of such fluctuations on both the laminar flame speed and the chemical source term in the progress variable transport equation.

The core motivation behind this analysis is to understand the assumption made by Sathiah et al. [35], where the influence of mixture fraction variance Z''^2 was considered negligible for ENACCEF-like configurations. In contrast, the present work seeks to re-evaluate this assumption by directly quantifying

how fluctuations in mixture fraction impact key combustion parameters, especially in partially premixed conditions.

The relative fluctuation is defined of mixture fraction $\tilde{Z}$ is defined as:

$$\epsilon_Z = \frac{Z - \tilde{Z}}{\tilde{Z}} = \frac{Z''}{\tilde{Z}}, \tag{5.2}$$

where Z'' denotes the fluctuating component.

In the context of flame speed, the relative fluctuation in S_L due to mixture fraction perturbation is defined as:

$$\epsilon_{S_L} = \frac{S_L(Z)^{1/2} - S_L(\tilde{Z})^{1/2}}{S_L(\tilde{Z})^{1/2}} \tag{5.3}$$

The source term ω in the progress variable transport equation (equation 3.20 is directly proportional to:

$$\omega(Z) \propto \rho_u(Z) S_L(Z)^{0.5} \kappa_u(Z)^{-0.25} \tag{5.4}$$

Similarly, the corresponding fluctuation in the source term ω is given by:

$$\epsilon_\omega = \frac{\omega(Z) - \omega(\tilde{Z})}{\omega(\tilde{Z})} \tag{5.5}$$

These expressions quantify the sensitivity of the laminar flame speed and the chemical source term to perturbations in the mixture fraction field. To evaluate them, a 6$^{\text{th}}$-order polynomial fit was constructed for $S_L(Z)$, using laminar flame speed data computed from Liu-Macfarlane correlations [73]. Additional thermo-physical properties (ρ_u, α_u) were evaluated using the Cantera [70] library.

Using the polynomial fits, a second-order Taylor expansion was employed to model the effect of fluctuations:

$$S_L(Z) \approx S_L(\tilde{Z}) + Z'' \frac{dS_L}{dZ} + \frac{(Z'')^2}{2} \frac{d^2 S_L}{dZ^2} \tag{5.6}$$

where the derivatives were evaluated analytically from the polynomial coefficients. Similar expansions were applied to compute $\omega(Z)$.

Figure 5.22 shows the variation of the relative fluctuation in flame speed ϵ_{S_L} with respect to the relative fluctuation in mixture fraction ϵ_Z for different values of the mean mixture fraction $\tilde{Z}$. Two sets of results are shown: one based on exact calculations using the full expressions, and the other based on second-order Taylor series approximations.

As seen in Figure 5.22, the flame speed is significantly sensitive to fluctuations in Z, particularly in leaner mixtures (lower $\tilde{Z}$). For example, at $\tilde{Z} = 0.0063$, even a 10% fluctuation in mixture fraction can lead to a 15–20% deviation in S_L, underscoring the non-negligible influence of local composition inhomogeneities on burning velocity.

The implications are also prominent when analyzing the chemical source term ω, shown in Figure 5.23.

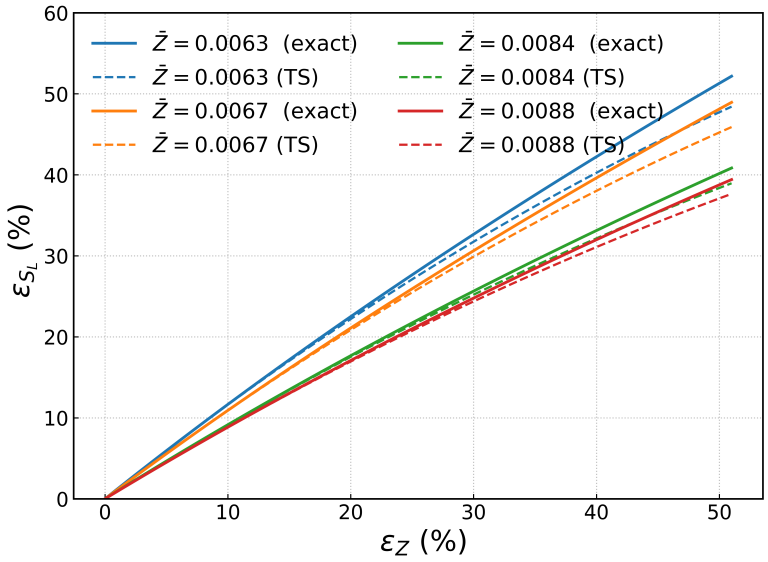

Figure 5.22: Relative fluctuation in laminar flame speed (ϵ_{S_L}) as a function of relative mixture fraction fluctuation (ϵ_Z) for different mean values $\tilde{Z}$. Solid lines indicate exact values; dashed lines denote Taylor series approximations.

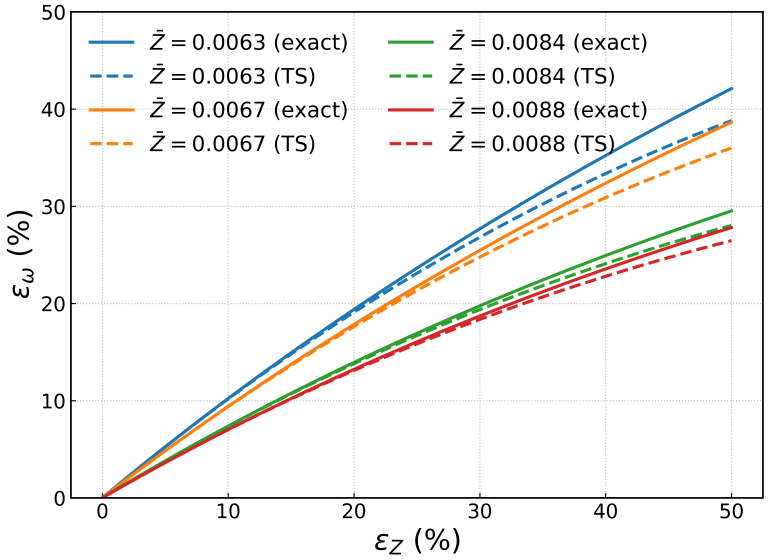

Figure 5.23: Relative fluctuation in source term ϵ_ω as a function of mixture fraction fluctuation ϵ_Z.

The source term $\dot{\omega}_c$ shows somewhat a nonlinear sensitivity to mixture fraction perturbations. For lower $\tilde{Z}$, the source term can deviate by almost 20% for $\epsilon_Z = 20\%$. This directly challenges the prior assumption that mixture fraction variance can be neglected, especially in simulations involving stratified or inhomogeneous configurations.

These findings reinforce the need to retain the Z''^2 term in modeling the turbulent flame speed in partially premixed hydrogen deflagrations. The steep gradients in local reactivity and thermochemical properties observed here play a critical role in determining flame acceleration, pressure buildup, and ultimately, the overall severity of the combustion event.

The *a priori* analysis clearly demonstrates that:

- Mixture fraction fluctuations have a pronounced impact on both laminar flame speed and the chemical source term.

- These effects are more pronounced at lower values of mean mixture fraction $\tilde{Z}$.
- The earlier claim that Z''^2 can be neglected [35] does not hold under the conditions considered in this work.

This justifies the inclusion of mixture fraction variance in the partially premixed flame model and sets the stage for the sensitivity analyses conducted in the next section.

Parameter Sweep Analysis of Mixture Fraction Variance

Having established through a priori analysis that fluctuations in mixture fraction can significantly impact the laminar flame speed and source term behavior, the next logical step is to explore how this effect manifests across a broader parametric space. In particular, we aim to quantify the impact of increasing mixture fraction variance on the integrated flame speed $\tilde{S}_L$, especially for lean mixtures that are near the flammability limit. This section details a parameter sweep over several representative mean mixture fractions $\tilde{Z}$, taken from the ENACCEF experimental dataset, and evaluates how variance shifts the effective flame speed.

As discussed earlier, when a scalar such as the laminar flame speed S_L is a nonlinear function of the local mixture fraction $\tilde{Z}$, any fluctuations in Z will affect the spatial average of S_L non-trivially. Instead of simply evaluating $S_L(\tilde{Z})$, the correct approach involves integrating the local property over the full probability distribution of Z, typically represented by a Beta distribution.

The integrated flame speed is computed as (refer to complete equation 4.30):

$$\tilde{S}_L = \int_0^1 S_L(\tilde{Z}) \cdot P(\tilde{Z}, Z''^2)\, dZ \tag{5.7}$$

where $P(\tilde{Z}, Z''^2)$ is the normalized Beta PDF parameterized by the mean $\tilde{Z}$ and variance Z''^2. The Beta PDF used is computed using the following parameterization:

$$a = \tilde{Z}\left(\frac{\tilde{Z}(1-\tilde{Z})}{Z''^2} - 1\right), \quad b = (1-\tilde{Z})\left(\frac{\tilde{Z}(1-\tilde{Z})}{Z''^2} - 1\right) \tag{5.8}$$

which satisfies the condition for a valid PDF as long as $Z''^2 < \tilde{Z}(1-\tilde{Z})$.

The flame speed $S_L(\tilde{Z})$ is obtained using a blended empirical correlation between the LMF and Bentaïb models (equation 4.24). The integral in Equation (5.7) is evaluated numerically using Gaussian quadrature in Python.

The Beta PDF and flame speed integrand $S_L(\tilde{Z}) \cdot P(\tilde{Z})$ were constructed across a fine $\tilde{Z}$-grid, and the integration was performed using the `quad` function in Python from `scipy.integrate`. The Python code snippet uses an internally consistent approach for gamma-function evaluation (via a log-gamma hybrid) and handles very small $\tilde{Z}$ and $\tilde{Z}''^2$ values to maintain numerical stability.

To assess the deviation due to variance, we compute the relative increase in integrated flame speed over the baseline (no variance) case, similar to equation 5.3:

$$\epsilon_{S_L} = \frac{\tilde{S}_L^{1/2} - S_L(\tilde{Z})^{1/2}}{S_L(\tilde{Z})^{1/2}}. \tag{5.9}$$

Figures 5.24 and 5.25 show the integrand evaluation and Beta PDF for $\tilde{Z} = 0.008946$, a lean condition that refers to the initial concentration of `RUN 765`. In this case, the base laminar flame speed evaluated at the mean, $S_L(\tilde{Z})$, is approximately $0.18\,\mathrm{m/s}$. However, the integrated flame speed rises to $0.21\,\mathrm{m/s}$ for $\tilde{Z}''^2 = 0.001\tilde{Z}$ and to $0.31\,\mathrm{m/s}$ for $\tilde{Z}''^2 = 0.005\tilde{Z}$.

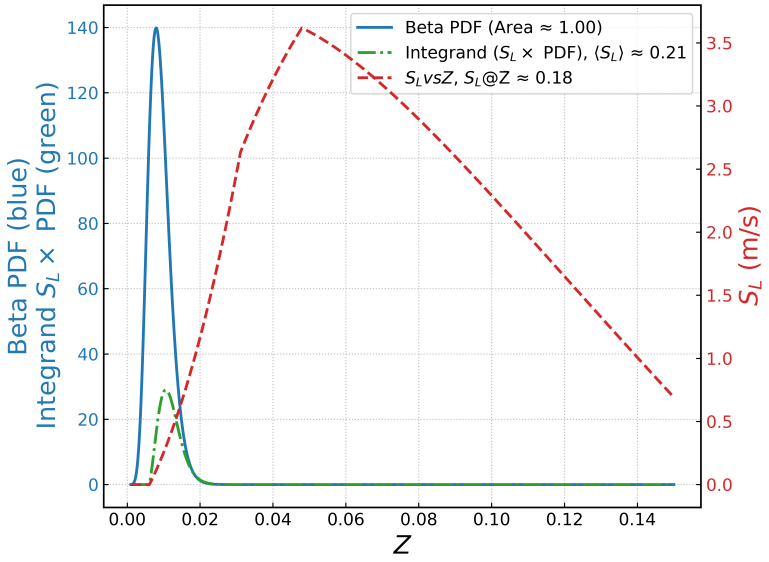

Figure 5.24: Overlay of Beta PDF, flame speed $S_L(\tilde{Z})$, and the integrand $S_L \cdot$ PDF for $\tilde{Z} = 0.008946$, $\tilde{Z}''^2 = 0.1\%\tilde{Z}$. The integrated flame speed $\tilde{S}_L \approx 0.21$ while $S_L(\tilde{Z}) \approx 0.18$.

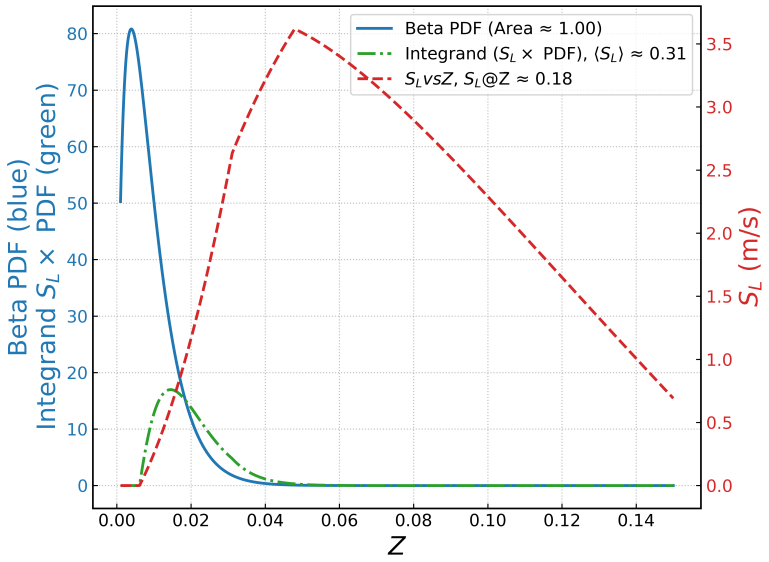

Figure 5.25: Effect of increasing variance to $\tilde{Z}''^2 = 0.5\%\tilde{Z}$ for same $\tilde{Z} = 0.008946$. Integrated flame speed increases further to $\tilde{S}_L \approx 0.31$, nearly 70% higher than the base case.

At very lean conditions ($\tilde{Z} = 0.008946$), most of the Beta PDF lies in regions where the flame speed is close to zero. However, as the variance increases, parts of the PDF shift into more reactive zones near the flammability threshold. The product $S_L \times$ PDF (shown as the green curve) exhibits a pronounced peak in this "shoulder region." This effect leads to a substantial increase in the integrated flame speed, with the case of $Z''^2 = 0.5\%\tilde{Z}$ showing over 70% amplification compared to the baseline.

This behavior explains a key modeling discrepancy observed in the earlier sections. When simulations were conducted using zero variance (as in the constant S_L or mean-based Bentaïb model), the predicted flame speeds and pressures in stratified mixtures like RUN 765 were severely underpredicted. However, the analysis presented here confirms that variance-induced enhancement of S_L is non-negligible - even at sub-percent levels of variance. These findings directly counter the assumptions made in prior studies such as Sathiah et al. [35], which suggested the effect could be ignored for

the ENACCEF facility.

Figure 5.26 presents the relative flame speed fluctuation ϵ_{S_L} as a function of mixture fraction fluctuation ϵ_Z for three representative mean mixture fractions $\tilde{Z}$.

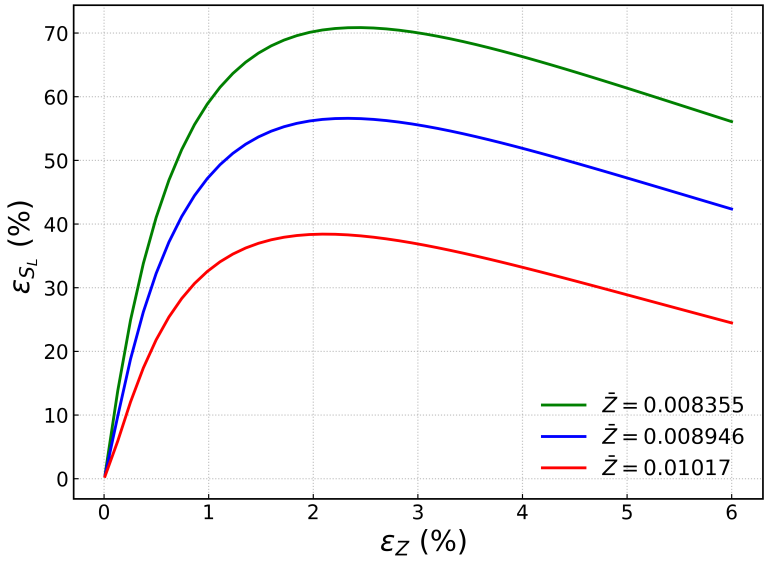

Figure 5.26: Relative flame speed fluctuation ϵ_{S_L} as a function of mixture fraction fluctuation ϵ_Z for selected $\tilde{Z}$ values.

The response of ϵ_{S_L} to increasing ϵ_Z is distinctly non-monotonic. Even at sub-percent variance levels, a clear enhancement in the effective laminar flame speed is observed, particularly for lower $\tilde{Z}$ cases. This is because, at very lean mean conditions, the Beta PDF is concentrated predominantly in the non-flammable region, where $S_L \approx 0$. The introduction of a small variance shifts a fraction of the distribution into more reactive zones, producing a disproportionately large increase in the integrated flame speed.

The effect is most pronounced for the smallest $\tilde{Z}$ considered ($\tilde{Z} = 0.008355$), where the relative increase exceeds 70% at moderate variances. As $\tilde{Z}$ increases, the baseline mixture is already in a more reactive regime, so the variance-induced enhancement is less dramatic.

At higher variances, the trend reverses due to a systematic leftward shift of the Beta PDF. As Z''^2 increases, the distribution becomes increasingly skewed towards the ultra-lean side of the mixture spectrum. Beyond a certain variance level, this shift is so pronounced that in the regions where $S_L > 0$, the Beta PDF attains values close to zero. Consequently, these reactive regions contribute negligibly to the integral in Equation 5.7, and the effective integrated flame speed begins to decline. This mechanism explains the post-peak reduction observed in ϵ_{S_L} and underscores the sensitivity of partially premixed flame dynamics to both the shape and position of the mixture fraction PDF.

This analysis highlights two critical points: (i) even small mixture fraction variances can substantially alter flame propagation in lean mixtures, and (ii) there exists an optimal variance range beyond which the enhancement effect saturates or diminishes. Such variance effects must therefore be explicitly considered in predictive modeling of partially premixed hydrogen-air combustion.

RUN 765 - Sensitivity Analysis of Mixture Fraction Variance

Before presenting the results, it is important to outline two modelling considerations that influence the interpretation of this sensitivity study.First, determining an appropriate initial value for the mixture fraction variance is inherently challenging. According to the governing transport equation for Z''^2 (see Equation 3.29), its evolution depends on the initial turbulence quantities k and ϵ. Since these quantities were not measured in the RUN 765 experiments, the initial variance cannot be prescribed *a priori* with confidence. This uncertainty motivates the present parameter sweep, in which a range of physically plausible initial variance levels is explored.

Second, in the current solver configuration, the transport equation for the mixture fraction variance is not solved. Instead, a non-zero initial Z''^2 is imposed uniformly in the domain and held constant throughout the simulation. This approach was adopted due to outstanding stability issues in the variance transport implementation, which could not be resolved within the timeframe of this work. While this simplification removes the effects of spatial and temporal variance transport, it enables a controlled assessment of the initial Z''^2 value on the predicted flame dynamics. In essence, ($Z''^2 > 0$) and `solveZp = False`.

With these considerations in mind, a sensitivity study was conducted by varying the imposed Z''^2 from 0 to 10% of the mean mixture fraction $\tilde{Z}$. The results are shown in Fig. 5.27, which presents the flame-front location histories, corresponding velocity profiles, and the pressure evolution at the dome entrance for each case, alongside the experimental data.

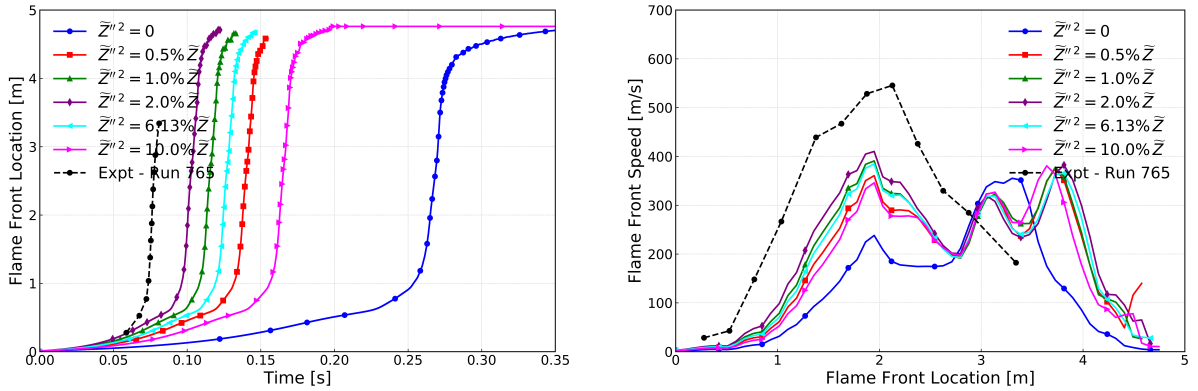

(a) Flame front location vs. time

(b) Flame front velocity vs. location

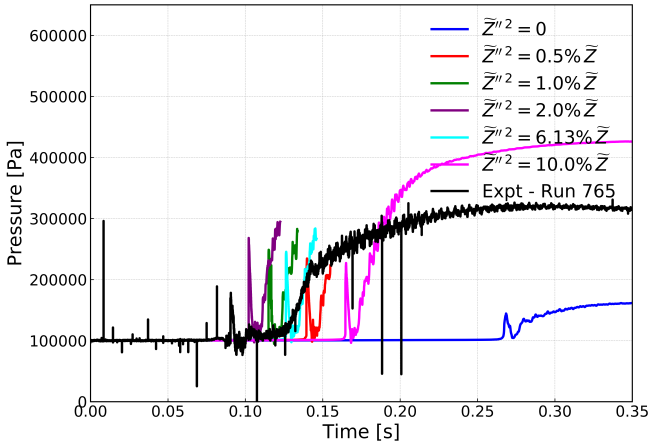

(c) Pressure evolution at the dome entrance

Figure 5.27: Sensitivity of flame propagation and pressure evolution in RUN 765 to initial mixture fraction variance. Experimental data is shown for comparison

Figure 5.27a shows the temporal evolution of the flame front position, while Figure 5.27b presents the corresponding flame front velocity profiles for different imposed values of Z''^2. As expected, increasing the initial mixture fraction variance enhances flame propagation by promoting local fluctuations in fuel concentration and increasing the effective burning rate. In the flame front velocity profile (Fig. 5.27b), the most pronounced influence of variance manifests in the *turbulent acceleration region*, extending from approximately $x \approx 1.0$ to $x \approx 2.5$ m. Here, modest increases in Z''^2 (e.g. 0.5%–2.0% of $\tilde{Z}$) substantially enhance the peak velocities, with $Z''^2 = 2.0\%$ producing the maximum acceleration amplitude. This behaviour is consistent with the a priori analysis of the beta-PDF for $\tilde{Z}$ (figures 5.24,5.25), which showed that small variances redistribute probability mass into locally richer regions, increasing the fraction of the mixture that lies above the flammability threshold and thereby elevating the effective laminar flame speed. Since `RUN 765` operates near the lean flammability limit, this activation is particularly

potent in this acceleration phase.

The pressure evolution (Fig. 5.27c) reinforce this interpretation. The onset and rate of pressure rise are strongly sensitive to $\widetilde{Z}''^2$ in the turbulent acceleration zone, with larger variances producing earlier onset of the pressure wave and steeper pressure ramps. Beyond the turbulent acceleration zone and approaching the dome (approximately $x > 3.0\,\mathrm{m}$), the velocity profiles for all variance levels tend to converge, and the pressure curves exhibit similar asymptotic behaviour. This convergence reflects the fact that the dome mixture composition is fixed and uniform across cases; thus, the upstream variance no longer plays a role in determining the local laminar flame speed and burning rate, and the jet flame expansion continues.

The non-monotonic response of the flame velocity to variance, previously demonstrated in the priori analysis, is clearly seen here. For small to moderate variances, the beta-PDF shape change favours reactive mass fraction growth; for large variances,a substantial portion of the PDF now resides in regions where the laminar flame speed is effectively zero (below the flammability threshold). Consequently, the probability mass contributing to active combustion diminishes, and the integrated flame speed decreases. This non-monotonicity is also reflected in the pressure evolution. The onset of the intermediate pressure rise, associated with the initial pressure wave generated in the turbulent acceleration region, shifts noticeably with variance. Moderate variances advance the timing of this shock formation and increase the magnitude of the intermediate pressure plateau, and as the the variance increases further, the magnitude of the intermediate pressure rise decreases, a result that directly correlates with decrease in laminar flame speed.

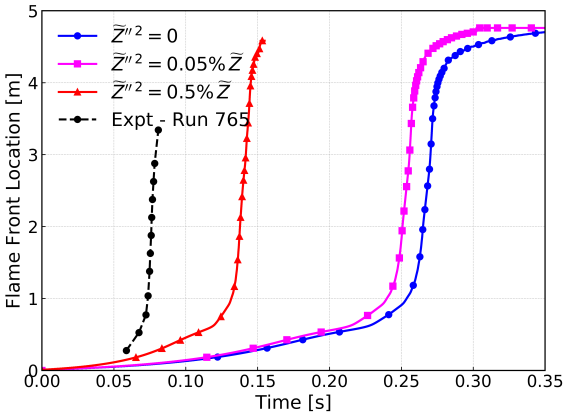

(a) Flame front location vs. time

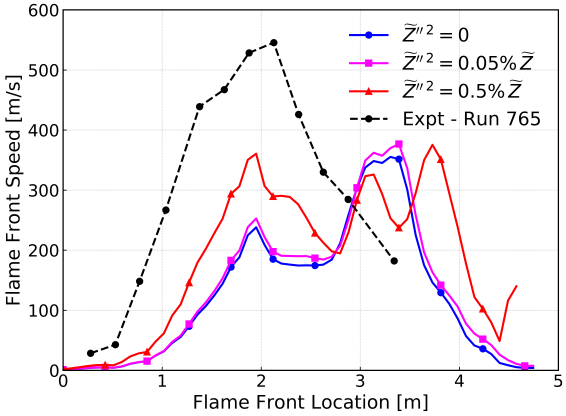

(b) Flame front velocity vs. location

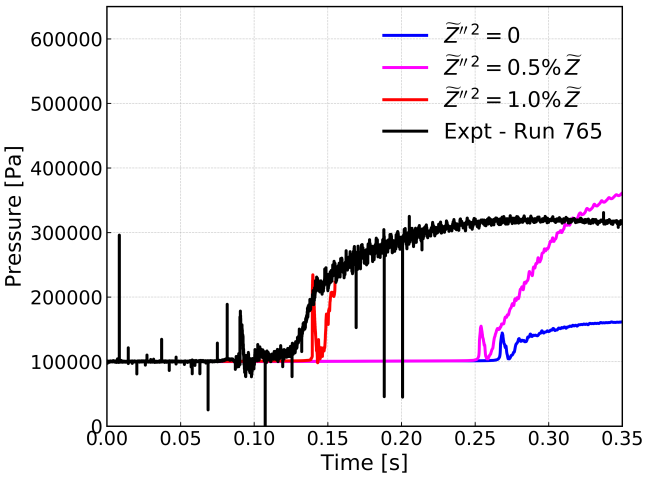

(c) Pressure evolution at the dome entrance

Figure 5.28: Sensitivity of flame propagation and pressure evolution in RUN 765 to initial mixture fraction variance. Experimental data is shown for comparison

As part of the sensitivity analysis, simulations were performed with the mixture fraction variance Z''^2 progressively reduced towards zero to assess the limiting behavior of the flame speed library. This edge case serves as an important consistency check to ensure that the implementation of the integration in the Bentaïb flame speed correlation behaves correctly under extreme conditions.

Figures 5.28a and 5.28b illustrate the flame front position and velocity for $Z''^2 = 0$ and a small but finite variance ($Z''^2 = 0.05\%$ of Z). As the mixture fraction variance decreases, the simulation results converge smoothly towards the zero-variance solution. This behavior demonstrates that the flame speed library correctly transitions to the limiting case where subgrid-scale composition fluctuations are absent.

As expected, the simulation with $Z''^2 = 0$ exhibits the slowest flame propagation, underpredicting both flame acceleration and peak velocities relative to experimental observations. In contrast, even a small finite variance ($Z''^2 = 0.5\%$ of Z) enhances flame propagation significantly, reflecting the sensitivity of flame dynamics to mixture fraction fluctuations in partially premixed systems.The corresponding pressure evolution (Fig. 5.28c) show a similar trend: the zero-variance case produces the latest onset and lowest magnitude of the pressure rise, while small finite variances advance the pressure wave formation and increase its peak, in closer agreement with experimental timing. This confirms that mixture fraction fluctuations not only accelerate the flame front but also strengthen the associated pressure transients.

This edge case validates the numerical implementation of the flame speed library by confirming that it correctly handles the zero-variance limit. The results further highlight the inadequacy of neglecting mixture fraction variance in predictive simulations and reinforce the importance of incorporating this parameter for accurate modeling of hydrogen deflagrations in containment scenarios.

Overall, this sensitivity study highlights the critical role of mixture fraction variance in accurately capturing flame propagation in partially premixed hydrogen-air mixtures. The results emphasize the need for careful consideration of this parameter in predictive simulations, especially in safety-critical applications.

Final Remarks for RUN 765

The RUN 765 simulations have demonstrated the clear influence of mixture fraction variance ($\widetilde{Z''^2}$) on flame propagation and pressure evolution in stratified hydrogen-air mixtures. The parameter sweeps confirm that even modest initial variances can significantly enhance the burning rate in the turbulent acceleration phase, primarily by increasing the probability of locally richer pockets above the flammability threshold. This effect is particularly relevant for RUN 765, where the mean mixture lies close to the lean limit and plays a decisive role in accelerating the flame front and generating the observed pressure transients.

While prescribing a fixed initial $\widetilde{Z''^2}$ has enabled a controlled investigation of its parametric influence, this approach inherently limits physical realism. In reality, $\widetilde{Z''^2}$ is not constant: its evolution is coupled to the turbulence field through the transport equation (Equation 3.29), with production driven by mean scalar gradients and dissipation linked to the turbulence dissipation rate ϵ. During the turbulent acceleration phase of RUN 765, the turbulence quantities k and ϵ undergo significant growth. If the variance transport equation were solved, this would be expected to increase $\widetilde{Z''^2}$ dynamically in the acceleration region, thereby amplifying the contribution at exactly the phase where the current model underpredicts experimental flame speeds and pressure rise rates. Such a dynamic treatment of variance is likely to improve agreement with the measured acceleration trends, both in terms of flame kinematics and the intermediate overpressure peak.

The present results also underscore the non-monotonic dependence of burning rate and pressure response on $\widetilde{Z''^2}$: while small to moderate variances accelerate the flame and strengthen the pressure wave, excessive variance shifts the beta-PDF towards ultra-lean values, reducing the reactive fraction and diminishing overall burning intensity. This behaviour was predicted by the a priori beta-PDF analysis and is now confirmed in the simulations.

Finally, the comparative analysis between experimental and numerical data suggests that the largest

discrepancies occur in the initial onset and slope of the turbulent acceleration phase. These differences can be attributed to the simplified treatment of mixture fraction variance and the absence of variance transport. Incorporating the full $\widetilde{Z''^2}$ transport equation, along with improved turbulence–chemistry closure models that respond to evolving turbulence scales, represents a promising avenue for further enhancing predictive fidelity under stratified, accident-relevant conditions.

In summary, the RUN 765 study validates the extended solver's capability to capture the primary effects of mixture stratification on hydrogen deflagration, highlights the sensitivity of results to $\widetilde{Z''^2}$ specification, and identifies variance transport modelling as a critical next step for improving quantitative agreement with experimental observations in the turbulent acceleration regime.

6

Conclusion and Recommendations

This thesis has presented the development, implementation, and validation of an extended CFD framework for modelling hydrogen–air combustion under accident-relevant, partially premixed conditions. The work combined the integration of new laminar flame speed correlations derived by Bentaïb with a pressure-based solver in `OpenFOAM`, capable of treating both premixed and non-premixed regimes. Numerical investigations were performed using experimental configurations from the ENACCEF facility, with emphasis on the role of mixture fraction variance in stratified hydrogen-air mixtures. The conclusions of this work, organised by the research questions posed in Chapter 1, are as follows:

- **Range of applicability and numerical stability of a pressure-based solver under accident-relevant conditions**

The applicability and robustness of the pressure-based solver were first assessed using the Sod shock tube problem across subsonic and supersonic regimes. In the subsonic case, `XiFoam` reproduced the analytical solution with excellent agreement, accurately resolving the rarefaction fan, contact discontinuity, and shock front. Mesh and Courant number sensitivity studies established that a moderate resolution offered a good balance between numerical accuracy and computational efficiency. At higher Mach numbers, the solver remained stable and captured the correct wave structure, with only minor pre-shock oscillations typical of pressure-based formulations. Comparison with the density-based `rhoCentralFoam` confirmed that, while density-based solvers retain slightly sharper shocks in the highly supersonic regime, `XiFoam` delivers physically consistent and bounded results even under strong compressibility effects. These findings establish that, with appropriate numerical schemes, the solver can handle weak to moderate strength shocks with high fidelity, a prerequisite for simulating turbulent hydrogen deflagrations.

The second stage of validation employed the ENACCEF-2 Step0 configuration, which subjects the solver to flame–shock interactions in a confined, obstacle-rich geometry. This case provided a more realistic and demanding benchmark, representative of accident-relevant containment conditions. The simulations demonstrated that the Turbulent Flame Closure (TFC) model, coupled with the pressure based framework, could accurately capture both the acceleration of turbulent flames and the interaction of flame fronts with the reflected shock.

Together, the Sod shock tube and ENACCEF-2 Step0 validations demonstrate that a pressure-based framework is numerically stable and physically accurate across a spectrum of conditions-from idealised, one-dimensional shock-dominated flows to complex, multi-dimensional confined combustion scenarios involving shock-flame interactions.

- **Implementation and validation of the Bentaïb laminar flame speed correlations**

The Bentaïb flame speed library was successfully implemented within `OpenFOAM`. Validation against ENACCEF experimental data for homogeneous mixtures confirmed that the implementation recovers the correct behaviour and yields improved agreement over constant S_L model. The library smoothly

transitions to from a non zero variance to the zero-variance limit, as demonstrated by small-variance sensitivity tests, confirming correct integration and numerical robustness in `OpenFOAM`.

- **Capturing combustion in inhomogeneous mixtures using mixture fraction and variance as inputs**

The solver was extended to account for subgrid-scale mixture composition fluctuations via the mixture fraction variance, $\widetilde{Z''^2}$, treated as a prescribed constant in the present work. Parametric sweeps demonstrated that incorporating a non-zero variance leads to marked improvements in flame acceleration and intermediate pressure rise prediction in the turbulent acceleration phase of RUN 765. Even modest variances (0.5-2% of $\tilde{Z}$) were found to have a strong effect on reactive tail activation in lean conditions.

- **Re-assessment of the role of mixture fraction variance under stratified conditions**

Contrary to earlier conclusions in the literature that Z''^2 plays a negligible role under stratified conditions, this study has shown that variance effects can be substantial in stratified hydrogen–air mixtures near the lean limit. The a priori beta-PDF analysis demonstrated a non-monotonic dependence of the effective laminar flame speed on $\widetilde{Z''^2}$, with an optimal variance range yielding maximum acceleration. Simulations on RUN 765 confirmed this trend in flame velocity and pressure peaks. While the current approach used a fixed variance, it is anticipated that solving the full variance transport equation would allow $\widetilde{Z''^2}$ to evolve with turbulence parameters k and ϵ, leading to increased variance during the turbulent acceleration phase and further improving agreement with experimental data.

This work has extended a pressure-based CFD solver to include physically grounded laminar flame speed correlations and variance effects, demonstrated its stability under accident-relevant conditions, and provided new insights into the coupled effects of mixture inhomogeneity and subgrid-scale composition fluctuations on hydrogen deflagration behaviour in confinement-like geometries. The findings directly inform model development for safety analysis tools aimed at predicting combustion loads in nuclear containment scenarios.

6.1. Recommendations

Based on the findings and limitations identified in this work, several recommendations are proposed to improve the predictive accuracy, computational efficiency, and general applicability of the developed solver framework:

1. **Thermodynamic model refinement for mixture fraction formulation:** In the current formulation, the thermodynamic and transport properties are evaluated only for two reference states: reactants and products. When $\tilde{Z}$ is introduced, the mixture can locally correspond to fuel, oxidiser, or products, each possessing distinct thermophysical properties. The absence of a library to adapt the thermodynamics to the mixture fraction formulation limits accuracy in partially premixed conditions. Implementing a composition-aware thermodynamic model that interpolates properties based on $\tilde{Z}$ would improve fidelity in regions with significant stratification.
2. **Completion of ENACCEF test matrix:** Extend the validation campaign to include the remaining ENACCEF runs, particularly RUN 736 and RUN 733 (see Table 5.6). RUN 736 introduces a stronger negative concentration gradient, while RUN 733 provides a positive concentration gradient, which is of special interest due to its potential to produce early flame acceleration in the lean region followed by enriched burning. These complementary datasets will enable a more thorough evaluation of model robustness under varying stratification patterns.
3. **Improved numerical integration for $\widetilde{Z''^2}$-dependent flame speed evaluation:** The current approach integrates the product of the beta-PDF and S_L using a fixed-point trapezoidal method. For small variance values, the beta-PDF becomes sharply peaked, requiring dense sampling to capture the distribution accurately-significantly increasing computational cost. Implementing an adaptive quadrature algorithm in C++ within the OpenFOAM framework would allow accurate and efficient evaluation of the integral, especially in extreme variance regimes.
4. **Solving the mixture fraction variance transport equation:** In this study, $\widetilde{Z''^2}$ was prescribed

as a constant. Solving the transport equation for Z''^2 would allow it to evolve dynamically with turbulence quantities k and ϵ. This is expected to increase variance in the turbulent acceleration phase, thereby enhancing reactive-tail activation and improving agreement with experimental flame velocity and pressure rise trends.

5. **Examine the effect of diluents:** Conduct additional simulations with diluents such as steam, CO, or nitrogen to examine their influence on flame speed, pressure, and turbulence-chemistry interaction. Such tests would improve the applicability of the solver to real containment accident scenarios, where gas mixtures often contain significant diluent fractions.
6. **Cross-facility validation:** Extend validation beyond the ENACCEF facility by testing against datasets from other experimental configurations with similar confinement and stratification features. This will allow assessment of model robustness and generality in geometries, boundary conditions, and turbulence regimes not covered by ENACCEF.
7. **High-fidelity turbulence combustion modelling:** Introduce Large-Eddy Simulation (LES) as an optional turbulence modelling approach within the framework. LES can provide improved resolution of large-scale turbulent structures and offer more detailed insight into the performance of the combustion model, especially in transient and stratified regimes.

Collectively, these recommendations target both the physical modelling and numerical implementation aspects of the framework. Implementing them would enhance accuracy in predicting flame dynamics under complex, accident-relevant conditions while ensuring computational tractability for containment-scale safety analyses.

References

[1] International Energy Agency. *World Energy Outlook 2022*. Tech. rep. Paris, France: International Energy Agency, 2022. URL: https://www.iea.org/reports/world-energy-outlook-2022.

[2] J. R. Lamarsh and A. J. Baratta. *Introduction to Nuclear Engineering*. 3rd Edition. Prentice Hall, 2001. ISBN: 978-0-201-82498-8.

[3] Office for Nuclear Regulation. *GDA Issue GI-AP1000-RC-03: Hydrogen Dosing System Assessment*. Tech. rep. ONR, 2016. URL: https://www.onr.org.uk/media/1ohmdt2b/onr-nr-ar-16-046.pdf.

[4] U.S. Nuclear Regulatory Commission. *Chemical and Volume Control System (CVCS) Description*. Tech. rep. U.S. NRC, 2011. URL: https://www.nrc.gov/docs/ML1123/ML11231A402.pdf.

[5] International Atomic Energy Agency. *Mitigation of Hydrogen Hazards in Severe Accidents in Nuclear Power Plants*. 1661. Vienna, Austria, 2011. ISBN: 978-92-0-116510-7. URL: https://www.iaea.org/publications/8646/mitigation-of-hydrogen-hazards-in-severe-accidents-in-nuclear-power-plants.

[6] World Nuclear Association. *The Three Mile Accident*. URL: https://world-nuclear.org/information-library/safety-and-security/safety-of-plants/three-mile-island-accident.

[7] M. Holt, R. J. Campbell, and M. B. Nikitin. *Fukushima Nuclear Disaster*. Tech. rep. R41694. Congressional Research Service, 2012. URL: https://crsreports.congress.gov/product/pdf/R/R41694.

[8] Tokyo Electric Power Company Holdings, Inc. *Things You Should Know More About Decommissioning: What caused the hydrogen explosions?* 2025. URL: https://www.tepco.co.jp/en/hd/decommission/towards_decommissioning/Things_you_should_know_more_about_decommissioning/answer-33-e.html.

[9] Z. Wang, E. Secnik, and G.F. Naterer. *Safety and Risk Management in Nuclear-Based Hydrogen Production with Thermal Water Splitting*. Tech. rep. University of Ontario Institute of Technology, 2019.

[10] National Academies of Sciences, Engineering, and Medicine. *Lessons Learned from the Fukushima Nuclear Accident for Improving Safety of U.S. Nuclear Plants*. Washington, DC: National Academies Press, 2014. DOI: 10.17226/18294.

[11] International Atomic Energy Agency. *Mitigation of Hydrogen Hazards in Water-Cooled Power Reactors*. Tech. rep. IAEA, 2001.

[12] OECD Nuclear Energy Agency CSNI. “Status Report on Hydrogen Management and Related Computer Codes”. In: 2015.

[13] C.R. Norman. *WASH 1400: Reactor Safety Study*. U.S. Nuclear Regulatory Commission, 1975.

[14] M. Ross. *NUREG 1150: Severe Accident Risks: An Assessment for Five U.S. Nuclear Power Plants*. U.S. Nuclear Regulatory Commission, 1990.

[15] T. Wellock. “Safe Enough? A History of Nuclear Power and Accident Risk”. In: *The New Yorker* (Aug. 2022). URL: https://www.newyorker.com/science/elements/how-safe-are-nuclear-power-plants.

[16] M. Hirano, T. Yonomoto, and M. Ishigaki. “Insights from Review and Analysis of the Fukushima Dai-ichi Accident”. In: *Journal of Nuclear Science and Technology* 49.1 (2012). DOI: 10.1080/00223131.2011.630389.

[17] International Atomic Energy Agency. *Mitigation of Hydrogen Hazards in Severe Accidents in Nuclear Power Plants*. Tech. rep. IAEA-TECDOC-1661. Vienna: International Atomic Energy Agency, 2011.

[18] L. L. Humphries and R. K. Cole. *MELCOR Computer Code Manuals Vol. 2: Reference Manual*. 2015.

[19] K. K. Murata and D. E. Carroll. *User's Manual for CONTAIN 1.1: A Computer Code for Severe Nuclear Reactor Accident Containment Analysis*. Tech. rep. U.S. Nuclear Regulatory Commission, 1989.

[20] W.K. Hessling and B. Schwinges. *ASTEC v0 CPA Module, Program Reference Manual, Rev. 0*. ASTECV00DOC001-34. ASTEC. 1998.

[21] M. S. Marek. *Steady-State and Accident Analyses of PBMR with the Computer Code SPECTRA*. Tech. rep. INIS-XA-524. International Atomic Energy Agency (IAEA), 2002.

[22] H. Jasak, A. Jemcov, and Z. Tukovic. "OpenFOAM: A C++ Library for Complex Physics Simulations". In: *International Workshop on Coupled Methods in Numerical Dynamics*. Vol. 1000. 2007, pp. 1–20.

[23] Ansys Inc. *Fluent Version 12.0 User Guide*. Ansys Inc. 2009.

[24] Siemens CD-Adapco. *STAR CCM+ User Guide Version 12.04*. CD-Adapco. 2017.

[25] E. M. J. Komen, D. C. Visser, F. Roelofs, and J. G. T. Te Lintelo. "The role of CFD computer analyses in hydrogen safety management". In: *Atw. Internationale Zeitschrift für Kernenergie* 60.11 (2015), pp. 660–665.

[26] O. Reynolds. "On the Dynamical Theory of Incompressible Viscous Fluids and the Determination of the Criterion". In: *Philosophical Transactions of the Royal Society of London A* 186 (1895), pp. 123–164. DOI: 10.1098/rsta.1895.0004.

[27] J. W. Deardorff. "A numerical study of three-dimensional turbulent channel flow at large Reynolds numbers". In: *Journal of Fluid Mechanics* 41.2 (1970), pp. 453–480. DOI: 10.1017/S002211207 0000691.

[28] P. R. Spalart. "Comments on the feasibility of LES for wings and on a hybrid RANS/LES approach". In: *1st ASOSR Conference on DNS/LES*. 1997.

[29] G. N. Coleman and R. D. Sandberg. *A Primer on Direct Numerical Simulation of Turbulence – Methods, Procedures and Guidelines*. Tech. rep. University of Southampton, 2010. URL: https://eprints.soton.ac.uk/66182/1/A_primer_on_DNS.pdf.

[30] P.J. Lobato. "Numerical Simulation of Turbulent Hydrogen Combustion for Nuclear Safety Management". Master's Thesis. Delft University of Technology, 2022.

[31] J.D. Palma. "Development and Implementation of a CFD Code for Hydrogen Combustion". Master's Thesis. University of Pisa, Department of Civil and Industrial Engineering, 2022.

[32] J. Goulier, A. Comandini, F. Halter, and N. Chaumeix. "Experimental study on turbulent expanding flames of lean hydrogen/air mixtures". In: *Proceedings of the Combustion Institute* 36.2 (2017), pp. 2823–2832. DOI: 10.1016/j.proci.2016.06.074.

[33] N. Chaumeix. *ENACCEF - Experimental Facility for Combustion Studies*. https://icare.cnrs.fr/en/en-research/en-facilities/en-ct-enaccef/. Accessed: 2025-07-31. 2024.

[34] A. Bentaib and N. Chaumeix. *SARNET H2 Combustion Benchmark: Diluent Effect on Flame Propagation – Blind Phase Results*. Technical Report. IRSN, 2012.

[35] P. Sathiah, E. M. J. Komen, and D. Roekaerts. "The Role of CFD Combustion Modeling in Hydrogen Safety Management – III: Validation Based on Homogeneous Hydrogen–Air–Diluent Experiments". In: *Nuclear Engineering and Design* 289 (2015), pp. 296–310. DOI: 10.1016/j.nucengdes.2014.05.042.

[36] T Poinsot and D Veynante. *Theoretical and Numerical Combustion*. RT Edwards, Inc., 2005. ISBN: 9781930217102.

[37] F. T. M. Nieuwstadt, J. Westerweel, and B. J. Boersma. *Turbulence: Introduction to Theory and Applications of Turbulent Flows*. Springer, 2016. ISBN: 978-9402406389.

[38] P. K. Kundu, I. M. Cohen, and D. R. Dowling. *Fluid Mechanics*. 6th. Academic Press, 2016. ISBN: 978-0124059351.

[39] A. Kolmogorov. “The local structure of turbulence in incompressible viscous fluid for very large Reynolds numbers”. In: *Cr Acad. Sci. URSS* 30 (1941), pp. 301–305.

[40] A. Kolmogorov. “Dissipation of energy in the locally isotropic turbulence”. In: *Dokl. Akad. Nauk SSSR A*. Vol. 32. 1941, pp. 16–18.

[41] Altair Engineering, Inc. *Turbulence Scales and Energy Cascade*. 2021. URL: %5Curl%7Bhttps://2021.help.altair.com/2021/hwsolvers/acusolve/topics/acusolve/training_manual/turb_scales_energy_cascasde_r.htm%7D.

[42] J. H. S. Lee and M. Berman. “Hydrogen Combustion and Its Application to Nuclear Reactor Safety”. In: *Heat Transfer in Nuclear Reactor Safety*. Vol. 29. Advances in Heat Transfer. Elsevier, 1997, pp. 59–127.

[43] P. Palies. “2 - Premixed Combustion for Combustors”. In: *Stabilization and Dynamic of Premixed Swirling Flames*. Ed. by P. Palies. Academic Press, 2020, pp. 57–103.

[44] A. H. Shapiro. *The Dynamics and Thermodynamics of Compressible Fluid Flow, Vol. I*. New York: The Ronald Press Company, 1953.

[45] F. A. Williams. *Combustion Theory*. 2nd. CRC Press, 2018. ISBN: 9780367025369.

[46] J. Hasslberger, L. R. Boeck, and T. Sattelmayer. “Numerical Simulation of Deflagration-to-Detonation Transition in Large Confined Volumes”. In: *Journal of Loss Prevention in the Process Industries* 36 (2015), pp. 371–379. DOI: 10.1016/j.jlp.2014.10.003.

[47] Y.B. Zel’dovich, G.I. Barenblatt, D.H. McNeill, V.B. Librovich, and G.M. Makhviladze. *The Mathematical Theory of Combustion and Explosions*. Consultants Bureau, 1985. ISBN: 9780306109744.

[48] A. C. Benim and K. J. Syed. *Flashback Mechanisms in Lean Premixed Gas Turbine Combustion*. Springer, 2011. ISBN: 978-3-642-17860-1.

[49] A. Lipatnikov. *Fundamentals of Premixed Turbulent Combustion*. CRC Press, 2012. ISBN: 9781439862294.

[50] N. Peters. “The Turbulent Burning Velocity for Large-scale and Small-scale Turbulence”. In: *Journal of Fluid Mechanics* 384 (1999), pp. 107–132. DOI: 10.1017/S002211209800421X.

[51] A.Y. Poludnenko. “Flamelet structure and its effect on turbulent burning velocities”. In: *Combustion and Flame* (2024). Review on flamelet structure and flame brush.

[52] NEA. *Flame Acceleration and Deflagration to Detonation Transition in Containment*. Tech. rep. Nuclear Energy Agency (NEA), 2020.

[53] A. N. Lipatnikov and J. Chomiak. “Turbulent flame speed and thickness: phenomenology, evaluation, and application in multidimensional simulations”. In: *Progress in Energy and Combustion Science* 28.1 (2002), pp. 1–74.

[54] T. Poinsot and D. Veynante. *Theoretical and Numerical Combustion*. 1st. Philadelphia, PA: Edwards, 2001.

[55] Y. R. Sivathanu and G. M. Faeth. “Generalized State Relationships for Scalar Properties in Non-Premixed Hydrocarbon/Air Flames”. In: *Combustion and Flame* 82 (1990), pp. 211–230.

[56] S. B. Pope. *Turbulent Flows*. Cambridge University Press, 2000. ISBN: 9780521591256. DOI: 10.1017/cbo9780511840531.

[57] A. Favre. “Statistical equations of turbulent gases”. In: *Problems of Hydrodynamics and Continuum Mechanics*. SIAM, 1969, pp. 231–266.

[58] B. E. Launder and D. B. Spalding. “The Numerical Computation of Turbulent Flows”. In: *Numerical Prediction of Flow, Heat Transfer, Turbulence and Combustion*. Elsevier, 1983, pp. 96–116.

[59] D. C. Wilcox. “Reassessment of the Scale-Determining Equation for Advanced Turbulence Models”. In: *AIAA Journal* 26.11 (1988), pp. 1299–1310.

[60] F. Moukalled, L. Mangani, and M. Darwish. “The finite volume method”. In: *The Finite Volume Method in Computational Fluid Dynamics*. Springer, 2016, pp. 103–135.

[61] B. F. Magnussen and B. H. Hjertager. “On mathematical modeling of turbulent combustion with special emphasis on soot formation and combustion”. In: *Symposium (International) on Combustion*. Vol. 16. 1. Elsevier, 1977, pp. 719–729. DOI: 10.1016/S0082-0784(77)80366-4.

[62] K. N. C. Bray, P. A. Libby, and J. B. Moss. “Unified modeling approach for premixed turbulent combustion—Part I: General formulation”. In: *Combustion and Flame* 61.1 (1985), pp. 87–102. DOI: 10.1016/0010-2180(85)90075-6.

[63] V. L. Zimont. “Theory of turbulent combustion of a homogeneous fuel mixture at high Reynolds numbers”. In: *Combustion, Explosion, and Shock Waves* 15.3 (1979), pp. 305–311. DOI: 10.1007/BF00785062.

[64] J. H. Ferziger, M. Peric, and R. L. Street. *Computational Methods for Fluid Dynamics*. Fourth. Springer, 2019. ISBN: 978-3-642-97866-5.

[65] K. C. Karki and S. V. Patankar. “Pressure Based Calculation Procedure for Viscous Flows at All Speeds in Arbitrary Configurations”. In: *AIAA Journal* 27.9 (1989), pp. 1167–1174. DOI: 10.2514/3.10242.

[66] I. Demirdzic, Z. Lilek, and M. Peric. “A collocated finite volume method for predicting flows at all speeds”. In: *International Journal for Numerical Methods in Fluids* 16.12 (1993), pp. 1029–1050. DOI: 10.1002/fld.1650161202.

[67] H. G. Weller, G. Tabor, A. D. Gosman, and C. Fureby. “Application of a flame-wrinkling LES combustion model to a turbulent mixing layer”. In: *Twenty-Seventh Symposium (International) on Combustion/The Combustion Institute*. 1998, pp. 899–907.

[68] G. A. Sod. “A survey of several finite difference methods for systems of nonlinear hyperbolic conservation laws”. In: *Journal of Computational Physics* 27.1 (1978), pp. 1–31. DOI: 10.1016/0021-9991(78)90023-2.

[69] A. Kurganov and E. Tadmor. “New High-Resolution Central Schemes for Nonlinear Conservation Laws and Convection Diffusion Equations”. In: *Journal of Computational Physics* 160.1 (2000), pp. 241–282. DOI: 10.1006/jcph.2000.6459. URL: https://doi.org/10.1006/jcph.2000.6459.

[70] D. G. Goodwin, H. K. Moffat, I. Schoegl, R. L. Speth, and B. W. Weber. *Cantera: An Object-Oriented Software Toolkit for Chemical Kinetics, Thermodynamics, and Transport Processes*. Version 3.1.0. Cantera Project. 2024. DOI: 10.5281/zenodo.14455267. URL: https://www.cantera.org.

[71] O. L. Gülder. *Correlations of laminar combustion data for alternative SI engine fuels*. Technical Report SAE Paper 840324. SAE Technical Paper, 1984. DOI: 10.4271/840324.

[72] S. Ravi and E. L. Petersen. “Laminar flame speed correlations for pure-hydrogen and high-hydrogen content syngas blends with various diluents”. In: *International Journal of Hydrogen Energy* 37.24 (2012), pp. 19177–19189. DOI: 10.1016/j.ijhydene.2012.09.031.

[73] D. Liu and R. MacFarlane. “Laminar burning velocities of hydrogen–air and hydrogen–air–steam flames”. In: *Combustion and Flame* 49.1–3 (1983), pp. 59–71. DOI: 10.1016/0010-2180(83)90111-7.

[74] I. L. Drell and F. E. Belles. *Survey of Hydrogen Combustion Properties*. Tech. rep. Report 1383. National Advisory Committee for Aeronautics (NACA), 1958.

[75] J. Manton and B. B. Milliken. “Study of Pressure Dependence of Burning Velocity by the Spherical Vessel Method”. In: *Proceedings of the Gas Dynamics Symposium on Aerothermochemistry*. Northwestern University, 1956, pp. 151–157.

[76] *Biennial Report on Hydrogen Safety: Dependence of Burning Velocity on Hydrogen Concentration, Pressure, and Temperature*. Tech. rep. HySafe Consortium, 2007.

[77] G. R. Pugh. “An Analysis of the Lanczos Gamma Approximation”. PhD thesis. Vancouver, Canada: University of British Columbia, 2004.

[78] H.G. Weller. *The development of a new flame area combustion model using conditional averaging*. TF 9307. Imperial College of Science, Technology and Medicine, 1993.

[79] O. L. Gülder. “Turbulent premixed flame propagation models for different combustion regimes”. In: *Symposium (International) on Combustion*. Vol. 23. Elsevier, 1991, pp. 743–750. DOI: 10.1016/S0082-0784(06)80287-3.

[80] OECD Publishing. *ISP-49 on Hydrogen Combustion*. Tech. rep. OECD, 2012.

A

Appendix - A

A.1. Dimensionless Numbers

Dimensionless numbers provide critical insight into the nature of reacting flows, offering a framework to classify flow regimes and combustion phenomena. They are instrumental in guiding modeling assumptions and assessing the relative importance of physical processes such as diffusion, advection, chemical kinetics, and turbulence. This section introduces the principal dimensionless numbers relevant to turbulent premixed and partially premixed combustion.

Reynolds Number (Re)

The Reynolds number characterizes the ratio of inertial forces to viscous forces in a flow:

$$Re = \frac{\rho U L}{\mu} = \frac{U L}{\nu} \tag{A.1}$$

where ρ is the fluid density [kg/m^3], U is the characteristic velocity [m/s], L is the characteristic length [m], μ is the dynamic viscosity [Pa $\cdot$ s], and $\nu = \mu/\rho$ is the kinematic viscosity [m^2/s]. Higher Re values typically indicate transition to turbulent flow.

In combustion modeling, the turbulent Reynolds number is more relevant:

$$Re_t = \frac{u' \ell_t}{\nu} = \left(\frac{\ell_t}{\delta_L}\right)\left(\frac{u'}{S_{L,0}}\right) \tag{A.2}$$

where u' is the root-mean-square of turbulent velocity fluctuations, ℓ_t is the turbulent integral length scale, δ_L is the laminar flame thickness, and $S_{L,0}$ is the unstrained laminar flame speed.

Mach Number (Ma)

The Mach number measures the ratio of the local flow velocity to the local speed of sound:

$$Ma = \frac{u}{a_s}, \qquad a_s = \sqrt{\gamma R T} \tag{A.3}$$

Here, a_s is the local speed of sound [m/s] for an ideal gas, $\gamma = c_p/c_v$ is the specific heat ratio, R is the specific gas constant, and T is the temperature [K]. Subsonic ($Ma < 1$), transonic ($Ma \approx 1$), and supersonic ($Ma > 1$) flows have different flow characteristics and boundary condition requirements.

Prandtl Number (Pr)

The Prandtl number quantifies the ratio of momentum diffusivity to thermal diffusivity:

$$Pr = \frac{\nu}{\alpha} = \frac{\mu c_p}{\kappa} \tag{A.4}$$

where $\alpha = \kappa/(\rho c_p)$ is the thermal diffusivity [m^2/s], and κ is the thermal conductivity [W/m $\cdot$ K]. For turbulent flows, a turbulent Prandtl number is used:

$$Pr_t = \frac{\nu_t}{\alpha_t} \tag{A.5}$$

Schmidt Number (Sc)

The Schmidt number is the ratio of momentum diffusivity to mass diffusivity:

$$Sc = \frac{\nu}{D} \tag{A.6}$$

where D is the species mass diffusivity [m^2/s]. For turbulent flows, the turbulent Schmidt number is:

$$Sc_t = \frac{\nu_t}{D_t} \tag{A.7}$$

Lewis Number (Le)

The Lewis number describes the ratio of thermal diffusivity to mass diffusivity:

$$Le = \frac{\alpha}{D} = \frac{Sc}{Pr} \tag{A.8}$$

In many combustion models, a unity Lewis number is assumed, though this may not hold for all species or operating conditions. For turbulence, an analogous turbulent Lewis number can be defined as:

$$Le_t = \frac{\alpha_t}{D_t} \tag{A.9}$$

Damköhler Number (Da)

The Damköhler number compares the turbulence time scale to the chemical reaction time scale:

$$Da = \frac{\tau_t}{\tau_c} = \frac{\ell_t/u'}{\delta_L/S_{L,0}} = \left(\frac{\ell_t}{\delta_L}\right)\left(\frac{u'}{S_{L,0}}\right)^{-1} \tag{A.10}$$

where τ_t is the turbulent timescale and τ_c is the chemical timescale. High Da implies fast chemistry relative to turbulence.

Karlovitz Number (Ka)

The Karlovitz number quantifies the ratio of the chemical time scale to the Kolmogorov time scale:

$$Ka = \left(\frac{\delta_L}{\eta}\right)^2 = \left(\frac{\delta_L/S_{L,0}}{\eta/u'(\eta)}\right) \tag{A.11}$$

It is often expressed in terms of Re_t and Da:

$$Ka = Re_t^{-1/2} \cdot Da^{-1} \qquad \Rightarrow \qquad Re_t = Da^2 Ka^2 \tag{A.12}$$

Markstein Number ($\mathcal{M}$)

The Markstein number reflects the effect of flame stretch on flame speed and is defined as:

$$\mathcal{M} = \frac{\mathcal{L}}{\delta_L} \tag{A.13}$$

where $\mathcal{L}$ is the Markstein length. Positive $\mathcal{M}$ implies flame stabilization under stretch, while negative $\mathcal{M}$ indicates destabilization.

Zel'dovich Number (β)

The Zel'dovich number quantifies the sensitivity of the reaction rate to temperature and is given by:

$$\beta = \frac{E_a}{RT_b} \cdot \frac{T_b - T_u}{T_b} \tag{A.14}$$

where E_a is the activation energy [J/mol], R is the universal gas constant, and T_b, T_u are the burnt and unburnt gas temperatures [K]. It reflects the steepness of the temperature dependence in the Arrhenius rate expression.

A.2. Pressure based algorithms for predicting flows at all speeds

In chapter 4, the PIMPLE algorithm was introduced for both subsonic and supersonic flows. This section talks about the modification needed to account for compressibility effects in supersonic cases. Demirdžić et al [66] explicitly added mass flux corrections, including density variations to account for compressible effects, making their method applicable to compressible flows at all speeds.

A.2.1. Methodology

In the case of incompressible flows, the mass flux correction is obtained by correcting the velocity. However, in the case of compressible flows, relative density changes become significant, and they have to be taken into account when deriving the mass correction expression in terms of velocity and density. To consider that, let us go back to the predictor - corrector steps of PISO algorithm.
After discretization, the momentum equation reduces to the following algebraic matrix equation:

$$[A]\,(U) = [Q] \tag{A.15}$$

where A is the square coefficient matrix, U is the velocity matrix and Q is the source term matrix.To simplify this, the left hand side is split into a diagonal and a non diagonal matrix, where the non diagonal matrix contains the convection and diffusion flux contributions.

$$A_o u_o + \sum_{\mathsf{nb}} A_{\mathsf{nb}} u_{\mathsf{nb}} = [Q] \tag{A.16}$$

Henceforth, a finite volume discretization method is considered, as explained in Demirdžić [66]. The discretization and the labelling has been explained in their paper and is taken directly. Now, equation A.16 for the cartesian velocity components is rewritten as:

$$u^{**}_{i,o} = \frac{\sum A_{\mathsf{nb}} u^*_{i,\mathsf{nb}} + Q^*_{u_i}}{A_o} - \left(\frac{S^i_{1P}}{A_o}\right)(p^*_e - p^*_w) - \left(\frac{S^i_{2P}}{A_o}\right)(p^*_n - p^*_s) \tag{A.17}$$

This is the finite volume equivalent of the first momentum corrector step. The mass fluxes based on the velocities calculated from equation A.17 with existing density and pressure fields do not necessarily satisfy the continuity equation, i.e. there exists a mass imbalance $\dot{Q}_m$.

$$\dot{m}^*_e - \dot{m}^*_w + \dot{m}^*_n - \dot{m}^*_s = Q^*_m. \tag{A.18}$$

For simplicity, consider $\dot{m}^*_e$. Let us correct the mass flux after the first momentum corrector step:

Mass Flux:

$$\dot{m}^{**}_e = [(\rho^* + \rho')(u^{**}_i + u'_i)S^x_1]_e \tag{A.19}$$

Flux Correction:

$$\dot{m}'_e = (\rho^* u'_i + \rho' u^{**}_i + \rho' u'_i)_e S^x_{1e} \tag{A.20}$$

The third term is neglected since it vanishes faster than the other two terms. To compute the flux correction $\dot{m}'_e$, we now need to find u^{**}_i and u'_i at the east face of the cell, which will be denoted as u^*_e and u'_e.

$$u^{**}_e = \left(\frac{\sum A_{\mathsf{nb}} u^{**}_{\mathsf{nb}} + Q^*_u}{A_o}\right)_e - \left(\frac{S^x_1}{A_o}\right)_e (p^*_E - p^*_P) \tag{A.21}$$

The velocity correction can be expressed in terms of the pressure corrections by using a truncated form of equation A.21:

$$u'_e = -\left(\frac{S_1^x}{A_O}\right)_e (p'_E - p'_P). \tag{A.22}$$

ρ^*, u_e^* and u'_e have been determined. Density correction can be implicitly expressed through the pressure correction in the following manner :

$$\rho' = \left(\frac{\partial \rho}{\partial p}\right) p'. \tag{A.23}$$

For an isentropic flow:

$$\left(\frac{\partial \rho}{\partial p}\right) = \frac{1}{c^2} = \frac{1}{\gamma RT} = C_\rho, \tag{A.24}$$

where c is the speed of sound. Substituting all these terms into the mass flux correction, we get:

$$\dot{m}'_e = -\rho_e^* S_{1e}^x \left(\frac{S_1^x}{A_P}\right)_e (p_E^* - p_P^*) + u_e^* S_{1e}^x (C_\rho p')_e. \tag{A.25}$$

There are two terms in this expression, the first term involving pressure correction difference across the cell, which is a diffusion like term, and a term depending on the face pressure p', which is like a convection like term. For incompressible flows, the second term vanishes, because the mass flux correction is just because of the velocity. In compressible flows, both these terms exist, and their relative importance on the mass flux correction depends on the kind of flow. Let us normalize the RHS of the mass flux correction equation to yield a weighting factor of 1 for p', the diffusion term gets a weighing factor proportional to $\frac{1}{M^2}$. for a subsonic flow this factor is several orders of magnitude larger than 1, so the first term dominates and the second is negligible. For compressible flows with high Mach numbers, the contrary is true: the weighting factor of the first term will be an order of magnitude or more below 1, so the second (convection-like) term will dominate. This numerical approach ensures that one formulation can be applied for all speeds.

This mass flux correction ensures that mass conservation is satisfied after the first momentum corrector step, and the next steps for PISO algorithm continues. This kind of a transonic mass flux correction has been implemented in pressure based solvers in OpenFOAM as well. The next section will talk about this flux correction implementation in rhoPimpleFoam.

Implementation in OpenFOAM rhoPimpleFoam is a pressure based solver dedicated to solve compressible flow problems. It is based on the PIMPLE algorithm, which is a combination of the PISO + SIMPLE algorithm. It has the same workflow as the PISO algorithm, the difference lies in the loops and the iterations. This report wont talk about the algorithm, it will just focus on how the mass flux corrections have been adopted in rhoPimpleFoam for transonic cases.

In transonic flows, the transition between subsonic to supersonic requires careful flux corrections to ensure numerical stability. OpenFOAM's `rhoPimpleFoam` solver implements a transonic flux correction term to smoothly transition between these regimes. This is achieved by introducing an additional correction term, ϕ_d, which modifies the mass flux ϕ_{HbyA}.

The base uncorrected mass flux in OpenFOAM is ϕ_{HbyA}, a modified version of equation A.25 . This is implemented in `rhoPimpleFoam` as:

Listing A.1: Implementation of mass flux in rhoPimpleFoam

```
// Calculate flux HbyA and add contribution from gravity term
surfaceScalarField phiHbyA
(
    "phiHbyA",
    fvc::interpolate(rho)*fvc::flux(HbyA)
```

```
  + rhorAUf*fvc::ddtCorr(rho, U, phi)
  + rhorAUf*fvc::interpolate(rho)*(g & mesh.Sf())
);
```

The pressure correction equation is then set up in the following way. The continuity equation is considered:

$$\frac{\partial \rho}{\partial t} + \nabla \cdot (\rho U) = 0$$

The Density and velocity are then broken down into the predicted and the correction terms:

$$\frac{\partial \rho^*}{\partial t} + \nabla \cdot (\rho^* u^*) + \frac{\partial \rho^{'}}{\partial t} + \nabla \cdot (\rho^* u^{'}) + \nabla \cdot (\rho^{'} u^*) = 0$$

Each of these terms are broken down in OpenFOAM notation:

$$\frac{\partial \rho^*}{\partial t} = fvc :: ddt(rho)$$

$$\nabla \cdot (\rho^* u^*) + \nabla \cdot (\rho^* u^{'}) = fvc :: div(phiHbyA) - fvm :: laplacian(rhorAUf, p) \tag{A.26}$$

Equation A.26 is obtained by a certain manipulation of terms and by rewriting pressure as the sum of the predictor and correction terms. The derivative of the density correction term is written as:

$$\frac{\partial \rho^{'}}{\partial t} = \psi \frac{\partial p^{'}}{\partial t} = psi * correction(fvm :: ddt(p))$$

The only remaining term is :

$$\nabla \cdot (\rho^{'} u^*) = \nabla \cdot (\psi P^{'} u^*)$$

which is the term ϕ_d when the transonic switch is enabled in rhoPimpleFoam. This term vanishes for subsonic flows because density changes are very small.

$$\phi_d = \frac{\psi}{\rho} \phi_{HbyA}, \tag{A.27}$$

This correction accounts for density-pressure interactions in transonic flows. Adding, we get all these terms implemented in rhoPimpleFoam in the following manner: pDDtEqn - fvm::laplacian(rhorAUf, p)

Listing A.2: Implementation of Transonic Correction and solving the pressure correction equation in rhoPimpleFoam

```
if (pimple.transonic())
{
    surfaceScalarField phid
    (
        "phid",
        (fvc::interpolate(psi)/fvc::interpolate(rho))*phiHbyA
    );

    phiHbyA -= fvc::interpolate(psi*p)*phiHbyA/fvc::interpolate(rho);

    fvScalarMatrix pDDtEqn
    (
        fvc::ddt(rho) + psi*correction(fvm::ddt(p))
      + fvc::div(phiHbyA) + fvm::div(phid, p)
     ==
        fvOptions(psi, p, rho.name())
    );

    while (pimple.correctNonOrthogonal())
    {
        fvScalarMatrix pEqn(pDDtEqn - fvm::laplacian(rhorAUf, p));

        // Relax the pressure equation to ensure diagonal-dominance
        pEqn.relax();

```

```
26          pEqn.solve(mesh.solver(p.select(pimple.finalInnerIter())));
27
28          if (pimple.finalNonOrthogonalIter())
29          {
30              phi = phiHbyA + pEqn.flux();
31          }
32      }
33  }
```

Modification of the Mass Flux

The transonic correction term ϕ_d is used to adjust the base flux ϕ_{HbyA} as:

$$\phi_{HbyA} = \phi_{HbyA} - \frac{\psi p}{\rho}\phi_{HbyA}. \tag{A.28}$$

Rearranging:

$$\phi_{HbyA} = \frac{\phi_{HbyA}^{\text{original}}}{1 + \frac{\psi p}{\rho}}. \tag{A.29}$$

This formulation ensures that:

- For low Mach numbers (**subsonic flow**): ψ is small, meaning the correction is negligible, and the elliptic pressure diffusion dominates.
- For high Mach numbers (**supersonic flow**): ψ is large, meaning the correction strongly modifies ϕ_{HbyA}, ensuring hyperbolic convection-dominated behavior.
- For transonic flows: Both terms contribute, ensuring a smooth transition between subsonic and supersonic regions.

By incorporating ϕ_d into the solver, `rhoPimpleFoam` achieves a robust formulation suitable for flows at all speeds, including challenging transonic regimes.

B

Appendix - B

B.1. OpenFOAM Description

As described in the introduction, there are different codes to perform CFD simulations: including not only the equations, but also numerical schemes, and linear system solution algorithms. The one that has been used for this thesis is `OpenFOAM` [22], which is a multipurpose toolbox written in C++ for the resolution of partial differential equations, especially those related to Computational Fluid Dynamics. Although it already includes many solvers, the open-source code is its true potential: every part of the code can be accessed, manipulated, and eventually reformulated to suit the specific requirements of a project. The source code is fully documented and the clear syntax presents a readable implementation of new models and equations. The C++ source code can be compiled afterward, obtaining an automatically parallelizable solver without the need for programming at low levels. Another big strength is that it is free and there are no license costs.

However, `OpenFOAM` is a fragmented project with many parallel versions and forked projects (the version used for this thesis is OpenFOAM v1812). It does not include a Graphical User Interface (GUI), and even if there is a large community, it can be challenging to implement new applications since not all details of the underlying code structure are documented for high-level development. Moreover, in recent versions the entanglement between different libraries and applications has increased. The widespread use of function virtualization and class inheritance increases the flexibility of the code, but also the complexity, making it more difficult to access and modify.

As there is no GUI, the simulations initially rely on several plain-text input files located in three basic directories, having the tree structure shown in Figure B.1. Additional files and folders may be required to perform certain pre- and post-processing tasks. New folders may include the `processorX` directories (for parallel execution of the solver), time directories (with the data saved at specified intervals), and the `postProcessing` folder (with data from OpenFOAM post-processing modules).

The `0/` folder contains the fields with the initial and boundary conditions used for the initialization of the application and the solution procedure. Some of the fields that commonly appear are `U` (velocity field) and `p` (pressure field). The `constant/` folder contains the mesh (under the subfolder `polyMesh/`), the properties of the flow (with dedicated files for combustion, thermophysical, and turbulence properties), and the inclusion of additional options in the solver with `fvOptions` (as source terms). Other files usually present in this folder are the `g` file (with the direction and magnitude of the gravitational force), the `dynamicMeshDict` file (for dynamic mesh library configuration), and the `boundaryRadiationProperties` or `radiationProperties` files (when radiation modeling is considered).

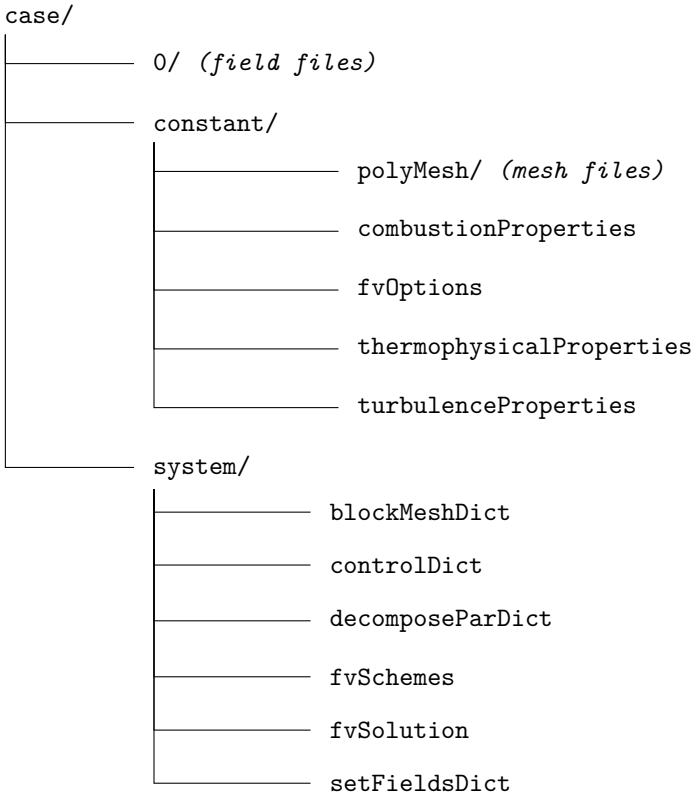

Figure B.1: Initial folder structure for a case in OpenFOAM

Finally, the `system/` folder contains the files that govern the simulation. The `blockMeshDict` file has the description of a hexahedral mesh defined by its vertices, faces, and blocks. The `controlDict` file dictates how the simulation is carried out (start and end time, timestep size, write intervals, etc.). The `decomposeParDict` file is used to decompose a given case into `processor` folders for parallel execution. The `setFieldsDict` file contains initialization definitions for non-uniform fields. The `fvSchemes` file specifies the numerical schemes used for discretization, and the `fvSolution` file defines the linear system solvers and pressure–velocity coupling. Other commonly used files in this folder include:

- `probes` – to extract data of specified fields at selected locations,
- `extrudeMeshDict` – to extrude meshes in a chosen direction,
- `snappyHexMeshDict` – to refine grids or generate complex meshes,
- `fileUpdate` – to update a given field during the simulation.

The description above applies to the setup of a case. However, the compilation of applications (solvers) and libraries follows another folder structure. The default applications and libraries of OpenFOAM are located in `$FOAM_APP` and `$FOAM_SRC`, respectively. Users can modify these libraries by copying them into their `/home` directory, editing the code and compiling them (using `wmake`). Libraries must then be linked to the application where required: either at compilation (by including them in the `Make/options` file of an application) or at runtime (by linking directly in the `controlDict` of a case). Both libraries and applications consist of header files (`.H`) and source code files (`.C`).

Apart from `OpenFOAM`, `Python` was also used extensively for post-processing, data handling, and figure generation. Finally, `Linux` scripting was used to automate solver execution, launch post-processing routines, and interact with the computing cluster used for the larger cases.

C

Appendix - C

This appendix includes the thermophysical properties for the ENACCEF-2, and the ENACCEF simulations performed.

C.1. Thermophysical Properties for ENACCEF-2

Table C.1: Thermodynamic, transport and combustion properties for the ENACCEF-2 Step 0 simulation

Reactants	
W (kg/kmol)	25.3603
T_{low} (K)	200.00
T_{common} (K)	1000.00
T_{high} (K)	6000.00
a_i $(T_{\text{low}} < T < T_{\text{common}})$	$\{\ 3.07921,\ 0.00118691,\ -3.83041 \times 10^{-7},\ 5.97173 \times 10^{-11},\ -3.48934 \times 10^{-15},\ -962.657,\ 4.51802\ \}$
a_i $(T_{\text{common}} < T < T_{\text{high}})$	$\{\ 3.42102,\ 0.000416651,\ -1.10714 \times 10^{-6},\ 2.55263 \times 10^{-9},\ -1.34386 \times 10^{-12},\ -1033.12,\ 2.79333\ \}$
μ ((N s)/m^2)	2.1377×10^{-5}
Pr	0.555945
Products	
W (kg/kmol)	27.1231
T_{low} (K)	200.00
T_{common} (K)	1000.00
T_{high} (K)	6000.00
a_i $(T_{\text{low}} < T < T_{\text{common}})$	$\{\ 3.00236,\ 0.00152595,\ -4.88233 \times 10^{-7},\ 7.35767 \times 10^{-11},\ -4.14656 \times 10^{-15},\ -5031.70,\ 5.70701\ \}$
a_i $(T_{\text{common}} < T < T_{\text{high}})$	$\{\ 3.65628,\ 0.000751540,\ 1.77760 \times 10^{-6},\ -1.92494 \times 10^{-10},\ -3.80328 \times 10^{-13},\ -5160.39,\ 2.51722\ \}$
μ ((N s)/m^2)	5.20313×10^{-5}
Pr	0.702876
Combustion	
$S_{L,0}$ (m/s)	0.27487
Le_{eff}	0.3348
L' (m)	-0.0002458
Φ	0.356692
T_{ad} (K)	1661.46

C.2. Thermophysical Properties for ENACCEF

Table C.2: Thermodynamic, transport and combustion properties for the ENACCEF Run 153

Reactants	
W (kg/kmol)	25.8383
T_{low} (K)	200.00
T_{common} (K)	1000.00
T_{high} (K)	3000.00
a_i $(T_{\text{low}} < T < T_{\text{common}})$	$\{\,3.27070,\ 0.00134291,\ -3.17177 \times 10^{-6},\ 4.43974 \times 10^{-9},\ -1.94260 \times 10^{-12},\ -1014.56,\ 4.37957\,\}$
a_i $(T_{\text{common}} < T < T_{\text{high}})$	$\{\,3.03650,\ 0.001296,\ -4.74827 \times 10^{-7},\ 8.76584 \times 10^{-11},\ -6.35209 \times 10^{-15},\ -961.694,\ 5.63252\,\}$
μ ((N s)/m^2)	1.84314×10^{-5}
Pr	0.563008
Products	
W (kg/kmol)	27.4292
T_{low} (K)	200.00
T_{common} (K)	1000.00
T_{high} (K)	3000.00
a_i $(T_{\text{low}} < T < T_{\text{common}})$	$\{\,3.46766,\ 0.000375926,\ -7.70424 \times 10^{-7},\ 2.14989 \times 10^{-9},\ -1.13498 \times 10^{-12},\ -4626.94,\ 4.12378\,\}$
a_i $(T_{\text{common}} < T < T_{\text{high}})$	$\{\,2.98403,\ 0.00155858,\ -5.39060 \times 10^{-7},\ 9.03050 \times 10^{-11},\ -5.80172 \times 10^{-15},\ -4538,\ 6.51765\,\}$
μ ((N s)/m^2)	4.81161×10^{-5}
Pr	0.704828
Combustion	
$S_{L,0}$ (m/s)	0.186455
Le_{eff}	0.357778
L' (m)	—
Φ	0.313238
T_{ad} (K)	1489.14